Universidade Federal do Ceará
Centro de Ciências
Programa de Pós–Graduação em Física
Doutorado em Física

Study of strongly correlated colloidal systems

Igor Rochaid Oliveira Ramos

Orientador: Prof. Dr. Wandemberg Paiva Ferreira

Fortaleza – CE
28 de agosto de 2014

Study of strongly correlated colloidal systems

Igor Rochaid Oliveira Ramos

Tese apresentada ao Departamento de Física da Universidade Federal do Ceará, como parte dos requisitos para a obtenção do Título de Doutor em Física.

Banca Examinadora:

Prof. Dr. Wandemberg Paiva Ferreira – UFC
(Orientador)

Prof. Dr. Gil de Aquino Farias – UFC

Prof. Dr. Raimundo Nogueira da Costa Filho – UFC

Prof. Dr. Felipe de Freitas Munarin – UFC

Prof. Dr. Fabricio Queiroz Potiguar – UFPA

Prof. Dr. Francois Maria Leopold Peeters – UA

À minha família e à minha esposa.

Acknowledgements

- Inicialmente, agradeço a Deus por ter me dado todas as condições para que eu pudesse realizar este trabalho.
- Ao meu orientador, Prof. Dr. Wandemberg Paiva Ferreira, por toda a atenção, respeito e por ter me ajudado nos momentos mais difíceis deste trabalho.
- À minha esposa, por estar ao meu lado durante todos esses anos.
- Aos meus pais, Rocha e Eliete, pela vida que me deram e por todo o amparo necessário para que eu pudesse chegar até aqui.
- Aos meus avós, Rita Ramos e Miguel Ramos (*in memoriam*), à minha tia, Maria Socorro Rocha Ramos, ao meu primo Cirilo, e à Ester por todo o amor, carinho, e os cuidados dedicados a mim até hoje.
- Aos meus tios, Raimundo (*in memoriam*), Rita, Gilson, Socorro e Conceição, por toda a ajuda durante todos os anos que passei em Fortaleza.
- Ao meu amigo Mardônio, pelos seus ensinamentos, direcionamentos e pelo incentivo, desde o pré-vestibular.
- Aos amigos, Philipe, Sílvia, Roberto Namor, Robson e Ítalo que muito me ajudaram durante todos esses anos. Serei eternamente grato.
- Ao Josa (da xerox) pela sua amizade, pelo seu trabalho, e por aceitar os fiados quando o dinheiro acaba.
- Ao chefe do Departamento.
- Aos examinadores da banca, pelas suas correções e sugestões, que muito enriqueceram este trabalho.
- Aos funcionários do Departamento de Física, em especial, a Rejane, Ana Cleide e Creuza.
- Ao VLIR-UOS (University Development Cooperation), pelo suporte financeiro durante o período que fiquei na Universidade da Antuérpia - Bélgica.

- Aos professores Dr. Francois Peeters e Dr. Milorad Milosevic por toda a ajuda durante os três meses que fiquei em Antuérpia.
- Ao CNPQ - Conselho Nacional de Desenvolvimento Científico e Tecnológico, pelo suporte financeiro.

Resumo

Nesta tese, estudamos as propriedades estruturais e dinâmicas, bem como, a fusão de sistemas coloidais.

Inicialmente, abordamos o problema de determinar as estruturas de mínima energia e o espectro de fônons de um sistema de dipolos magnéticos carregados, organizados em uma estrutura de bicamadas e orientados perpendicularmente ao plano das camadas. Este sistema pode ser sintonizado através de seis diferentes fases cristalinas, através da variação de parâmetros tais como a separação entre as camadas e/ou a carga e/ou o momento de dipolo das partículas. A presença de carga elétrica nas partículas dipolares é responsável pela nucleação de cinco fases onde as camadas não estão alinhadas verticalmente e uma fase desordenada, que não são encontradas no sistema em bicamadas de dipolos magnéticos previamente apresentado na literatura. Estas fases extras são uma consequência da competição entre a repulsão coulombiana e a interação atrativa entre os dipolos em diferentes camadas. As estruturas de mínima energia são sumarizadas em um diagrama de fases associado à separação entre camadas e a importância relativa entre as interações elétrica e magnética. Determinamos, ainda, a ordem das transições estruturais entre as várias configurações de mínima energia. O espectro de fônons do sistema foi calculado usando a aproximação harmônica. Um comportamento não-monotônico do espectro de fônons é encontrado como função da interação efetiva entre as partículas. A estabilidade termodinâmica das diferentes fases é determinada.

Em seguida, estudamos o sistema de bicamadas de dipolos magnéticos carregados para temperaturas diferentes de zero, investigando a fusão do sistema através do critério de Lindemann modificado, em função dos parâmetros: (i) a distância entre as camadas η e (ii) a intensidade relativa da interação magnética com respeito à interação elétrica λ. Para λ suficientemente grande, uma das fases (a fase hexagonal com alinhamento vertical) exibe um comportamento reentrante na temperatura de fusão em função de η. Uma vez que a carga e o momento de dipolo magnético das partículas coloidais pode ser alterado, por exemplo, pela variação do pH da solução na qual estão imersos e por um campo magnético externo, respectivamente, este sistema pode ser em princípio verificado experimentalmente.

Por último, um sistema bidimensional (2D) coloidal binário consistindo de dipolos interagentes é investigado. Dentro da aproximação harmônica, calculamos o espectro de fônons do sistema em função da composição, da razão entre os momentos de dipolo e da razão entre as massas das partículas pequenas e grandes. Através de uma análise sistemática dos espectros de fônons, determinamos a região de estabilidade das diferentes estruturas das ligas coloidais. As lacunas no espectro de frequência dos fônons, as frequências óticas no limite de longos comprimentos de onda e a velocidade do som são também discutidos. Usando o critério de Lindemann modificado e dentro da aproximação harmônica, estimamos a temperatura de fusão da sub -rede gerada pelas partículas grandes.

Abstract

This thesis presents the study of the structural and dynamical properties, as well as, melting of colloidal systems.

Initially, we study the structure and phonon spectrum of a system of charged magnetic dipoles, organized in a bilayer structure and oriented perpendicular to the plane of the layers. This system can be tuned through six different crystalline phases by changing parameters such as the interlayer separation and/or the charge and/or dipole moment of the particles. The presence of the electric charge on the dipole particles is responsible for the nucleation of five staggered phases and a disordered phase which are not found in the magnetic dipole bilayer system previously presented in the literature. These extra phases are a consequence of the competition between the repulsive Coulomb and the attractive dipole interlayer interaction. The minimum energy structures are summarized in a phase diagram associated to the separation between the layers and to the relative importance between the magnetic and electric interactions. We determine the order of the structural phase transitions. The phonon spectrum of the system was calculated within the harmonic approximation. A non-monotonic behavior of the phonon spectrum is found as a function of the effective strength of the inter-particle interaction. The thermodynamic stability of the different phases is determined.

Then, we study the bilayer system of charged magnetic dipoles for nonzero temperatures, investigating the melting behavior of the system through the modified Lindemann criterion, as a function of the parameters: (i) the distance between the layers η and (ii) the relative intensity of the magnetic interaction with respect to the electric interaction λ. For large enough λ, one of the phases (the matching hexagonal phase) exhibits a re-entrant melting behavior as a function of η. Since the charges and the magnetic dipole moment of the colloidal particles can be altered, for example, by changing the pH of the solution in which they are immersed or an external magnetic field, respectively, this system can be in principle verified experimentally.

Last, a two-dimensional (2D) binary colloidal system consisting of interacting dipoles is investigated. Within the harmonic approximation, we obtained the phonon spectrum of the system as a function of the composition, dipole moment ratio and mass ratio between the small and big particles. Through a systematic analysis of the phonon spectra, we are able to determine the stability region of the different lattice structures of colloidal alloys. The gaps in the phonon frequency spectrum, the optical frequencies in the long-wavelength limit and the sound velocity are discussed as well. Using the modified Lindemann criterion and within the harmonic approximation, we estimated the melting temperature of the sub-lattice generated by the big particles.

Contents

List of Figures

List of Tables

Chapter 1

Introduction

1.1 Colloidal systems

The term colloidal system or colloidal suspension is frequently used when one deals with materials that are composed of particles of typical sizes varying between 1 nm and 1 μm, called mesoscopic particles, dispersed into a solvent whose molecules are much smaller in size. The mesoscopic particles form the disperse phase and the solvent, the dispersion medium. In the case of a solid disperse phase composed of magnetic nanoparticles which are distributed into a liquid dispersion medium, this colloidal magnetic system is termed ferrofluid or magnetic fluid.

This type of system has attracted the attention of many reseachers in the last decades. The main reasons of the importance of the system of colloids are the following: 1) unlike atomic systems in which the interactions between the particles are determined by their electronic structure and therefore can not be controlled externally [1, 2], the interactions between colloidal particles and, thus, the physical properties of the system, can be modified externally by controlling, for example, the temperature, the salt concentration, the composition (stoichiometry) of the system and/or an external magnetic field, depending on the type of particle in the system; 2) from the experimental point of view, the size of the colloidal particles is of the order of magnitude of the wavelength of visible light (400 nm - 700 nm) and, thus, one can study this system through light scattering experiments [1, 2]. Besides, the particle motion can be observed directly using video microscopy and, therefore, the state of the system can be studied in real time [3, 4]. For example, in Figure 1.1, we have one-component monolayers of silica particles with diameter $3\mu m$ and $1\mu m$ at a horizontal octane/water interface, which were observed from above using video microscopy [5].

In a system of charged colloidal particles dispersed in a medium containing ions, the actual interaction between these colloidal particles is given by the Yukawa potential or Debye-Hückel potential [6, 7, 8]. In this case, for a given temperature, the interaction between the colloidal particles is screened by the surrounding ion cloud, and the screening length can be tailored by changing the ion concentration [6, 7]. For low ion concentration, the interaction can be approximated by a

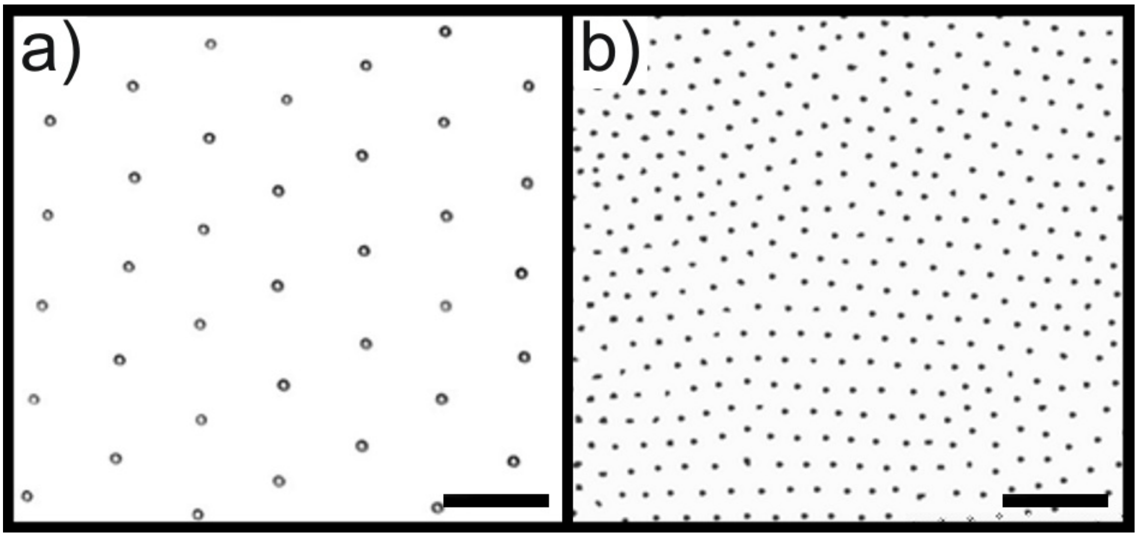

Figure 1.1: One component monolayers of silica particles with diameter (a) $3\mu m$ and (b) $1\mu m$ at a horizontal octance/water interface. The scale bars are equal to $30\mu m$ and the average distance between large particle centers in (a) is $28\mu m$. Figure taken from Ref. [5].

Coulomb potential.

On the other hand, in an electrically stabilized colloidal system, the charge of the colloids can be controlled by the pH of the solution by adding/removing salt to/from the solvent [9, 10]. For instance, in Fig. 1.2, we have the pH-dependence of the superficial density of charge of a ferrofluid based on cobalt ferrite nanoparticles. We can see that, for pH values around 3.5 and 10.5, the nanoparticles are charge saturated and the ferrofluid is thermodynamically stable [10].

In a system composed of super-paramagnetic colloidal particles, the interaction can be altered by changing the applied external magnetic field. Due to the super-paramagnetic character of the particles, thermal fluctuations of the magnetic moment around the preferred direction are negligible, i. e., the magnetic dipole of each particle aligns perfectly with the external field. Besides, the strength of the induced dipole moment can be tuned by the magnitude of the external magnetic field [11]. If the system has super-paramagnetic particles of different sizes, the composition (for example, the concentration of small particles) can be used to modify the interaction between the particles. Therefore, colloidal systems are very much used as model systems to study, for instance, melting, because the size of colloidal particles and their interactions can be tailored for experimental studies [2, 12, 13, 14].

The fact that the size of the colloidal particles and their interactions can be tailored for experimental studies is of great importance in the study and understanding of phase transitions, e. g., melting, since the observation of the melting transition of atomic or molecular materials on the microscopic scale is very difficult. Therefore, melting transition of most materials is not well understood because the lack of theories on a microscopic scale. The details of the interactions between the particles forming the crystal have great influence in the mechanism of melting and, as a consequence, the system of colloidal particles provides an appropriate scenario for testing the

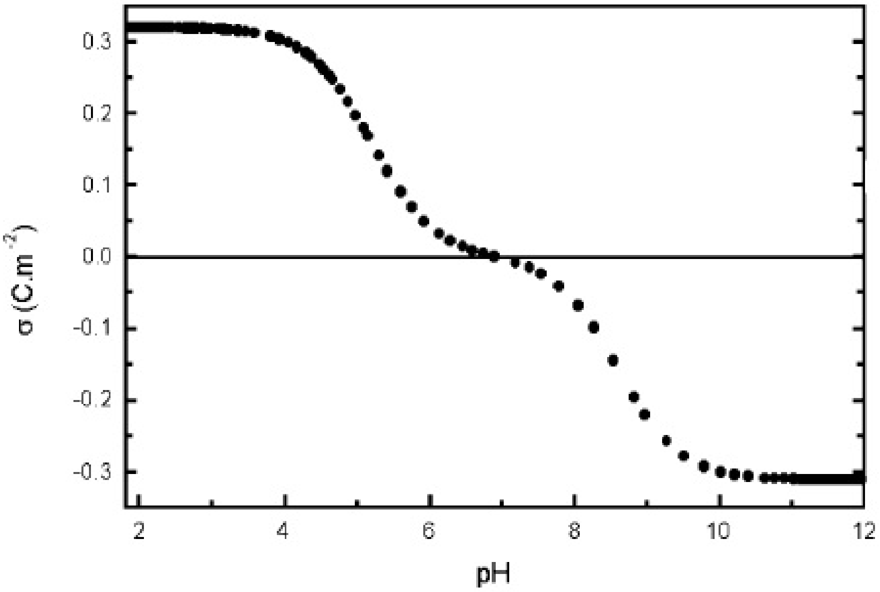

Figure 1.2: pH-dependence of the superficial density of charge. For pH ≤ 3.5 in acidic medium and pH ≥ 10.5 in basic one, the nanoparticles are charge saturated and the ferrofluid is thermodynamically stable. Figure taken from Ref. [10].

validity of a melting theory, for instance, the two-dimensional (2D) Kosterlitz-Thouless-Halperin-Nelson-Young (KTHNY) theory. According to this theory, melting is based on the decoupling of pairs of topological defects and it predicts the existence of an intermediate equilibrium phase - the *hexatic* phase - between the crystal and the liquid phase [14]. In the *hexatic* phase, the system has no translational order while the orientational correlation is still quasi-long-range. Such a two step melting is not known in 3D for isotropic pair interactions [4]. The theoretical melting scenario according to the KTHNY theory was confirmed experimentally using a one-component system of super-paramagnetic colloidal particles at an water-air interface, in the presence of an external magnetic field, and interacting through a repulsive dipole-dipole potential [14]. Although this system of interacting dipole particles is very well understood in the classical regime, it was unknown whether the *hexatic* phase exists when the quantum fluctuations play a major role. An estimate of the effect of quantum fluctuations on this *hexatic* phase was presented for both dipolar systems and charged Wigner crystals, predicting that the *hexatic* phase is stable to very low temperatures [15].

Furthermore, the dispersion relation in colloidal systems can also be accessed experimentally. For example, Keim *et al.* [2], resorted on a video-microscopy study of 2D colloidal crystals composed of super-paramagnetic colloidal particles, and show how to obtain direct access to the normal modes of vibration of the crystal. This is very important for studying, for instance, phononic crystals, i. e, materials with a band gap in their spectrum of transmitted sound waves (no vibrations are possible for frequencies within the gap). For example, the phonon spectra of periodic structures formed by 2D mixtures of dipolar colloidal particles was investigated, and it was shown that the phonon gaps can be controlled by changing the susceptibility ratio, the composition, and the mass ratio between the two components [16].

Besides melting and phonons, the structural phases in colloidal system is also frequently investigated. For instance, Law *et al.* [5], reported experimental studies on a 2D binary colloidal system composed of silica particles of different sizes floating at an oil-water interface, and interacting through a repulsive dipole-dipole potential. In this case, the interaction between the particles can be modified by changing the size of the colloidal particles.

The examples cited above help us to understand the main reasons of the importance of colloidal systems: the interaction between the particles can be externally controlled and the possibility of experimental access. This understanding is crucial for the appreciation of the next chapters since we will deal with the structural and dynamical properties of some colloidal systems.

1.2 Structure of the thesis

The present work is organized as follows: in chapter 2, we address the structural and dynamical properties of a system of charged magnetic dipoles in a bilayer structure. In chapter 3, we investigated the melting of the same system using the modified Lindemann criterion and within the harmonic approximation. In chapter 4, we study the dynamical properties and melting of binary system of magnetic dipolar particles in a monolayer structure. The conclusions are given in chapter 5.

Chapter 2

Bilayer crystals of charged magnetic dipoles: structure and phonon spectrum

2.1 Introduction

Strongly repulsive interacting particles crystallize for a certain range of density and temperature. This has been found in systems of rather different nature and therefore the study of the structural and dynamical properties of such a crystalline phase is of fundamental interest. The crystallization phenomenon of strongly interacting particles was originally predicted for an electron gas (Wigner crystal - WC) by E. P. Wigner in 1934 [17]. Up to now, the original three-dimensional (3D) WC of electrons is not yet observed experimentally, mainly due to defects and imperfections in real lattice structures. But experimental evidence of the WC was found in 1979 in a 2D system of electrons on the surface of liquid helium [18]. Nowadays, the term Wigner crystal is used in a broad sense for the crystalline state of clusters of strongly interacting particles. Such Wigner crystallization has also been observed in atomic and molecular clusters [19, 20, 21] and in several non-electronic classical systems as colloids [12, 5, 22, 23, 24, 16], complex dusty plasma [30], and metallic spheric balls [31].

For the particular case of classical systems (e. g., charged or magnetic colloidal particles [32]), crystallization is observed if the interaction potential energy overcomes the kinetic energy of the particles and correlation effects dominate the long-range structure of the system [33]. More specifically, the thermodynamic state of the system is characterized by the coupling parameter Γ, defined as the average of the ratio between the interaction potential energy and the kinetic energy. For a 2D classical system of charged particles with Coulomb interaction, $\Gamma = q^2\sqrt{\pi n}/k_B T$, where q is the charge of each particle, n the density, k_B the Boltzmann constant and T the temperature. For $\Gamma < 1$, the kinetic energy largely dominates the interacting term and the system behaves as a classical gas. For intermediate values $1 \leq \Gamma \leq 100$, particles become more correlated and a liquid state is found. For $\Gamma > 100$, the interacting potential energy dominates the kinetic energy, particles become strongly correlated and the system typically changes to a crystalline phase for $\Gamma \sim 130$.

In a 2D system of purely repulsive interacting particles the ground state configuration is found to be the hexagonal lattice [34, 35]. However, a more interesting scenario is observed if a 2D system of particles with pure repulsive interaction are arranged in a bilayer structure. In this case, the set of possible ground state configurations is richer, and many other 2D structures, not observed in the single-layer case, now appear as the minimum energy configuration. Goldoni and Peeters [36] showed that the hexagonal lattice is the ground state only when the separation between layers is zero or larger than a critical value. In the latter case, the hexagonal lattice in each layer are displaced with respect to each other (staggered hexagonal phase). For intermediate distances between the layers, staggered square, rectangular, and rhombic phases become the ground state.

In a 2D system of magnetic dipoles oriented perpendicularly to the layers, Xin Lu *et al.* [37] showed that, independently of the distance between the layers, the hexagonal phase is the minimum energy structure in each layer, and the dipoles in the different layers are aligned along the direction perpendicular to the layers (matching hexagonal phase). In addition, a reentrant melting temperature, which was related to the anisotropic nature of the dipole interaction, was predicted in this case. Magnetic 2D system of colloidal particles appear yet in many interesting recent studies [5, 24, 38, 39, 40].

Motivated by modern technical methods of synthetizing particles and the assembly of colloidal particles in controlled structures [41], we study a 2D classical bilayer system of charged magnetic dipoles directed perpendicular to the layers (which can be realized by the application of a magnetic field). Such particles have recently been produced using magnetic colloidal particles [12] with electrical stabilization [9]. Note that in an electrically stabilized colloidal system the charge of the colloids can in principle be controlled by the PH of the solution by adding/removing salt to/from the solvent [10]. Furthermore, the magnetic moment of the paramagnetic particles is tunable by the strength of the external magnetic field. In a single layer, both the Coulomb and the magnetic interaction lead to a repulsion between the particles favoring the formation of a 2D Wigner lattice. Between the layers the particles exert a repulsive Coulomb interaction while the magnetic interaction is attractive. Depending on the relative strength between the magnetic and Coulomb interaction, the particles in both layers can be either staggered or on top of each other. Here, we study the ground state configurations and the frequencies of the phonon modes as a function of the separation between the layers and a parameter which is related to the ratio between the dipole moment (μ) and the charge (Q) of the particles ($\lambda = \mu^2 n/Q^2$, with n the density of particles).

This chapter is organized as follows. In Sec. 2.2 we introduce the model, define the important parameters used to characterize the system and calculate the total energy of the system. In Sec. 2.3 the results for the ground state configurations are presented and discussed as a function of the separation between the layers and λ. In Sec. 2.4 we present the methodology used to calculate the phonon spectrum and discuss the numerical results. Our conclusions are given in Sec. 2.5.

2.2 Model

We study a two-dimensional classical crystal of charged dipole particles with total density n arranged in a bi-layer structure. The particles are evenly distributed over the layers (xy plane), which are separated by a distance d along the z-axis. Each particle has charge Q and magnetic dipole moment $\vec{\mu} = \mu\hat{e}_z$ oriented perpendicular to the layers. Thus, the inter-particle interaction consists of a repulsive Coulomb term $Q^2/|\vec{r}_1 - \vec{r}_2|$ and a dipole interaction term $\mu^2/|\vec{r}_1 - \vec{r}_2|^3$. For convenience we included the dielectric constant ϵ of the medium into Q^2 and therefore, $Q/\sqrt{\epsilon}$ is the real charge of the particles (Fig. 2.1).

In order to confine the colloidal particles in each layer into a plane we can make use of, e. g., glass plates. Because of the difference between the dielectric constants of the glass plates and the water environment in which the colloids are, it will lead to image charges as discussed in Ref. [42]. But because the dielectric constant of water ($\epsilon = 80$) is much larger than of the confining glass plates, the induced image charges have the same charge as the colloidal particles. This will have two effects: 1) the colloidal particles will be repelled by the glass plates and will therefore form a 2D layer in the middle between the two glass plates, and 2) the inter-colloid repulsive interaction will increase which can, to some extent, be modeled by replacing the charge Q by an effective charge $Q^* > Q$. Therefore, including this dielectric mismatch effect will not qualitatively modify our results.

Typically, we consider colloidal particles containing magnetic ions exhibiting paramagnetic behavior and thus a magnetic field is applied in the z-direction aligning all magnetic moments in the z-direction. The considered crystal structures are 2D lattices in which the unit cell consists of two particles, one in each layer, where we will label the lattices in different layers by A and B (Fig. 2.1). The equilibrium positions of the particles in each layer are given by $\vec{R}_A = l_1\vec{a}_1 + l_2\vec{a}_2$, and $\vec{R}_B = l_1\vec{a}_1 + l_2\vec{a}_2 + \vec{c}$, where l_1 and l_2 are integers, $\vec{a}_1$ and $\vec{a}_2$ are the primitive vectors, $\vec{c}$ is a two-dimensional vector which describes the shift of lattice B with respect to A in the xy plane. For $\vec{c} = 0$ the lattices are not displaced, and are exactly on top of each other (matched case). The case $\vec{c} \neq 0$ implies staggered lattices. Because of equal density of particles in both layers, the lattice structure in both layers is the same.

The total interaction energy is given by

$$E^t = E^t_{el} + E^t_{mag}, \tag{2.1}$$

with the Coulomb interaction energy

$$\begin{aligned} E^t_{el} =& \frac{1}{2}\sum_{R_A\neq R'_A}\frac{Q^2}{|\vec{R}_A-\vec{R'}_A|}+\frac{1}{2}\sum_{R_B\neq R'_B}\frac{Q^2}{|\vec{R}_B-\vec{R'}_B|} \\ &+\sum_{R_A,R_B}\frac{Q^2}{\sqrt{|\vec{R}_A-\vec{R}_B|^2+d^2}}, \end{aligned} \tag{2.2}$$

where d is the separation between the layers. The dipole-dipole interaction energy is

$$\begin{aligned} E^t_{mag} =& \frac{1}{2}\sum_{R_A\neq R'_A}\frac{\mu^2}{|\vec{R}_A-\vec{R'}_A|^3}+\frac{1}{2}\sum_{R_B\neq R'_B}\frac{\mu^2}{|\vec{R}_B-\vec{R'}_B|^3} \\ &+\sum_{R_A,R_B}\frac{\mu^2(|\vec{R}_A-\vec{R}_B|^2-2d^2)}{[|\vec{R}_A-\vec{R}_B|^2+d^2]^{\frac{5}{2}}}. \end{aligned} \tag{2.3}$$

Since the layers are equivalent, it is convenient to write the total energy per particle E as

$$E=\frac{E^t}{N}=E_{el}+E_{mag}, \tag{2.4}$$

where the total Coulomb (E_{el}) and magnetic (E_{mag}) energy per particle can be split as

$$E_{el}=\frac{1}{2}(E_{0E}+E_{IE}), \tag{2.5a}$$

$$E_{mag}=\frac{1}{2}(E_{0M}+E_{IM}), \tag{2.5b}$$

where

$$E_{0E}=\sum_{\vec{R}\neq\vec{0}}\frac{Q^2}{|\vec{R}|}, \tag{2.6a}$$

$$E_{0M}=\sum_{\vec{R}\neq\vec{0}}\frac{\mu^2}{|\vec{R}|^3}, \tag{2.6b}$$

are the Coulomb and magnetic interaction energy per particle in each layer, respectively, and $\vec{R}=l_1\vec{a}_1+l_2\vec{a}_2$. On the other hand,

$$E_{IE}=\sum_{\vec{R}}\frac{Q^2}{(|\vec{R}+\vec{c}|^2+d^2)^{1/2}}, \tag{2.7a}$$

$$E_{IM}=\sum_{\vec{R}}\frac{\mu^2(|\vec{R}+\vec{c}|^2-2d^2)}{(|\vec{R}+\vec{c}|^2+d^2)^{5/2}}, \tag{2.7b}$$

are the Coulomb and magnetic interaction energy per particle between particles in distinct layers, respectively. Following the procedure developed in Refs. [34, 35, 36, 37], we define the auxiliary functions (see Appendix A):

$$\begin{aligned} T_0(\vec{r},\vec{q}) &= e^{-i\vec{q}\cdot\vec{r}}\sum_{\vec{R}}\frac{e^{i\vec{q}\cdot(\vec{r}-\vec{R})}}{|\vec{r}-\vec{R}|}-\frac{1}{r}, && (2.8a)\\ T_I(\vec{r},\vec{q}) &= e^{-i\vec{q}\cdot\vec{r}}\sum_{\vec{R}}\frac{e^{i\vec{q}\cdot(\vec{r}-\vec{R}+\vec{c})}}{[|\vec{r}-\vec{R}+\vec{c}|^2+d^2]^{1/2}}, && (2.8b)\\ \psi_0(\vec{r},\vec{q}) &= e^{i\vec{q}\cdot\vec{r}}\sum_{\vec{R}\neq\vec{0}}\frac{e^{-i\vec{q}\cdot(\vec{r}+\vec{R})}}{|\vec{r}+\vec{R}|^3}, && (2.8c)\\ \psi_I(\vec{r},\vec{q}) &= e^{i\vec{q}\cdot\vec{r}}\sum_{\vec{R}}\left(\frac{e^{-i\vec{q}\cdot(\vec{r}+\vec{R}+\vec{c})}}{|\vec{r}+\vec{R}+\vec{c}|^3}+\frac{-3d^2e^{-i\vec{q}\cdot(\vec{r}+\vec{R}+\vec{c})}}{|\vec{r}+\vec{R}+\vec{c}|^5}\right). && (2.8d)\end{aligned}$$

The function $\psi_I(\vec{r},\vec{q})$ can also be written as

$$\psi_I(\vec{r},\vec{q}) = \psi_{I1}(\vec{r},\vec{q}) - 3d^2\psi_{I2}(\vec{r},\vec{q}) \tag{2.9}$$

with

$$\begin{aligned} \psi_{I1}(\vec{r},\vec{q}) &= \sum_{\vec{R}}\frac{e^{-i\vec{q}\cdot(\vec{R}+\vec{c})}}{|\vec{r}+\vec{R}+\vec{c}|^3}, && (2.10a)\\ \psi_{I2}(\vec{r},\vec{q}) &= \sum_{\vec{R}}\frac{e^{-i\vec{q}\cdot(\vec{R}+\vec{c})}}{|\vec{r}+\vec{R}+\vec{c}|^5}, && (2.10b)\end{aligned}$$

where $|\vec{r}+\vec{R}+\vec{c}| \equiv (|\vec{r}+\vec{R}+\vec{c}|^2+d^2)^{1/2}$. Using Eqs. (2.8 - 2.10) we can write Eqs. (2.6) and (2.7) as

$$\begin{aligned} E_{0E} &= Q^2\lim_{\vec{r}\to 0}T_0(\vec{r},\vec{0}), && (2.11a)\\ E_{IE} &= Q^2\lim_{\vec{r}\to 0}T_I(\vec{r},\vec{0}), && (2.11b)\\ E_{0M} &= \mu^2\lim_{\vec{r}\to 0}\psi_0(\vec{r},\vec{0}), && (2.11c)\\ E_{IM} &= \mu^2\lim_{\vec{r}\to 0}\psi_I(\vec{r},\vec{0}). && (2.11d)\end{aligned}$$

Due to the long range nature of the interactions, we use the Ewald summation method in order to improve the convergence of the energy expressions. Therefore, for the Coulomb interaction, Eqs. (2.8a) and (2.8b) are re-written as [34, 35, 36]

$$
\begin{aligned}
T_0(\vec{r},\vec{q}) &= \sqrt{n/2}\sum_{\vec{G}} e^{-i(\vec{q}+\vec{G})\cdot\vec{r}}\Phi\left(\frac{|\vec{q}+\vec{G}|^2}{2\pi n}\right) \\
&+ \sqrt{n/2}\sum_{\vec{R}\neq\vec{0}} e^{-i\vec{q}\cdot\vec{R}}\Phi(\pi n|\vec{r}-\vec{R}|^2/2) \\
&+ \sqrt{n/2}\Phi(\pi n|\vec{r}|^2/2) - \frac{1}{r}, \qquad (2.12a) \\
T_I(\vec{r},\vec{q}) &= \sqrt{n/2}\sum_{\vec{G}} e^{-i(\vec{q}+\vec{G})\cdot\vec{r}}e^{-i\vec{G}.\vec{c}}\Psi\left(\frac{|\vec{q}+\vec{G}|^2}{2\pi n},\pi\eta^2\right) \\
&+ \sqrt{n/2}\sum_{\vec{R}} e^{-i\vec{q}\cdot(\vec{R}-\vec{c})}\Phi(\pi[n|\vec{r}-\vec{R}+\vec{c}|^2/2+\eta^2]), \qquad (2.12b)
\end{aligned}
$$

where $\vec{G}$ are arbitrary reciprocal lattice vectors given by $\vec{G} = l_1\vec{b}_1 + l_2\vec{b}_2$ (l_1, l_2 are integers) and $\vec{b}_1$, $\vec{b}_2$ are the primitive translation vectors of the reciprocal lattice. The functions

$$\Phi(x) = \sqrt{\frac{\pi}{x}}\mathrm{erfc}(\sqrt{x}) \quad , \qquad (2.13)$$

and

$$
\begin{aligned}
\Psi(x,y) = \frac{1}{2}\sqrt{\frac{\pi}{x}}[e^{\sqrt{4xy}}\mathrm{erfc}(\sqrt{x} \\
+ \sqrt{y}) + e^{-\sqrt{4xy}}\mathrm{erfc}(\sqrt{x}-\sqrt{y})]
\end{aligned} \qquad (2.14)
$$

rapidly converge to zero for large values of their arguments. The term erfc(x) is the complementary error function, and $\eta = d\sqrt{n/2}$ is a dimensionless parameter proportional to the separation between the two layers. By considering Eqs. (2.13) and (2.14), Eqs. (2.11a) and (2.11b) can be written as

$$E_{0E} = Q^2\sqrt{n/2}A \quad , \qquad (2.15)$$

where

$$A = 2\sum_{\vec{R}\neq\vec{0}}\Phi(\pi n|\vec{R}|^2/2) - 4, \qquad (2.16)$$

and

$$E_{IE} = Q^2\sqrt{n/2}B(\eta), \qquad (2.17)$$

where,

$$\begin{aligned} B(\eta) = & \sum_{\vec{R}} \Phi(\pi[n|\vec{R}+\vec{c}|^2/2+\eta^2]) \\ & + \sum_{\vec{G}\neq\vec{0}} e^{-i\vec{G}\cdot\vec{c}}\Psi\left(\frac{|\vec{q}+\vec{G}|^2}{2\pi n}, \pi\eta^2\right) \\ & + 2\{\pi\eta\cdot\operatorname{erfc}(\sqrt{\pi}\eta) - e^{-\pi\eta^2}\}. \end{aligned} \tag{2.18}$$

A similar approach is considered for the magnetic interaction. In this case, following Ref. [37], the following expressions are obtained

$$\begin{aligned} \psi_0(\vec{r},\vec{q}) = & \frac{\pi n}{2}\sum_{\vec{G}} e^{i(\vec{q}+\vec{G})\cdot\vec{r}}\left[\frac{4\varepsilon}{\sqrt{\pi}}e^{-|\vec{q}+\vec{G}|^2/4\varepsilon^2}\right. \\ & \left. - 2|\vec{q}+\vec{G}|\operatorname{erfc}\left(\frac{|\vec{q}+\vec{G}|}{2\varepsilon}\right)\right] \\ & + \left[\frac{2\varepsilon e^{-\varepsilon^2 r^2}}{\sqrt{\pi}r^2} - \frac{\operatorname{erf}(\varepsilon r)}{r^3}\right] \\ & + \sum_{\vec{R}\neq\vec{0}} e^{-i\vec{q}\cdot\vec{R}}\left[\frac{\operatorname{erfc}(\varepsilon|\vec{R}+\vec{r}|)}{|\vec{R}+\vec{r}|^3}\right. \\ & \left. + \left(\frac{2\varepsilon}{\sqrt{\pi}}\right)\frac{e^{-\varepsilon^2|\vec{R}+\vec{r}|^2}}{|\vec{R}+\vec{r}|^2}\right], \end{aligned} \tag{2.19a}$$

$$\begin{aligned} \psi_I(\vec{r},\vec{q}) = & \frac{\pi n}{2}\sum_{\vec{G}} e^{i(\vec{q}+\vec{G})\cdot\vec{r}}e^{i\vec{G}\cdot\vec{c}}\left[\frac{4\varepsilon}{\sqrt{\pi}}e^{-\frac{|\vec{q}+\vec{G}|^2}{4\varepsilon^2}-\varepsilon^2 d^2}\right. \\ & - e^{-|\vec{q}+\vec{G}|d}|\vec{q}+\vec{G}|\operatorname{erfc}\left(\frac{|\vec{q}+\vec{G}|}{2\varepsilon} - \varepsilon d\right) \\ & \left. - e^{|\vec{q}+\vec{G}|d}|\vec{q}+\vec{G}|\operatorname{erfc}\left(\frac{|\vec{q}+\vec{G}|}{2\varepsilon} + \varepsilon d\right)\right] \\ & + \sum_{\vec{R}} e^{-i\vec{q}\cdot(\vec{R}+\vec{c})}\left[\frac{\operatorname{erfc}(\varepsilon|\vec{R}+\vec{c}+\vec{r}|)}{|\vec{R}+\vec{c}+\vec{r}|^3}\right. \\ & + \left(\frac{2\varepsilon}{\sqrt{\pi}}\right)\frac{e^{-\varepsilon^2|\vec{R}+\vec{c}+\vec{r}|^2}}{|\vec{R}+\vec{c}+\vec{r}|^2} - 3d^2\left(\frac{\operatorname{erfc}(\varepsilon|\vec{R}+\vec{c}+\vec{r}|)}{|\vec{R}+\vec{c}+\vec{r}|^5}\right. \\ & \left.\left. + \left(\frac{2\varepsilon}{3\sqrt{\pi}}\right)\frac{(3+2\varepsilon^2|\vec{R}+\vec{c}+\vec{r}|^2)e^{-\varepsilon^2|\vec{R}+\vec{c}+\vec{r}|^2}}{|\vec{R}+\vec{c}+\vec{r}|^4}\right)\right] \quad , \end{aligned} \tag{2.19b}$$

where $|\vec{R}+\vec{c}+\vec{r}| \equiv (|\vec{R}+\vec{c}+\vec{r}|^2+d^2)^{1/2}$, and the parameter $\varepsilon > 0$ is related to the inverse of the average distance between particles in the same layer, i.e., $\varepsilon = 1/r_0 = \sqrt{\pi n/2}$. In this case, Eqs. (2.11c) and (2.11d) can be written, respectively, as

$$E_{0M} = \mu^2 (n/2)^{3/2} C, \tag{2.20}$$

where

$$\begin{aligned} C = &\sum_{\vec{G}} \left[4\pi e^{-|\vec{G}|^2/2\pi n} - \frac{2|\vec{G}|\pi}{\sqrt{n/2}} \text{erfc}\left(\frac{|\vec{G}|}{2\sqrt{\pi n/2}} \right) \right] \\ &+ \sum_{\vec{R}\neq\vec{0}} \left[\frac{\text{erfc}(\sqrt{\pi n/2}|\vec{R}|)}{(n/2)^{3/2}|\vec{R}|^3} + \left(\frac{4}{n}\right) \frac{e^{-\pi n|\vec{R}|^2/2}}{|\vec{R}|^2} \right] - \frac{4\pi}{3}, \end{aligned} \tag{2.21}$$

and

$$E_{IM} = \mu^2 (n/2)^{3/2} D(\eta), \tag{2.22}$$

where

$$\begin{aligned} D(\eta) = &\sum_{\vec{G}} e^{i\vec{G}\cdot\vec{c}} \left[4\pi e^{-\frac{|\vec{G}|^2}{2\pi n} - \pi\eta^2} \right. \\ &- \frac{\pi|\vec{G}|}{\sqrt{n/2}} e^{-|\vec{G}|\eta/\sqrt{n/2}} \text{erfc}\left(\frac{|\vec{G}|}{2\sqrt{\pi n/2}} - \sqrt{\pi}\eta \right) \\ &\left. - \frac{\pi|\vec{G}|}{\sqrt{n/2}} e^{|\vec{G}|\eta/\sqrt{n/2}} \text{erfc}\left(\frac{|\vec{G}|}{2\sqrt{\pi n/2}} + \sqrt{\pi}\eta \right) \right] \\ &+ \sum_{\vec{R}} \left[\frac{\text{erfc}(\sqrt{\pi n/2}|\vec{R}+\vec{c}|)}{(n/2)^{3/2}|\vec{R}+\vec{c}|^3} \left(1 - \frac{6\eta^2}{n|\vec{R}+\vec{c}|^2} \right) \right. \\ &\left. + \frac{4e^{-\pi n|\vec{R}+\vec{c}|^2/2}}{n|\vec{R}+\vec{c}|^2} \left(1 - \frac{6\eta^2}{n|\vec{R}+\vec{c}|^2} - 2\pi\eta^2 \right) \right]. \end{aligned} \tag{2.23}$$

Finally, the total energy per particle defined in Eq. (2.4) can be written as

$$\frac{E}{Q^2\sqrt{n}} = \frac{1}{2\sqrt{2}}(A + B(\eta)) + \frac{\mu^2 n}{Q^2} \frac{1}{2^{5/2}} (C + D(\eta)). \tag{2.24}$$

Now we define the dimensionless parameter

$$\lambda = \frac{\mu^2 n}{Q^2} \tag{2.25}$$

which relates the density, the magnetic moment and the charge of each particle. It is a measure of the relative strength of the magnetic interaction as compared to the Coulomb interaction. In

Phases	$\frac{\vec{a}_1}{a}$	$\frac{\vec{a}_2}{a}$	$\vec{c}$	$\frac{\vec{b}_1 a}{2\pi}$	$\frac{\vec{b}_2 a}{2\pi}$	$\frac{na^2}{2}$
I. one-component hexagonal (OCH)	$(1,0)$	$(0,\sqrt{3})$	$\frac{\vec{a}_1+\vec{a}_2}{2}$	$(1,0)$	$(0,1/\sqrt{3})$	$\frac{1}{\sqrt{3}}$
II. staggered rectangular (SRect)	(1,0)	$(0,\alpha)$	$\frac{\vec{a}_1+\vec{a}_2}{2}$	(1,0)	$(0,1/\alpha)$	$\frac{1}{\alpha}$
III. staggered square (SS)	(1,0)	(0,1)	$\frac{\vec{a}_1+\vec{a}_2}{2}$	(1,0)	(0,1)	1
IV. staggered rhombic (SRhomb)	(1,0)	$(\cos\theta,\sin\theta)$	$\frac{\vec{a}_1+\vec{a}_2}{2}$	$(1,\frac{-\cos\theta}{\sin\theta})$	$(0,\frac{1}{\sin\theta})$	$\frac{1}{\sin\theta}$
V. staggered hexagonal (SH)	(1,0)	$(\frac{1}{2},\frac{\sqrt{3}}{2})$	$\frac{\vec{a}_1+\vec{a}_2}{3}$	$(1,\frac{-1}{\sqrt{3}})$	$(0,\frac{2}{\sqrt{3}})$	$\frac{2}{\sqrt{3}}$
VI. matching hexagonal (MH)	(1,0)	$(\frac{1}{2},\frac{\sqrt{3}}{2})$	0	$(1,\frac{-1}{\sqrt{3}})$	$(0,\frac{2}{\sqrt{3}})$	$\frac{2}{\sqrt{3}}$
VII. matching rectangular (MRect)	(1,0)	$(0,\alpha)$	0	(1,0)	$(0,\frac{a_1}{a_2})$	$\frac{1}{\alpha}$
VIII. matching square (MS)	(1,0)	(0,1)	0	(1,0)	(0,1)	1
IX. matching rhombic (MRhomb)	(1,0)	$(\cos\theta,\sin\theta)$	0	$(1,\frac{-\cos\theta}{\sin\theta})$	$(0,\frac{1}{\sin\theta})$	$\frac{1}{\sin\theta}$

Table 2.1: Lattice parameters of the different crystalline structures. a is the average nearest neighbor distance which is determined by the density and the configuration (see last column). For each case, $\vec{a}_1$ and $\vec{a}_2$ are the primitive lattice vectors, and $\vec{c}$ is the interlattice displacement vector. $\vec{b}_1$ and $\vec{b}_2$ are the primitive vectors of the reciprocal lattice, n is the density. The aspect ratio of phases II and VII is $\alpha = a_2/a_1$. In phases IV and IX, the angle between the lattice vectors $\vec{a}_1$ and $\vec{a}_2$ is θ.

this case, Eq. (2.24) takes the form

$$\frac{E}{Q^2\sqrt{n}} = \frac{1}{2\sqrt{2}}(A + B(\eta)) + \frac{\lambda}{2^{5/2}}(C + D(\eta)). \tag{2.26}$$

Because λ is associated with the relative strength of the dipole-dipole interaction with respect to the Coulomb interaction, it can be varied experimentally, e.g. through an external magnetic field. Notice that the total energy of the system is only a function of λ and η and therefore the zero temperature ($T = 0$) phase diagram can be represented in (λ, η)-space. The density enters only in the energy (i.e. $E_0 = Q^2\sqrt{n}$) and length ($r_0 = \sqrt{2/\pi n}$) scales of the problem and in the parameter λ.

2.3 Ground state crystal structures

In this section we present the analytical results for the structure of the $T = 0$ configurations (ground state).

The ground state configurations were obtained numerically by comparing the total energy [Eq. (2.26)] of the 9-possible crystalline structures, described in Table 2.1 (for instance, see the structures in Fig. 2.1), for both $\vec{c} = 0$ (matching) and $\vec{c} \neq 0$ (staggered) cases as a function of λ and η. From all the considered structures the one with the lowest energy is chosen as the ground state configuration associated to the particular set of parameters (λ, η).

An example of the total energy as a function of η ($\lambda = 0.04$) for the lattices shown in Table 2.1 is presented in Fig. 2.2 . Notice that the energy curves cross each other or merge with (or split away from) one another, and these facts are associated to first and second order structural

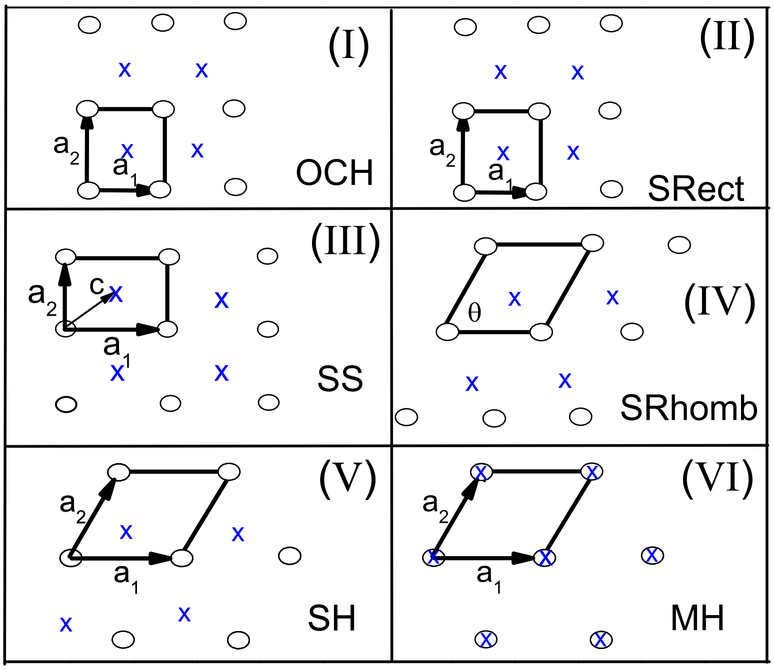

Figure 2.1: Top view of the structures of the ordered phases, where the circles (crosses) correspond to the lower (upper) layer. In the case of the matched phases, the layers are not displaced and are exactly on top of each other, as is shown for the MH phase.

phase transitions, which can be observed more clearly in Fig. 2.2(b). For a first order structural phase transition, the energy is continuous but the first derivative of the energy with respect to η is discontinuous. In this case, the energy curves associated to different structures cross each other. For a second order transition, the energy and its first derivative are continuous, but the second derivative of the energy with respect to η is discontinuous. In this case, the energy curves merge with (or split away from) one another. The transition from the staggered rhombic (SRhomb) to the staggered hexagonal (SH) phase at $\eta \approx 0.65$ is an example of a first order structural transition, while a second order structural transition is observed when the system changes from the staggered square (SS) to the SRhomb phase. Notice that such phases differ from each other only in the aspect ratio a_2/a_1 and angle θ between the primitive vectors. As shown in Fig. 2.2(c) for $\eta \approx 0.51$ the system starts to change continuously from the SS ($\sin\theta = 1$; $a_2/a_1 = 1$) to the SRhomb phase ($\sin\theta \neq 1$).

We summarize our results in the phase diagram of Fig. 2.3. The different phases are separated by solid (dotted) lines for first (second) order structural phase transitions. In the point (λ, η)=(0, 0) the system is found in the one-component hexagonal (OCH) phase, where particles are arranged in a single layer triangular lattice and the inter-particle interaction is only electrostatic. Notice that of the studied 9 phases only 6 are found to be able to become the ground state in a certain area of the (λ, η)-plane. The OCH phase is also found along the line $\eta = 0$, where the magnetic interaction is present ($\lambda \neq 0$), but in this case the inter-particle interaction is only repulsive,

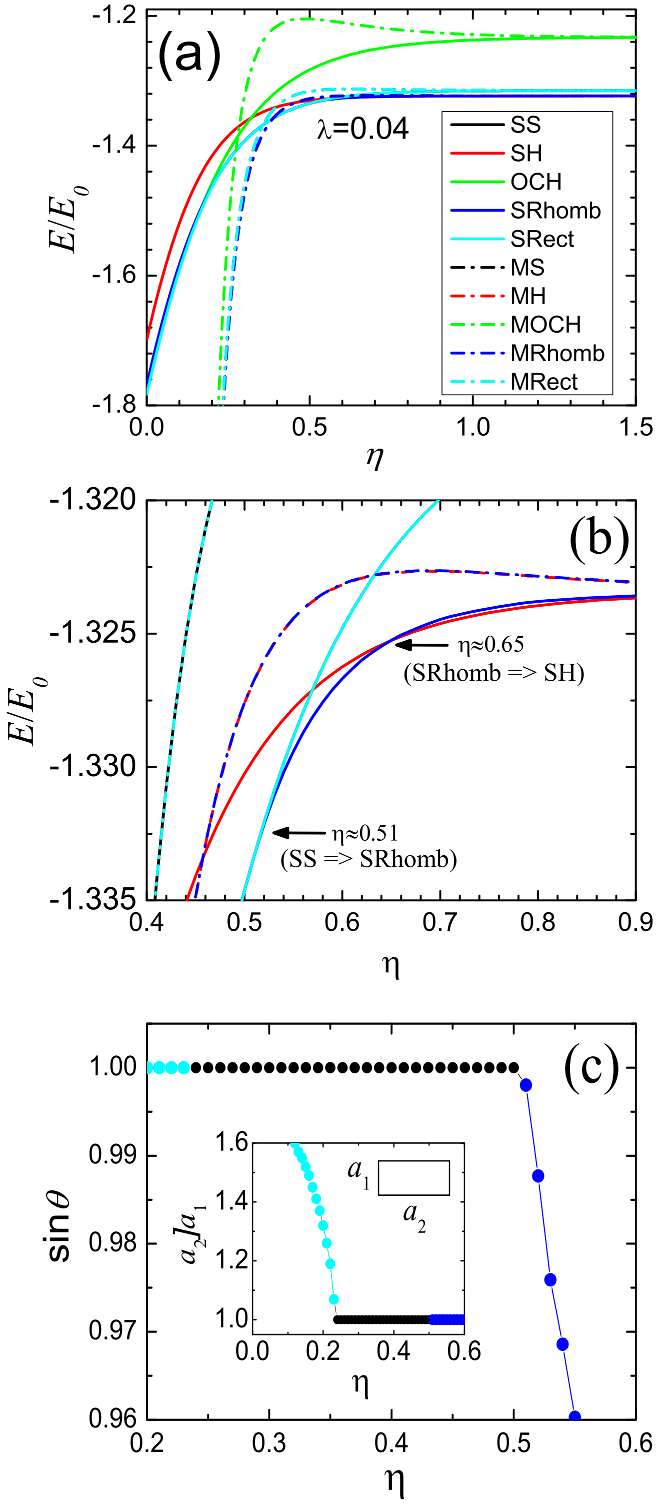

Figure 2.2: (a) The total energy per particle (in units of $E_0 = Q^2\sqrt{n}$) as function of η for the different phases presented in Table 2.1. (b) Detailed view of (a). (c) The sine of the angle between the primitive vectors $\vec{a}_1$ and $\vec{a}_2$ of the SRhomb phase as a function of η. The inset in (c) shows how the aspect ratio a_2/a_1 for the SRect phase depends on η.

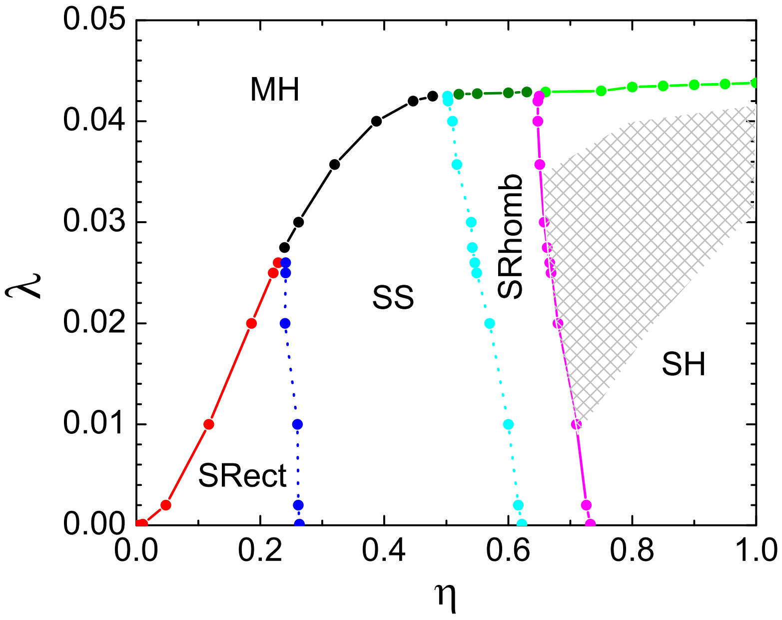

Figure 2.3: The zero temperature phase diagram where $\lambda = \mu^2 n/Q^2$ and $\eta = d\sqrt{n/2}$. First (second) order structural phase transitions are indicated by solid (dotted) lines. The labels indicating the crystalline phases are given in Table 2.1. The hatched area corresponds to the disordered phase.

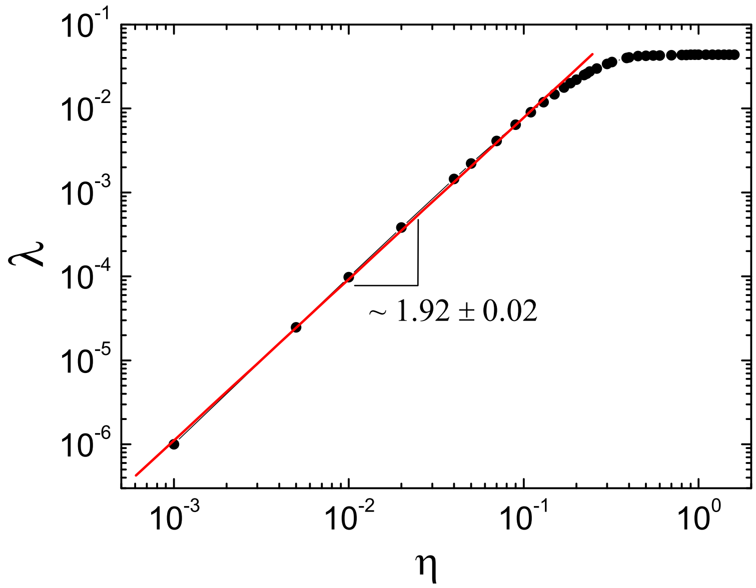

Figure 2.4: The $log \times log$ plot of the critical $\lambda(\eta)$ curve which separates the staggered phases from the MH phase taken from Fig. 2.3.

since the dipoles are all aligned along the z-axis and the inter-layer separation is zero. This is the well-known 2D Wigner crystal phase [34]. Along the $\lambda = 0$ line, the OCH phase is found only in a very small interval of η. In fact, already for $\eta = 0.006$ the OCH phase is no longer the ground state. The $\lambda = 0$ line corresponds to the case in which the inter-particle interaction is only electrostatic. In this case, the system can be found in five energetically favorable staggered configurations (phases I, II, III, IV, V - see Table 2.1) as a function of η. The latter results are in complete agreement with those discussed earlier in Ref. [36].

In general, when the magnetic interaction is taken into account ($\lambda \neq 0$), it is possible to find a configuration in which the dipoles in distinct layers are directly on top of each other (matching configuration). This phase was absent in Ref. [36] and is a consequence of the attractive magnetic interaction between the particles in different layers. We find that the matching configuration is always reached for a high enough value of λ (which is a function of η) through a first order structural transition (Fig. 2.3). In this case, the system is always found in the MH phase, where particles in distinct layers are arranged in a hexagonal lattice and their dipoles are aligned along the z-axis. Recently, Xin Lu *et al.* showed that the MH phase is the ground state configuration for a 2D classical bilayer system of dipoles oriented perpendicular to the plane of the layers, independently of the interlayer separation and density [37]. They did not include any Coulomb interaction and therefore it corresponds to the case $\lambda \to \infty$. An interesting point here is that the charging of the dipole particles allows the bilayer system to crystallize in different lattice structures which are not possible when only the magnetic dipole interaction is present.

The critical value of λ, where the system changes from a staggered (rectangular, square, rhombic, hexagonal) to the MH phase, is a monotonic increasing function of η. As seen in Fig. 2.3 we notice two distinct behaviors of $\lambda(\eta)$. Initially, there is a fast increase of λ with increasing η, followed by an almost constant $\lambda(\eta)$. Such a behavior can be qualitatively understood taking into account the range of the Coulomb and magnetic dipole inter-particle interaction. An inter-particle interaction is defined as short range if it decreases faster than $1/r^{\alpha}$, where α is the dimensionality of the system [43]. In the opposite case, the interaction is long range. In this sense the Coulomb interaction can be considered as long range and the magnetic dipole interaction as short range. For small η the separation between layers is small and the dipole interaction is dominant over the electric interaction. As a consequence, the transition to the MH phase, which is the ground state for a system with only magnetic dipole interaction, occurs for small λ. For a large enough separation between the layers the coupling between dipoles in distinct layers (the inter-layer interaction) becomes very small. For example, for $\eta = 0.8$ the inter-layer interaction is only 0.3% of the total energy. As a consequence, for high enough values of η the layers become independent, and it becomes numerically impossible to determine if the SH or MH phase is the ground state. E.g., for $\eta = 2.3$ ($\lambda \approx 0.044$) the absolute difference in energy between the SH and MH phases is of the order of 10^{-8}, which is the level of our numerical accuracy. In this case, the total energy is twice the energy of each layer, since the particles in each layer barely interact.

A more detailed analysis of the critical $\lambda(\eta)$ which defines the transition from a staggered to the MH phase identifies a clear crossover between the fast (strong coupling between dipoles in distinct layers) and slow increase of $\lambda(\eta)$. This is shown in Fig. 2.4, where a $\log \times \log$ plot of the critical $\lambda(\eta)$ curve which separates the staggered phases from the MH phase is presented. As can be seen, there is a power law increase of $\lambda(\eta)$ for $\eta \lesssim 0.15$ with exponent $\beta \sim 1.92$. Thus for $\eta \lesssim 0.2$, the critical distance between the layers scales as $d \propto (\mu/Q)^{1.04} n^{0.021}$, which indicates a weak dependence on the density and an almost linear dependence on the ratio μ/Q. This scaling behavior can be understood as follows: the interlayer dipole interaction $\sim \mu^2/d^3$ while the Coulomb interlayer interaction $\sim Q^2/d$ and therefore we expect the staggered to matched transition approximately when $Q^2/d \sim \mu^2/d^3$ and thus $\lambda \sim \eta$.

To conclude, we also present a hatched area in the (λ, η) phase diagram (Fig. 2.3). It corresponds to a disordered phase which can not be obtained from our analytical calculations. The discussions concerning such a phase will be postponed to the next section.

2.4 Dynamical Properties

Now we turn our discussion to the dynamical properties of the system. Such a study in addition will give us information on the stability of the different phases considered in the previous section.

The phonon spectra are calculated within the harmonic approximation. The phonon frequencies for a general lattice are directly obtained from the dynamical matrix through the square root of the eigenvalues. Since we are studying a 2D crystal with two particles per unit cell (one in each layer), the dynamical matrix corresponds to a 4 × 4 matrix which can be written as

$$D = \begin{pmatrix} D^{AA} & D^{AB} \\ D^{BA} & D^{BB} \end{pmatrix} \quad , \tag{2.27}$$

where D^{AA}, D^{AB}, D^{BA}, D^{BB} are 2×2 block matrices which include the intra- and inter-layer electric and magnetic interactions. The labels A and B describe the distinct layers, and each block matrix is of the form

$$[D^{\tau\nu}(\vec{q})]_{\alpha\beta} = [D^{\tau\nu}_{el}(\vec{q})]_{\alpha\beta} + [D^{\tau\nu}_{mag}(\vec{q})]_{\alpha\beta}, \tag{2.28}$$

where $\tau, \nu = A, B$; $\alpha, \beta = x, y$. Following the procedure described in Ref. [36] and by using Eqs. (2.12a), (2.12b), (2.19a), and (2.19b), the different terms present in Eq. (2.28) are given by

$$\begin{aligned}[D^{AA}_{el}(\vec{q})]_{\alpha\beta} = \frac{1}{m}\{&[S^{AA}_{el}(0)]_{\alpha\beta} + [S^{AB}_{el}(0)]_{\alpha\beta} \\ &- [S^{AA}_{el}(\vec{q})]_{\alpha\beta}\},\end{aligned} \tag{2.29a}$$

$$[D^{AB}_{el}(\vec{q})]_{\alpha\beta} = \frac{1}{m}\{-[S^{AB}_{el}(\vec{q})]_{\alpha\beta}\}, \tag{2.29b}$$

$$\begin{aligned}[D^{AA}_{mag}(\vec{q})]_{\alpha\beta} = \frac{1}{m}\{&[S^{AA}_{mag}(0)]_{\alpha\beta} + [S^{AB}_{mag}(0)]_{\alpha\beta} \\ &- [S^{AA}_{mag}(\vec{q})]_{\alpha\beta}\},\end{aligned} \tag{2.29c}$$

$$[D^{AB}_{mag}(\vec{q})]_{\alpha\beta} = \frac{1}{m}\{-[S^{AB}_{mag}(\vec{q})]_{\alpha\beta}\}, \tag{2.29d}$$

where m is the mass of each particle and

$$\begin{aligned}[S^{AA}_{el}(\vec{q})]_{\alpha\beta} &= -Q^2 \lim_{r\to 0} \partial_\alpha \partial_\beta T_0(\vec{r}, \vec{q}) \\ &= -Q^2 \sqrt{n_s} [E(\vec{q})]_{\alpha\beta} \quad ,\end{aligned} \tag{2.30a}$$

$$\begin{aligned}[S^{AB}_{el}(\vec{q})]_{\alpha\beta} &= -Q^2 \lim_{r\to 0} \partial_\alpha \partial_\beta T_I(\vec{r}, \vec{q}) \\ &= -Q^2 \sqrt{n_s} [F(\vec{q}, \eta)]_{\alpha\beta} \quad ,\end{aligned} \tag{2.30b}$$

$$\begin{aligned}[S^{AA}_{mag}(\vec{q})]_{\alpha\beta} &= -\mu^2 \lim_{r\to 0} \partial_\alpha \partial_\beta \psi_0(\vec{r}, \vec{q}) \\ &= -\mu^2 \sqrt{n_s} [G(\vec{q})]_{\alpha\beta} \quad ,\end{aligned} \tag{2.30c}$$

$$\begin{aligned}[S^{AB}_{mag}(\vec{q})]_{\alpha\beta} &= -\mu^2 \lim_{r\to 0} \partial_\alpha \partial_\beta \psi_I(\vec{r},\vec{q}) \\ &= -\mu^2 \sqrt{n_s} [H(\vec{q},\eta)]_{\alpha\beta} \quad .\end{aligned} \tag{2.30d}$$

The auxiliary functions $[E(\vec{q})]_{\alpha\beta}$, $[F(\vec{q},\eta)]_{\alpha\beta}$, $[G(\vec{q})]_{\alpha\beta}$, and $[H(\vec{q},\eta)]_{\alpha\beta}$ are given by:

$$\begin{aligned}[E(\vec{q})]_{\alpha\beta} = &- \sum_{\vec{G}} (\vec{q}+\vec{G})_\alpha (\vec{q}+\vec{G})_\beta \Phi\left(\frac{|\vec{q}+\vec{G}|^2}{4\pi n_s}\right) \\ &+ \lim_{r\to 0} \sum_{\vec{R}\neq\vec{0}} e^{-i\vec{q}\cdot\vec{R}} \partial_\alpha \partial_\beta \Phi\left(\pi n_s |\vec{r}-\vec{R}|^2\right) \\ &+ \delta_{\alpha\beta} \frac{4}{3}\pi n_s,\end{aligned} \tag{2.31a}$$

$$\begin{aligned}[F(\vec{q},\eta)]_{\alpha\beta} = &- \sum_{\vec{G}} (\vec{q}+\vec{G})_\alpha (\vec{q}+\vec{G})_\beta \\ &\times e^{-i\vec{G}\cdot\vec{c}} \Psi\left(\frac{|\vec{q}+\vec{G}|^2}{4\pi n_s}, \pi\eta^2\right) \\ &+ \lim_{r\to 0} \sum_{\vec{R}} e^{-i\vec{q}\cdot(\vec{R}-\vec{c})} \\ &\times \partial_\alpha \partial_\beta \Phi\left(\pi[n_s|\vec{r}-\vec{R}+\vec{c}|^2+\eta^2]\right) \quad ,\end{aligned} \tag{2.31b}$$

$$\begin{aligned}[G(\vec{q})]_{\alpha\beta} = &-\pi n_s \sum_{\vec{G}} (\vec{q}+\vec{G})_\alpha (\vec{q}+\vec{G})_\beta \Upsilon\left(\frac{|\vec{q}+\vec{G}|}{2\varepsilon}, 0\right) \\ &+ \lim_{r\to 0} \sum_{\vec{R}\neq\vec{0}} e^{-i\vec{q}\cdot\vec{R}} \partial_\alpha \partial_\beta \Omega_1\left(|\vec{r}+\vec{R}|\right) + \delta_{\alpha\beta} \frac{8\varepsilon^5}{5\sqrt{\pi}},\end{aligned} \tag{2.31c}$$

$$\begin{aligned}[H(\vec{q},\eta)]_{\alpha\beta} = &-\pi n_s \sum_{\vec{G}} (\vec{q}+\vec{G})_\alpha (\vec{q}+\vec{G})_\beta \\ &\times e^{i\vec{G}\cdot\vec{c}} \Upsilon\left(\frac{|\vec{q}+\vec{G}|}{2\varepsilon}, \varepsilon d\right) \\ &+ \lim_{r\to 0} \sum_{\vec{R}} e^{-i\vec{q}\cdot(\vec{R}+\vec{c})} \partial_\alpha \partial_\beta \Omega_2\left(|\vec{r}+\vec{R}+\vec{c}|\right),\end{aligned} \tag{2.31d}$$

and the functions $\Upsilon(x,y)$, $\Omega_1(x)$, and $\Omega_2(x)$ which appear in Eqs. (2.31c) and (2.31d) are:

$$\Upsilon(x,y) = \frac{4\varepsilon}{\sqrt{\pi}} e^{-x^2-y^2} + \sum_{\pm} (-2)\varepsilon x e^{\pm 2xy} \mathrm{erfc}(x \pm y) \quad , \tag{2.32a}$$

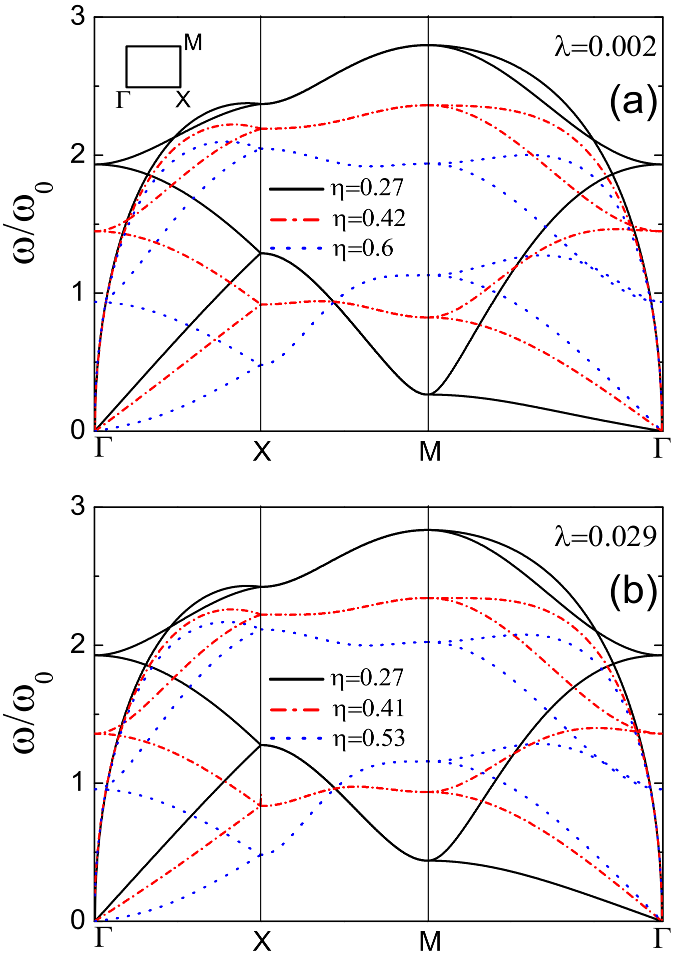

Figure 2.5: The phonon spectrum for the staggered square phase for different values of η and for (a) $\lambda = 0.002$ and (b) $\lambda = 0.029$. The high-symmetry directions of the reciprocal space are presented in the inset. The frequency is in units of $\omega_0 = Qn^{3/4}/m^{1/2}$.

$$\Omega_1(x) = \frac{\mathrm{erfc}(\varepsilon x)}{x^3} + \frac{2\varepsilon e^{-\varepsilon^2 x^2}}{\sqrt{\pi} x^2} \quad , \tag{2.32b}$$

$$\begin{aligned}\Omega_2(x) = {} & \frac{\mathrm{erfc}(\varepsilon x)}{x^3} + \frac{2\varepsilon e^{-\varepsilon^2 x^2}}{\sqrt{\pi} x^2} \\ & - 3d^2 \left[\frac{\mathrm{erfc}(\varepsilon x)}{x^5} + \frac{2\varepsilon(3 + 2\varepsilon^2 x^2) e^{-\varepsilon^2 x^2}}{3\sqrt{\pi} x^4}\right] \quad .\end{aligned} \tag{2.32c}$$

By using the relations $\varepsilon = 1/r_0 = \sqrt{\pi n_s}$, $n_s = n/2$, and $\lambda = \mu^2 n/Q^2$ the terms of the matrix given in (2.27) become

$$\begin{aligned}[D^{AA}(\vec{q})]_{\alpha\beta} = \frac{-Q^2 n^{3/2}}{m} & \left[\frac{1}{2^{3/2} n_s}\{[E(0)]_{\alpha\beta} + [F(0,\eta)]_{\alpha\beta}\right. \\ & -[E(\vec{q})]_{\alpha\beta}\} + \frac{\lambda}{(2n_s)^{5/2}}\{[G(0)]_{\alpha\beta} \\ & \left. + [H(0,\eta)]_{\alpha\beta} - [G(\vec{q})]_{\alpha\beta}\}\right] \quad ,\end{aligned}$$

$$\begin{aligned}[D^{AB}(\vec{q})]_{\alpha\beta} = \frac{Q^2 n^{3/2}}{m} & \left[\frac{1}{2^{3/2} n_s}[F(\vec{q},\eta)]_{\alpha\beta}\right. \\ & \left. + \frac{\lambda}{(2n_s)^{5/2}}[H(\vec{q},\eta)]_{\alpha\beta}\right] \quad .\end{aligned}$$

The two layers of particles are equivalent. In this case, $D^{AA} = D^{BB}$, $D^{AB} = [D^{BA}]^\dagger$, and the dynamical matrix D may now be calculated as a function of λ, $\vec{q}$, and η. In general, the dynamical matrix is complex hermitian. Therefore, it is possible to apply an unitary transformation in order to generate a real and symmetric matrix. Such a transformation is given by the matrix

$$U = \frac{1}{\sqrt{2}} \begin{pmatrix} I_2 & iI_2 \\ iI_2 & I_2 \end{pmatrix} \tag{2.33}$$

where I_2 is the 2×2 identity matrix, and

$$\begin{aligned}\bar{D} &= UDU^{-1} \\ &= \begin{pmatrix} D^{AA} + \mathrm{Im}D^{AB} & \mathrm{Re}D^{AB} \\ \mathrm{Re}D^{AB} & D^{AA} - \mathrm{Im}D^{AB} \end{pmatrix}\end{aligned} \tag{2.34}$$

where $\mathrm{Re}D^{AB}$ and $\mathrm{Im}D^{AB}$ are the real and imaginary parts of D^{AB}, respectively. Since a unitary transformation does not change the eigenvalues, we may consider now the real and symmetric matrix $\bar{D}$ in order to obtain the eigenvalues and the phonon frequencies. For each (λ,η), which specify a given structure in the phase diagram shown in Fig. 2.3, we vary the wave vector $\vec{q}$ along a given symmetry direction of the first Brillouin zone of the corresponding phases. For each value of $\vec{q}$, we generate a 4×4 matrix which gives us four eigenvalues $\omega_j^2(\vec{q})/\omega_0^2$, with $j = 1, ..., 4$ and

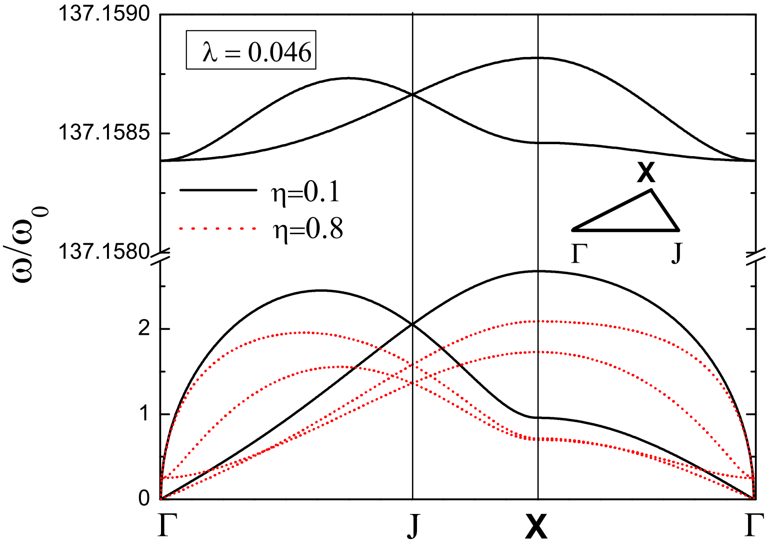

Figure 2.6: The phonon spectrum for the MH phase for different values of η and fixed λ. The high-symmetry directions of the reciprocal space are presented in the inset.

$\omega_0^2 = Q^2 n^{3/2}/m$, and for each eigenvalue a corresponding eigenvector $\vec{e}(\vec{q}, j)$ which indicates the direction of the phonon oscillation.

In our analysis of the dispersion relation we will present only frequencies which are real positive, i. e. $\omega_j^2(\vec{q})/\omega_0^2 \geq 0$. For $\omega^2 < 0$, the frequencies are imaginary, which means that the amplitudes of particle oscillation become an exponentially increasing function of time. In this case, the crystalline structure is unstable and will not exist. As commented earlier, in all phases studied in the previous section there are two particles per unit cell, one in each layer. As a consequence, there are two acoustic and optical modes which are associated to the in-phase and out-of-phase vibrations of particles in the unit cell, respectively. The acoustic branch is characterized by $\omega(\vec{q}) \to 0$ for $\vec{q} \to 0$, while in the optical branch $\omega(\vec{q}) \to$ constant in the limit $\vec{q} \to 0$. Besides, the acoustic and optical branches may also be defined as longitudinal, $\vec{e} \parallel \vec{q}$, and transverse modes [44], $\vec{e} \perp \vec{q}$. Due to the extended parameter space, we present here only some examples which illustrate the general behavior of the phonon spectrum.

In general, we find qualitative distinct behaviors for the normal mode spectra for the staggered phases and for the matching hexagonal phase. With exception of the SH phase, for a given staggered phase the phonon spectrum is almost-independent of λ, but it depends strongly on the parameter η. In addition, for a given high-symmetry direction of the reciprocal space we found a monotonic increasing (or decreasing) behavior of the phonon frequencies as a function of η. As an example, the phonon frequencies for the SS phase along the high-symmetry directions of the reciprocal space are presented in Fig. 2.5 for $\lambda = 0.002$ and $\lambda = 0.029$ and different η. The high-

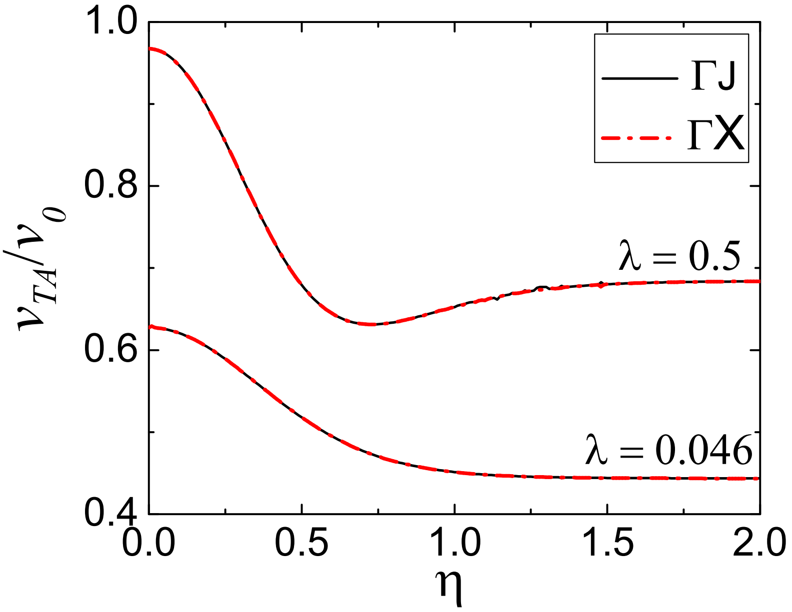

Figure 2.7: The sound velocity (in units of $v_0 = \omega_0/\sqrt{n}$) of the TA mode as a function of η for $\lambda = 0.046$ and $\lambda = 0.5$.

symmetry points in the first Brillouin zone are indicated in the insets. Notice that for both values of λ, which are one order of magnitude distinct, the same qualitative behavior is found for the phonon frequencies as a function of the wave vector. The phonons soften with increasing η along the ΓX direction. Along the XM direction, the normal mode frequencies are degenerate for any value of η. The lowest normal mode frequencies cross at a specific q-value which is independent of η. Notice that in the ΓM direction the lowest energy phonons soften with decreasing η which is the opposite behavior found along the ΓX direction.

For the MH phase, we present in Fig. 2.6, the phonon spectrum for $\lambda = 0.046$. In this case, the bilayer system is found in the MH phase for any value of η. Again the high-symmetry points in the reciprocal space are labelled in the inset. For a fixed density n, the parameter $\eta = d\sqrt{n/2}$ is directly related to the separation between the layers. For $\eta = 0.1$, a large gap between the acoustic and optical modes is observed. The later ones, which describe the out-of-phase vibrations of particles in distinct layers, are two orders of magnitude larger than the acoustic ones. Such a behavior is due to the strong dipolar magnetic interaction for small η. Notice that the dipole interaction ($\propto 1/r^3$) is dominant over the Coulomb interaction ($\propto 1/r$) for short distances r. The acoustic modes, which describe the in-phase oscillation of particles in the unit cell (distinct layers), are almost not affected by the dipole coupling. In addition the width of the optical band becomes extremely narrow. For large separation of the layers ($\eta = 0.8$) all mode frequencies have the same order of magnitude (Fig. 2.6), indicating a weaker coupling between dipoles in distinct layers. This is in agreement with the comment made in the previous section that, for $\eta = 0.8$ the inter-layer interaction is only 0.3% of the total energy. The gap between the acoustic and optical modes is observed for $\eta \lesssim 0.44$. For $\eta >> 1$ the acoustic and optical modes (transverse and longitudinal) become degenerate since the coupling between the layers becomes very small, and the system behaves as two independent single layer systems.

As shown previously for the SS phase, we also find a monotonic behavior of the phonon spectrum of the MH phase for $\lambda = 0.046$, i.e. there is a softening of the phonon frequencies with increasing η for all the high-symmetry directions of the reciprocal space. Such a behavior is interesting, since in the bilayer system with only dipole interaction, a non-monotonic behavior of the phonon spectrum was observed as a function of η [37]. Such a behavior was explained in Ref. [37] as being linked to the competitive character of the dipole-dipole interaction. In that case, the non-monotonic behavior of the phonon spectrum also revealed a non-monotonic dependence of the sound velocity on η. In addition, for $\eta \to 0$ the sound velocity is a factor $\sqrt{2}$ larger than the value obtained for $\eta >> 1$, showing that for small separations the bilayer system of dipoles behaves as a crystal of particles with twice larger dipole moment and mass. In the present bilayer system of charged dipole particles, we found that such a non-monotonic behavior for the phonon spectrum depends on the parameter λ as shown in Fig. 2.7. For $\lambda = 0.046$ the sound velocity is a monotonic function of η, but e.g. for $\lambda = 0.5$ it is non-monotonic exhibiting a minimum for $\eta = 0.73$. We found that the non-monotonic versus monotonic behavior of the sound velocity is associated to a change in the attractive/repulsive character of the total energy, i.e. it is attractive when v_{TA} is non-monotonic. This is an interesting feature, since e. g. in electrically steric colloidal systems the charge adsorbed on the colloidal particles can be controlled, for example, by changing the PH of the solution [10]. In addition, since the melting temperature can in principle be calculated from the normal mode frequencies, the non-monotonic behavior of the phonon spectrum should play an important role in the behavior of the melting temperature, which should become noticeable when varying λ.

As shown in Fig. 2.3, for $\eta \gtrsim 0.732$ ($\lambda \gtrsim 0.035$) the bilayer system can be found in either SH and MH phases, depending on λ. Note that λ can be varied either through Q or μ. Now we study how the phonon spectrum changes as a function of λ in the case the hexagonal phase is found as the ground state in each layer. This is shown in Fig. 2.8 where the phonon spectra for different values of λ are presented for $\eta = 0.8$. As shown in Fig. 2.3, a structural first order phase transition from the SH to the MH phase is observed with increasing λ. For $\lambda \gtrsim 0.0436$ the MH phase appears as the ground state. It is interesting to notice that for $\eta = 0.8$ ($\lambda = 0.046$) the layers are sufficiently far apart in order that the optical and acoustical frequencies are of the same order of magnitude, indicating a weak dipole-dipole coupling between layers. However, the magnetic interaction still plays an important role since the MH phase is found as the ground state. The optical modes are softened and the acoustical modes are hardened when the system changes

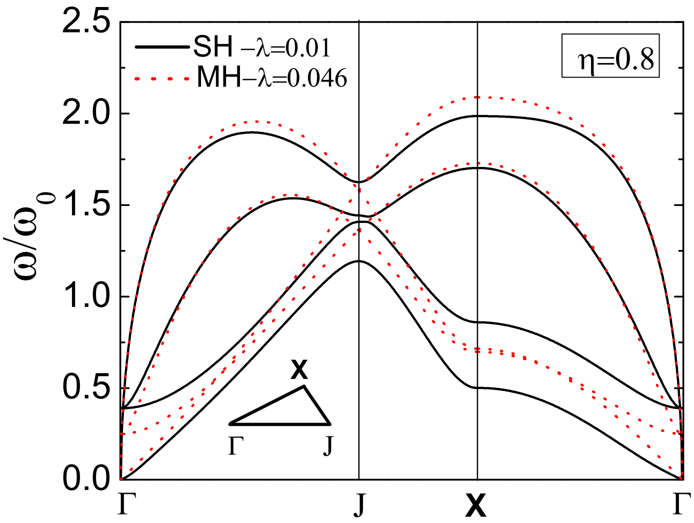

Figure 2.8: The phonon spectrum for the SH and MH phase for different λ and fixed $\eta = 0.8$. The high-symmetry direction of the reciprocal space are presented in the inset.

from the SH to the MH phase.

Now we study the interval of stability of the different phases (deduced from the phonon spectrum) and compare it with the position of the phase boundary (obtained from the minimum energy criterion).

As expected, not only the phase boundary but also the stability of the MH phase is enhanced with increasing λ in the sense that the interval of η for which the MH phase is stable, increases with increasing λ. This is shown in Fig. 2.9 for $\lambda = 0.01$ and 0.03. Notice that the stability interval of the MH phase is larger than the phase boundaries in both cases, indicating that the MH phase is metastable beyond the phase boundary. In such a case, the structural phase transition is first order. The interval of stability of the staggered phases with increasing λ depends on the crystalline structure. For the OCH, which is not found as a ground state for $\lambda \neq 0$, the interval of stability decreases with increasing λ (Fig. 2.9). For the SS phase and $\lambda = 0.03$, the interval of stability of the SS phase ($0.238 \lesssim \eta \lesssim 0.534$) becomes larger than its phase boundary ($0.262 \lesssim \eta \lesssim 0.534$) and a first order transition separates the SS and MH phases. When the SS phase is bordered by the SRect and SRhomb phases ($\lambda \lesssim 0.027$) its phase boundary and interval of stability coincide and these phases are separated by a second order structural (continuous) transition, characterized by the softening of one of the phonon mode frequencies. The SRect phase, which is suppressed as a ground state configuration for $\lambda \gtrsim 0.027$, is still stable as shown e. g. for $\lambda = 0.03$.

An interesting feature of the present system, found for $\lambda \neq 0$, is that more than two phases

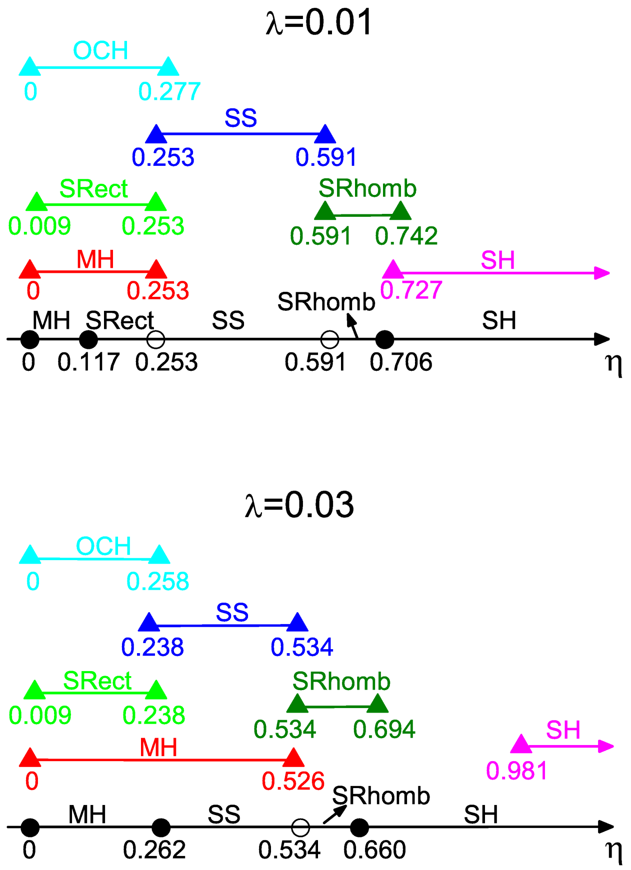

Figure 2.9: The phase boundaries (circles) and the range of stability (colored triangles) for the different phases as a function of η for two values of λ. Closed (open) circles refer to first (second) order structural phase transitions.

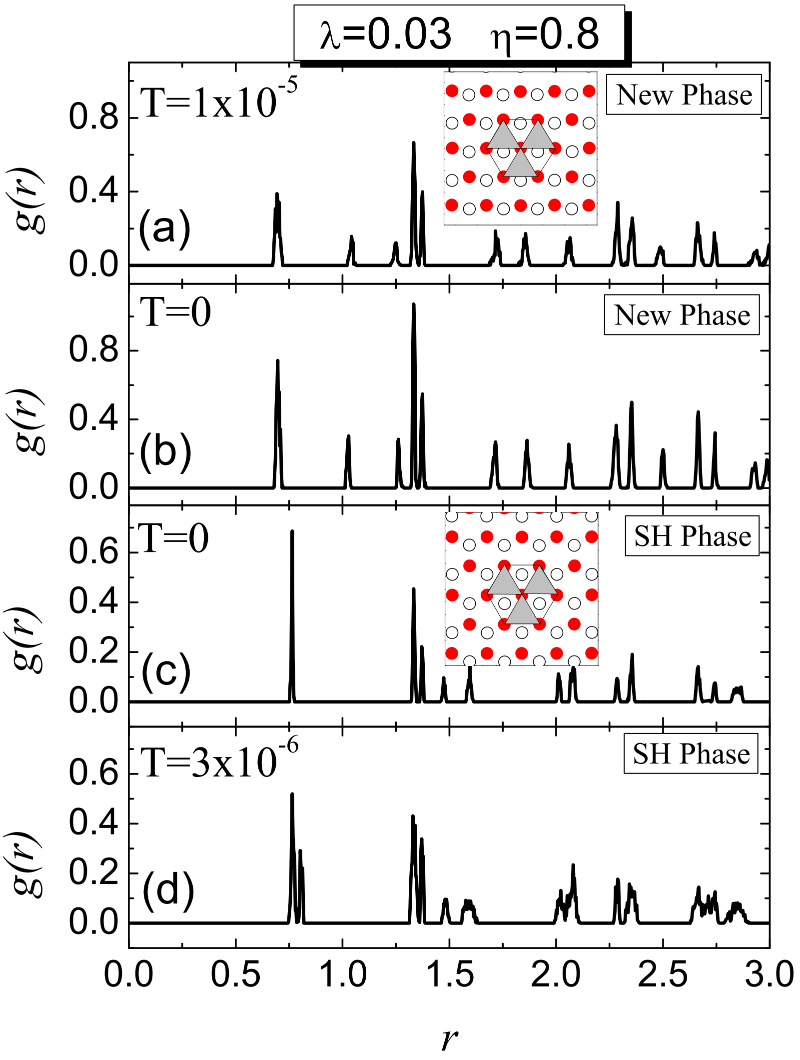

Figure 2.10: The radial distribution function as calculated from our MC simulations for the new phase and the SH phase for two different temperatures. For the new phase: (a) $T = 1 \times 10^{-5}$ and (b) $T = 0$. For the SH phase: (c) $T = 0$ and (d) $T = 3 \times 10^{-6}$. The configuration of the new phase (energy $E = -1.340575$) is presented as inset in (a), while the configuration of the SH phase (energy $E = -1.340534$) is presented as inset in (c). The $T \neq 0$ results in (a) and (d) were obtained by applying MC simulations starting with the new phase and the SH phase at $T = 0$, respectively. Solid and open circles represent particles in distinct layers.

can be stable for some interval of η. For instance, for $\eta = 0.24$ ($\lambda = 0.03$) the MH, SS and OCH phases are all stable. In contrast, for the pure Coulomb [36] and magnetic [37] systems a maximum number of two phases were found to be stable in a given interval of η. The presence of many stable phases might have important consequences for the melting temperature. In this case, structural transitions between such phases should, in principle, be possible before the system melts.

From Fig. 2.9, we see that in the large η-region (hatched) in the (λ, η) phase diagram (Fig. 2.3) there is a discrepancy between the found lowest energy structure and its stability. For $\lambda = 0.01$ we found that the SH configuration has the lowest energy for $\eta > 0.706$ while it is only stable for $\eta > 0.727$. For $\eta < 0.727$ the frequency of the transverse acoustic mode of the SH phase becomes imaginary along the ΓX and ΓJ directions. Imaginary frequency is also found for the other phases presented in Table 2.1. From this observation we are forced to conclude that in the region $0.706 < \eta < 0.727$ none of the 9 crystal structures can be the ground state. This discrepancy is even more pronounced for $\lambda = 0.03$ where the SH phase was found to be unstable in the range $0.660 < \eta < 0.981$ where (from the analytical calculations) it was initially predicted to be the ground state (Fig. 2.3). An important lesson to be learned from this stability analysis is that one has to be very careful to rely only on the most plausible crystal structures in combination with an energy minimization when deciding which phase is the ground state. In order to find the true ground state in this area of the phase diagram we resorted to a pure numerical approach.

We used Monte Carlo (MC) numerical simulations in order to find the stable ground state configuration. As an example we took $\lambda = 0.03$ and $\eta = 0.8$ and we notice from the inset of Fig. 2.10(a) that the obtained ground state configuration is similar to the SH phase (inset Fig. 2.10(c)), but the 2D displacement of one layer with respect to the other is different, i. e. $\vec{c} \neq (\vec{a}_1 + \vec{a}_2)/3$. The energy of this new phase is slightly lower, i.e. the difference with the SH phase is $\Delta E \approx 10^{-5}$.

To test numerically the stability of the new configuration (inset of Fig. 2.10(a)) we compare the $T = 0$ and $T \neq 0$ pair distribution functions $g(r)$ calculated from the MC simulations. See that $g(r)$ contains both the inter-layer ($g_{12}(r)$) and the intra-layer ($g_{ii}(r)$) radial distribution, where the latter takes into account only the inplane component. As can be observed from Fig. 2.10(a) the $g(r)$ function remains almost unaltered when we increase T slightly, indicating the thermal stability of the phase. That the SH phase is indeed unstable we tested by using our MC simulations and let the program run for $T \neq 0$. Notice that the $g(r)$ for $T = 0$ and the one for very low temperature $T = 3 \times 10^{-6}$ are different (Figs. 2.10(c) and (d)). There is a clear disordering of the lattice which indicates that very small thermal fluctuations destroy already the SH phase and consequently the SH phase is indeed unstable.

From the inset of Fig. 2.10(a) it appears that in the new phase both lattices are slightly shifted with respect to each other. This is reflected in $g(r)$ where the first peak now appears at a slightly smaller r value and there is a second peak for $r \approx 1$ which is not present in the SH phase. These

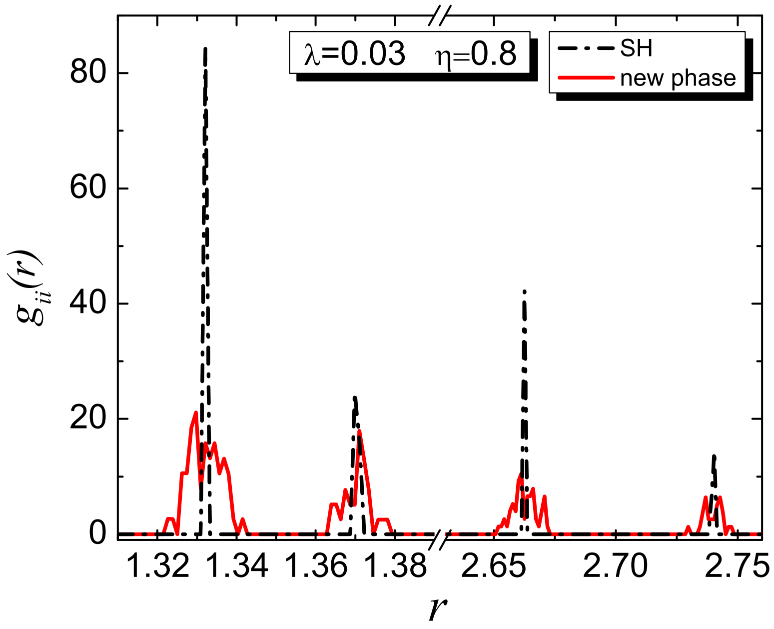

Figure 2.11: The radial distribution function as calculated from our MC simulations ($T = 0$) taking into account only one layer of the SH phase (dash-dotted black curve) and one layer of the new phase (solid red curve).

two peaks reflect only the short range inter-layer ordering. In fact, a more careful analysis reveals that the new phase does not consists of a perfect hexagonal configuration in each layer. This can be seen in Fig. 2.11 where a comparison between the pair distribution functions $g_{ii}(r)$ calculated in each layer of the new phase and the one calculated in each layer of the SH phase is presented in two narrow ranges of r. The difference observed in the $g_{ii}(r)$ functions between both phases indicates that the new phase does not consist of a perfect hexagonal lattice in each layer. Notice that for each peak of the SH phase, there appear many peaks (or a broadening of the hexagonal lattice peak) of the new phase around it, which indicates that the lattice is distorted (or strained).

2.5 Conclusions

We studied a 2D classical bilayer system of charged magnetic dipoles. The phase diagram at $T = 0$, as well as the phonon spectra were obtained through minimization of the energy and within the harmonic approximation, respectively. We obtained a very rich phase diagram at $T = 0$ with six different crystalline structures, being five staggered phases (OCH, SS, SRect, SRhomb, SH), which were previously found as the ground state configuration when no magnetic interaction is present [36], and a MH phase, which was obtained as the only ground state configuration for the bilayer system of dipoles aligned perpendicularly to the layers [37]. Notice that the presence of both Coulomb and magnetic interaction allows the appearance of phases which were not found in the pure Coulomb (MH phase) and magnetic systems (staggered phases). In the latter, the charges on the dipole particles allow the bilayer system to crystallize in different lattice structures which are not possible when only the magnetic dipole interaction is present, e.g. the SH and SRhomb phases appear not stable for any interval of η. The phase diagram was obtained as a function of the separation between the layers (η), and a parameter (λ) which is associated to the relative strength of the magnetic and Coulomb interaction between the particles. We found that the staggered phase boundaries depend on λ, e.g., the SRect phase is no longer the ground state for $\lambda \gtrsim 0.027$.

The phonon spectrum of the different phases given in the (λ, η) phase diagram were obtained. With the exception of the SH phase, we found that for a given staggered phase the phonon spectrum has the same qualitative behavior for different λ, but depend sensitively on the separation between the layers η. For the MH phase, there is a strong dependence of the phonon spectrum on η. For small η, the optical frequencies become very large due to the strong coupling between dipoles in the distinct layers. In addition, the optical band becomes very narrow. Also, a non-monotonic behavior of the phonon spectrum as a function of λ was found for the MH phase, which is related to the competition between the dipole and the Coulomb interaction [37]. We found that the non-monotonic behavior of the phonon spectrum is associated to a prevalence of the attractive over the repulsive character of the total energy, through an analysis of the sound velocity behavior. Notice that in electrically steric colloidal systems the charge adsorbed on the colloidal particles can be controlled, for example, by changing the pH of the solution [10]. In this case, for a large enough separation between the layers, where only the MH and SH phases are found as ground state, it is possible to tune the configuration between staggered and matching by changing e.g. the charge on the particles (fixed μ) and, consequently, λ. Alternatively we may change the magnetic field strength in order to tune the value of λ. In addition, since the melting temperature can, in principle, be calculated from the normal mode frequencies (at least within the harmonic approximation), the non-monotonic behavior of the phonon spectrum might play an important role when determining the melting temperature for different λ.

The stability of the phases obtained from the phonon spectrum were compared with the phase boundaries for different values of (λ, η). In particular, the MH phase is enhanced with increasing λ, in the sense that a larger phase boundary and interval of stability is observed. The SRect phase, which is no longer observed as ground state configuration for $\lambda \gtrsim 0.027$ still appears as a metastable configuration. As an important finding, the presence of both electric and magnetic interaction stabilizes up to three phases in some η-interval of a given ground state configuration, and this fact should have profound implications on the melting temperature, since structural transitions may take place for temperatures $T \neq 0$.

We found a region in the (λ, η) phase diagram where the SH phase has the lowest energy among the considered 9 crystal structures while from the phonon spectrum it appears to be unstable. Monte Carlo simulations were used to determine the ordered structure in this region, and we found that the lowest energy configuration corresponds to a distorted hexagonal lattice structure.

In this chapter, we studied the system at zero temperature. Initially, to obtain the structural phase diagram, we calculated the energy of the system considering all the particles rigorously static at the equilibrium positions of each considered crystalline structure. Then, we studied the stability of the system in the harmonic approximation, where the particles execute small oscillations around the equilibrium positions. In the next chapter, we will address the study of the system at nonzero temperature. We will calculate the melting temperature of the system as a function of η and λ, within the harmonic approximation and using the modified Lindemann criterion.

Chapter 3

Melting of a classical bilayer crystal of charged magnetic dipoles

3.1 Introduction

Since Eugene P. Wigner, in 1934, pointed out the crystallization of a three-dimensional (3D) electron gas (Wigner crystal - WC) for low densities and temperatures [17], a large body of investigations occured in the last decades in order to understand the melting scenario of the WC. Because the three-dimensional WC was not observed experimentally so far, due to imperfections and defects in real structures, the investigations were addressed to 2D electron gas on the surface of the liquid helium, since it is free of traps and scattering centers [45]. Therefore, several theoretical works arose in order to estimate the melting temperature of the 2D WC [46, 47, 48, 49]. Experimental evidence of a solid-liquid transition of the bi-dimensional WC was presented in 1979 by Grimes and Adams [50], for electrons on the liquid-He surface for low temperatures and high densities.

Another interesting system is the electron gas in a bilayer structure. Unlike the monolayer WC which has only one structural phase, namely, the hexagonal lattice, the bilayer electron gas (BLEG) has five structural phases: one-component hexagonal and staggered square, rectangular, rhombic and hexagonal [36, 51]. The melting scenario of the BLEG was investigated using the modified Lindemann criterion within the harmonic approximation [36] as well as Monte Carlo technique [52, 53]. A bilayer system of dipoles was also investigated and it was shown that the matching hexagonal phase (MH - two hexagonal crystals positioned on top of each other) is the only ground-state configuration [37]. Furthemore, the melting scenario was obtained by use of the modified Lindemann criterion and within the harmonic approach. A re-entrant melting behavior in the form of solid-liquid-solid-liquid transitions, at fixed temperature, of the MH phase was observed and explained as being due to the attractive part of the dipole-dipole interaction [37].

Currently, the term Wigner crystal is also used in non-electronic systems, specially in colloidal systems, in order to designate the crystalline state of strongly interacting colloidal particles.

In experiments of 2D colloidal systems the particles are observed by video microscopy and image processing [55, 4, 65]. As a consequence, the trajectories of the colloidal particles and, therefore, the crystallization and the solid-liquid transition can be observed in real time [4]. Moreover, the interactions between colloidal particles can be controlled experimentally. For instance, in a 2D colloidal system consisting of superparamagnetic colloidal particles of diameter 4.5 μm, confined by gravity at a flat water-air interface of a pending water droplet, the dipole-dipole interaction and, hence, the melting scenario are controllable by an external magnetic field [14, 4]. Furthermore, in an electrically stabilized colloidal system the charge of the colloids and, therefore, the charge-charge interaction can be controlled, for example, by the pH of the solution by adding (removing) salt to (from) the solvent [10].

Recently, a 2D classical bilayer crystal of charged magnetic dipoles in a configuration in which the dipole moments are all oriented perpendicularly to the layers (which can be realized by the application of an external magnetic field) was studied [56]. Such particles have recently been produced using magnetic colloidal particles [57] with electrical stabilization [58]. Six ordered structural phases and one disordered phase were found to be the ground-state configurations as a function of the separation between the layers (η) and a parameter which is related to the ratio between the dipole moment (μ) and the charge (Q) of the particles ($\lambda = \mu^2 n/Q^2$, with n the density of particles). The ordered phases are: one-component hexagonal (OCH), found when there is no separation between the layers ($\eta = 0$); staggered square (SS), rectangular (SRect), rhombic (SRhomb), hexagonal (SH); matching hexagonal (MH), and a disordered phase (DP) [56]. The staggered phases correspond to the case where the crystalline lattices in both layers are displaced with respect to each other along the plane. In this chapter, we will focus on the melting of the six ordered structural phases of the bilayer system of charged magnetic dipoles. To this aim, we resort on the modified Lindemann criterion (appropriated for 2D systems) and on the harmonic approximation in order to calculate the phonons.

The present chapter is organized as follows. In Sec. 3.2, the details of the analytical calculations are shown. In Sec. 3.3, the results for the melting are presented and discussed as a function η and λ. Our conclusions are given in Sec. 3.4.

3.2 Classical melting

At low temperatures, the particles of the crystal execute small vibrations (by comparison with the mean distance between the particles) around its equilibrium positions. When the crystal is connected with a thermal reservoir at a temperature T, the crystal receives energy and the displacement ($\vec{u}$) of the particles around its equilibrium positions becomes larger. When this displacement becomes of the order of the mean distance between the particles (r_0) the concept of a solid phase becomes nonsense. Therefore, it is expected that a solid-liquid transition takes place and a natural question would be: when the solid-liquid transition initiate? In order to solve this problem, Frederick A. Lindemann, in 1910, proposed that the melting occurs when the mean square displacement exceeds a threshold value of the mean interparticle distance (r_0) [59, 60]. In other words, the Lindemann criterion states that, for a given structural phase, the melting occurs when [36, 61, 37]

$$\frac{< u^2 >}{r_0^2} = \delta^2 \quad , \tag{3.1}$$

where δ^2 is a parameter which is obtained numerically using, for example, molecular dynamics simulation, and the symbol $<>$ stands for a thermal average. However, the Lindemann criterion is not appropriated for 2D crystals because $< u^2 >$ diverges [36, 61]. On the other hand, in 1985, V. M. Bedanov, G. V. Gadiyak and Yu. E. Lozovik showed through molecular dynamics simulation [61] that the relative mean square displacement given by

$$< |\vec{u}(\vec{R}) - \vec{u}(\vec{R} + \vec{a})|^2 > \quad , \tag{3.2}$$

is constant, where $\vec{u}(\vec{R})$ and $\vec{u}(\vec{R} + \vec{a})$ are the displacement vectors at site $\vec{R}$ and at its nearest-neighbor site $\vec{R}+\vec{a}$, respectively, and $\vec{a}$ is the lattice parameter. Therefore, a modified Lindemann-like criterion for 2D crystals is defined as

$$\frac{< |\vec{u}(\vec{R}) - \vec{u}(\vec{R} + \vec{a})|^2 >}{r_0^2} = \delta_m^2 \quad . \tag{3.3}$$

Because the value of the parameter δ_m^2 for several types of interactions in 2D classical crystals (including dipole and Coulomb interactions) is around $\delta_m^2 = 0.1$, we will take this value in the calculations of the melting temperature of the present system.

3.2.1 Analytical calculations

In this section we present the analytical calculations of the correlation function $< |\vec{u}(\vec{R}) - \vec{u}(\vec{R}+\vec{a})|^2 >$ in order to estimate the melting temperature of the system. The correlation function is obtained within the harmonic approximation and considering the nearest neighbors in each layer. The structures in the phase diagram depend on λ and η, and six ordered structural phases can be found. As a consequence, the number and the distance of the nearest neighbors changes with these parameters. Furthermore, following Refs. [36] and [37], it is convenient to define two correlations functions Δu_{AA} and Δu_{AB}, which involve the nearest neighbors in the same layer and in different layers, respectively:

$$\Delta u_{AA} = \frac{1}{N_A} \sum_{\alpha=x,y} \sum_{l=1}^{N_A} < |u_\alpha^A(0) - u_\alpha^A(l)|^2 > \quad , \tag{3.4}$$

and

$$\Delta u_{AB} = \frac{1}{N_B} \sum_{\alpha=x,y} \sum_{l=1}^{N_B} < |u_\alpha^A(0) - u_\alpha^B(l)|^2 > \quad , \tag{3.5}$$

where $u_\alpha^A(l)$ ($u_\alpha^B(l)$) is the αth component of the displacement vector of the lth nearest neighbor in the layer A (B), and N_A and N_B are the number of nearest neighbors in the layer A and B, respectively. Using the normal coordinates transformation [37, 62]

$$u_\alpha^A(0) = \frac{1}{\sqrt{Nm}} \sum_{\vec{q},j} e_\alpha^A(\vec{q},j) Q(\vec{q},j) \quad , \tag{3.6}$$

$$u_\alpha^A(l) = \frac{1}{\sqrt{Nm}} \sum_{\vec{q},j} e_\alpha^A(\vec{q},j) Q(\vec{q},j) e^{i\vec{q}.\vec{R}_A(l)} \quad , \tag{3.7}$$

where m is the mass of the particle, N the number of unit cells of the crystal, $e_\alpha^A(\vec{q},j)$ is the αth component of the eigenvector of the jth normal mode in layer A for the wave vector $\vec{q}$, $Q(\vec{q},j)$ the normal coordinate of the vibrational mode, and $\vec{R}_A(l)$ is the relative vector connecting one particle at the origin to its lth nearest neighbor in layer A. From the fact that the thermal average of $Q(\vec{q},j)Q^*(\vec{q}^{'},j^{'})$ is given by [36, 37]

$$< Q(\vec{q},j)Q^*(\vec{q}^{'},j^{'}) >= \frac{k_B T}{\omega^2(\vec{q},j)} \delta_{\vec{q}\vec{q}'} \delta_{jj'} \tag{3.8}$$

where k_B is the Boltzmann constant and T is the temperature of the system, we obtain

$$< |u_\alpha^A(0) - u_\alpha^A(m)|^2 >= \frac{4k_B T}{Nm} \sum_{\vec{q},j} \frac{[e_\alpha^A(\vec{q},j)]^2}{\omega^2(\vec{q},j)} \sin^2 \frac{\vec{q}.\vec{R}_A(l)}{2} \quad . \tag{3.9}$$

Therefore, the expression for Δu_{AA} results

$$\Delta u_{AA} = \frac{4k_B T}{NmN_A} \Gamma_{AA} \quad , \tag{3.10}$$

with

$$\Gamma_{AA} = \sum_{\vec{q},j} \frac{[e_x^A(\vec{q},j)]^2 + [e_y^A(\vec{q},j)]^2}{\omega^2(\vec{q},j)} \sum_{l=1}^{N_A} \sin^2 \frac{\vec{q}.\vec{R}_A(l)}{2} \quad . \tag{3.11}$$

Following the same procedure for $< |u_\alpha^A(0) - u_\alpha^B(l)|^2 >$, where $u_\alpha^B(l)$ is given by

$$u_\alpha^B(l) = \frac{1}{\sqrt{Nm}} \sum_{\vec{q},j} e_\alpha^B(\vec{q},j) Q(\vec{q},j) e^{i\vec{q}.\vec{R}_B(l)} \quad , \tag{3.12}$$

we find

$$\begin{aligned} < |u_\alpha^A(0) - u_\alpha^B(l)|^2 > \; &= \; \frac{k_BT}{Nm}\sum_{\vec{q},j}\frac{[e_\alpha^A(\vec{q},j)]^2+[e_\alpha^B(\vec{q},j)]^2}{\omega^2(\vec{q},j)} \\ &\quad -\frac{2k_BT}{Nm}\sum_{\vec{q},j}\frac{e_\alpha^A(\vec{q},j)e_\alpha^B(\vec{q},j)}{\omega^2(\vec{q},j)} \\ &\quad \times\cos\vec{q}.\vec{R}_B(l) \end{aligned} \qquad (3.13)$$

and the equation for Δu_{AB} is written as

$$\Delta u_{AB} = \frac{k_BT}{NmN_B}\Gamma_{AB} \quad , \qquad (3.14)$$

with

$$\begin{aligned} \Gamma_{AB} \; &= \; \sum_{l=1}^{N_B}\sum_{\vec{q},j}\frac{1}{\omega^2(\vec{q},j)}\Big[1-2\cos\vec{q}.\vec{R}_B(l) \\ &\quad \times\{e_x^A(\vec{q},j)e_x^B(\vec{q},j)+e_y^A(\vec{q},j)e_y^B(\vec{q},j)\}\Big] \quad . \end{aligned} \qquad (3.15)$$

Moreover, following Refs. [36] and [37] we write the correlation function as

$$< |\vec{u}(\vec{R}) - \vec{u}(\vec{R}+\vec{a})|^2 >= \Delta u_{AA} + f(\eta)\Delta u_{AB} \qquad (3.16)$$

where $f(\eta)$ takes into account the influence of the vibrations of the particles in one layer on the vibrations of the particles in the other layer. Besides, $f(\eta)$ is taken to be proportional to the in-plane component of the force between two nearest neighbors in different layers, and it has to fulfill the following conditions:

$$f(\eta = 0) = 1 \qquad (3.17)$$

and

$$f(\eta = \infty) = 0 \qquad (3.18)$$

where the first condition means that there is no distinction between the nearest neighbors and second one means that the vibration in one layer is not affected by the vibration in the other layer.

For the staggered ordered structures in the $T = 0$ phase diagram, the in-plane component of the force between two nearest neighbors in different layers is given by

$$F_\parallel(d) = F_\parallel^{el}(d) + F_\parallel^{mag}(d) \qquad (3.19)$$

where

$$F_\parallel^{el}(d) = \frac{Q^2c}{(c^2+d^2)^{3/2}} \quad , \qquad (3.20)$$

$$F_{\parallel}^{mag}(d) = \frac{3\mu^2 c}{(c^2+d^2)^{5/2}} - \frac{15\mu^2 d^2 c}{(c^2+d^2)^{7/2}} \quad . \tag{3.21}$$

Furthermore, from the definitions

$$\alpha_p = \frac{1}{n_s c^2} \tag{3.22}$$

and $\eta = d\sqrt{n_s}$, we obtain

$$\begin{aligned} F_{\parallel}(d) &= \frac{Q^2}{c^2(1+\alpha_p\eta^2)^{3/2}} + \frac{3\mu^2}{c^4(1+\alpha_p\eta^2)^{5/2}} \\ &\quad -\frac{15\mu^2 d^2}{c^6(1+\alpha_p\eta^2)^{7/2}} \quad . \end{aligned} \tag{3.23}$$

Now we write $f(\eta)$ as

$$f(\eta) = \frac{F_{\parallel}(d)}{Q^2/c^2} \quad , \tag{3.24}$$

with

$$\begin{aligned} f(\eta) &= \frac{1}{(1+\alpha_p\eta^2)^{3/2}} + \frac{3\mu^2}{Q^2c^2(1+\alpha_p\eta^2)^{5/2}} \\ &\quad -\frac{15\mu^2 d^2}{Q^2c^4(1+\alpha_p\eta^2)^{7/2}} \quad . \end{aligned} \tag{3.25}$$

Substituting $\lambda = \mu^2 n/Q^2$, $\eta = d\sqrt{n_s}$, $\alpha_p = 1/n_s c^2$ and $n_s = n/2$ into Eq. (3.25), $f(\eta)$ becomes

$$f(\eta) = f^{el}(\eta) + \frac{3\lambda\alpha_p}{2} f^{mag}(\eta) \tag{3.26}$$

with

$$f^{el}(\eta) = \frac{1}{(1+\alpha_p\eta^2)^{3/2}} \quad , \tag{3.27}$$

$$f^{mag}(\eta) = \frac{1}{(1+\alpha_p\eta^2)^{5/2}} - \frac{5\alpha_p\eta^2}{(1+\alpha_p\eta^2)^{7/2}} \quad , \tag{3.28}$$

where α_p is a dimensionless parameter which depends on the considered structure, and can be calculated from the lattice parameters of each structure. In order to satisfy the conditions (3.17) and (3.18), we write $f(\eta)$ as:

$$f(\eta) = f^{el}(\eta) + \frac{3\lambda\alpha_p(1-\delta_{\eta,0})}{2} f^{mag}(\eta) \tag{3.29}$$

where $\delta_{\eta,0}$ is the Kronecker delta.

On the other hand, for the matched structures in the $T = 0$ phase diagram, $F_{\parallel}(d)$ is written as

$$F_{\parallel}^{el}(d) = \frac{Q^2 a}{(a^2+d^2)^{3/2}} \quad , \tag{3.30}$$

$$F_{\parallel}^{mag}(d) = \frac{3\mu^2 a}{(a^2+d^2)^{5/2}} - \frac{15\mu^2 d^2 a}{(a^2+d^2)^{7/2}} \quad , \tag{3.31}$$

where a is the lattice parameter. Besides, α_p in the Eq. (3.22), now is given by

$$\alpha_p = \frac{1}{n_s a^2} \quad . \tag{3.32}$$

Substituting (3.16) into (3.3), with $\delta_m = 0.1$, $r_0^2 = 1/\pi n_s$, and the expressions for Δu_{AA} (Eq. (3.10)) and Δu_{AB} (Eq. (3.14)), we have

$$(\Delta u_{AA} + f(\eta)\Delta u_{AB})\pi n_s = 0.1 \tag{3.33}$$

$$\frac{\pi n_s 4 k_B T_M}{N m N_A}\Gamma_{AA} + f(\eta)\frac{\pi n_s k_B T_M}{N m N_B}\Gamma_{AB} = 0.1 \quad , \tag{3.34}$$

where T_M is the melting temperature of the crystal. As $n_s = n/2$, where n is the total density, we obtain

$$\frac{\pi n}{2}\frac{k_B T_M}{N m}\left[\frac{4\Gamma_{AA}}{N_A} + \frac{f(\eta)\Gamma_{AB}}{N_B}\right] = 0.1 \quad . \tag{3.35}$$

The expression in the last equation can be re-written as

$$\frac{\pi n}{2}\frac{k_B T_M}{N m} = \frac{\pi^{3/2}}{2N}\frac{Q^2 n^{3/2}}{m}\frac{k_B T_M}{Q^2\sqrt{\pi n}} \quad . \tag{3.36}$$

Now we use the dimensionless parameter $\Gamma = Q^2\sqrt{\pi n}/k_B T_M$, which indicates the solid-liquid transition, where Q is the particle charge and n is the total density. Using the characteristic frequency $\omega_1 = \sqrt{Q^2 n^{3/2}/m}$, the Eq. (3.36) becomes

$$\frac{\pi n}{2}\frac{k_B T_M}{N m} = \frac{\pi^{3/2}}{2N}\frac{\omega_1^2}{\Gamma} \quad . \tag{3.37}$$

Therefore, substituting (3.37) into (3.35), the expression for Γ becomes,

$$\Gamma = \frac{20\pi^{3/2}\omega_1^2\Gamma_{AA}}{N N_A} + \frac{5\pi^{3/2}\omega_1^2 f(\eta)\Gamma_{AB}}{N N_B} \tag{3.38}$$

From the definitions of Γ_{AA} (Eq. (3.11)) and Γ_{AB} (Eq. (3.15)) we finally obtain

$$\begin{aligned}\Gamma \;=\; & \frac{20\pi^{3/2}}{NN_A}\sum_{\vec{q},j}\left[\frac{[e_x^A(\vec{q},j)]^2+e_y^A(\vec{q},j))]^2}{\omega^2(\vec{q},j)/\omega_1^2}\right] \\ & \times\sum_{l=1}^{N_A}\sin^2\left(\frac{\vec{q}.\vec{R}_A(l)}{2}\right) \\ & +\frac{5\pi^{3/2}f(\eta)}{NN_B}\sum_{\vec{q},j}\frac{1}{\omega^2(\vec{q},j)/\omega_1^2} \\ & -\frac{10\pi^{3/2}f(\eta)}{NN_B}\sum_{\vec{q},j}\left[\frac{e_x^A(\vec{q},j)e_x^B(\vec{q},j)+e_y^A(\vec{q},j)e_y^B(\vec{q},j)}{\omega^2(\vec{q},j)/\omega_1^2}\right] \\ & \times\sum_{l=1}^{N_B}\cos\vec{q}.\vec{R}_B(l) \qquad (3.39)\end{aligned}$$

and we recall that $\omega^2(\vec{q},j)/\omega_1^2$ $(j = 1, ..., 4)$ and $\vec{e}(\vec{q},j)$ are the eigenvalues and the eigenvectors of the dynamical matrix (calculated within the harmonic approach), respectively.

3.3 Results and discussion

In this section, we show the results for the melting of the ordered phases presented in Fig. 2.1.

In Fig. 3.1 we present the melting temperature for $\lambda = 0.01$ and $\lambda = 0.03$ as a function of η. For $\lambda = 0.01$ and $\lambda = 0.03$, we have five phases and four phases energetically favorable, respectively [56]. Besides, we plot the interval of η where the phases are energetically favorable (phase boundaries). The first thing we observe is that, in general, for a given λ, e. g., $\lambda = 0.01$ or $\lambda = 0.03$ the maximum melting temperature of each phase diminishes when the distance between the layers (η) increases due to decrease of the interaction energy between the charged magnetic dipoles. For the MH phase we have that the higher the λ, the greater is the melting temperature. Furthermore, the melting temperature of the MH phase is considerably larger than that of the other phases. The reason for this fact is the strong coupling between the magnetic dipoles. As a consequence, more energy is necessary to dissolve the MH phase than to dissolve the other structural phases. Another interesting thing we observe in Figs. 2 and 3 is that when the system suffers a first order structural transition (discontinuous) the melting temperature exhibits a jump. For instance, for $\lambda = 0.01$, from MH phase to SRect, and for $\lambda = 0.03$, from MH phase to SS, this behavior can clearly be observed.

In Fig. 3.2, we present the melting temperature as a function of λ, for $\eta = 0.8$. I. e., we fixed the separation between the layers and study the melting temperature in terms of the relative interaction between the particles. For $\eta = 0.8$, we found before [56] three different stable ground-state configurations - SH, MH and a disordered phase. The SH phase becomes unstable

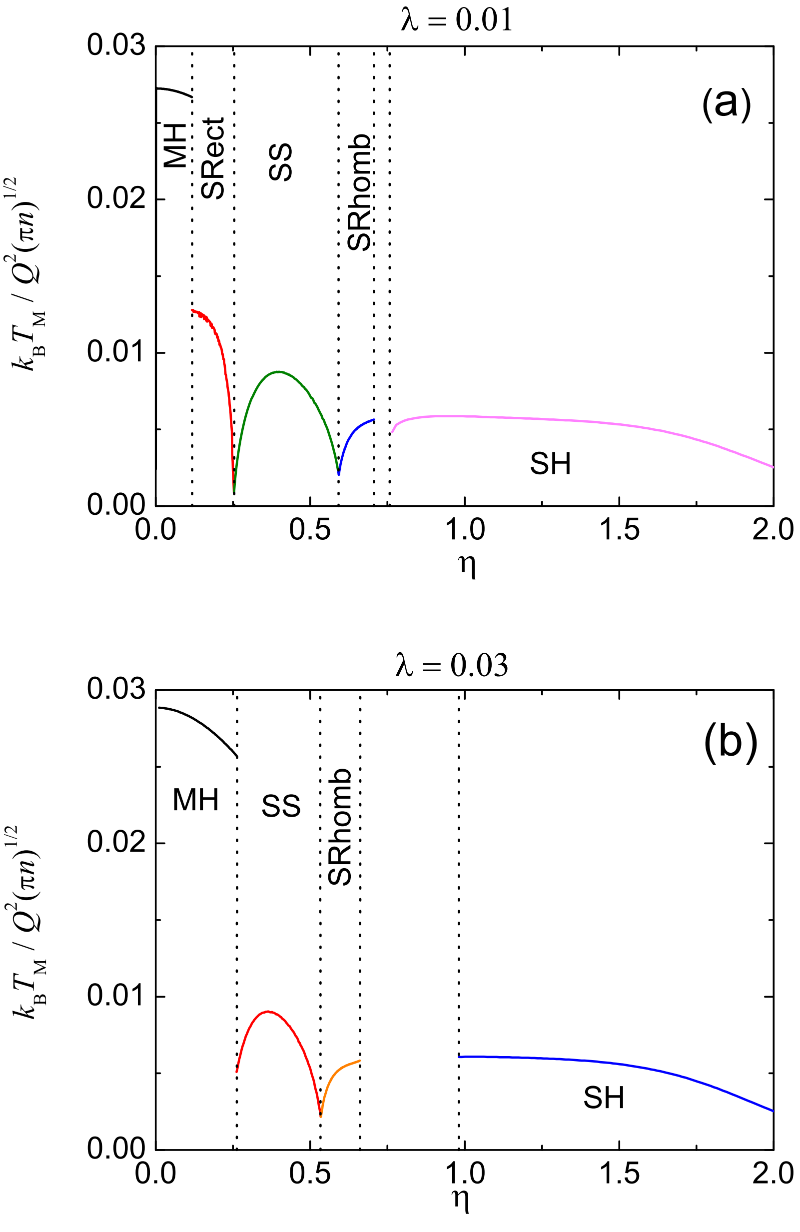

Figure 3.1: Melting temperature of the energetically favorable phases as a function of η, for (a) $\lambda = 0.01$ and (b) $\lambda = 0.03$. The vertical dotted lines indicate the phase boundaries.

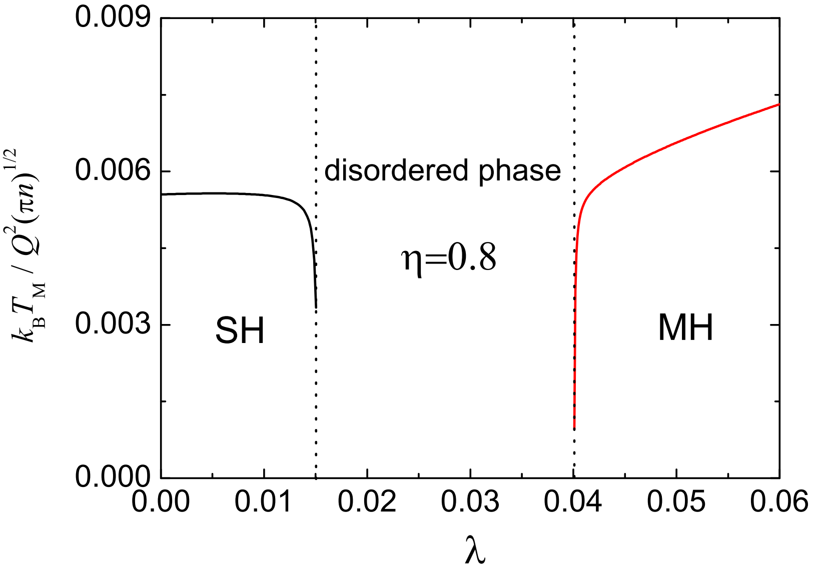

Figure 3.2: Melting temperature of the SH and MH phases for $\eta = 0.8$ as a function of λ. The vertical dotted lines indicate the phase boundaries.

for $\lambda \gtrsim 0.0169$, while the MH phase is unstable for $\lambda \lesssim 0.0401$. Therefore, for the SH phase we only present the melting temperature in the range $0 \leq \lambda \lesssim 0.0169$. We notice that the melting temperature of the SH phase decreases rapidly when λ is around the stability limit, 0.0169. We recall that when the value of λ is increased, the magnetic character of the particles becomes more relevant. As a consequence, the dipoles in both layers tend to be aligned in a hexagonal lattice (MH phase) and the SH phase is no longer stable. On the other hand, the MH phase is energetically favorable for $\lambda \gtrsim 0.043$, but it is stable even before this value, i. e., $\lambda \approx 0.0401$. Furthermore, when λ is increased the frequencies of vibration of the MH phase become large, and consequently, the melting temperature increases with λ, as can be clearly seen in the Fig. 3.2.

Fig. 3.3 shows the melting temperature of the MH phase for three values of λ, as a function of η. As observed previously, here we also have that the melting temperature of the MH phase becomes larger when λ is increased. However, the most important result here is the re-entrant behavior of T_M as a function of η when the value of λ is very large, e. g., $\lambda = 3$. Actually, this re-entrant behavior is already observed when $\lambda \cong 1.1$. It means that, at a fixed temperature, the MH phase melts going to the liquid phase and thereafter it returns to the solid phase, when the distance between the layers η (for a fixed density) is increased. This re-entrant behavior was also observed in the bilayer system with only dipole-dipole interaction, and it was explained as being due to the attractive part of the dipole-dipole interaction [5]. Therefore, in the bilayer system with only charge-charge interaction this re-entrant behavior can not be found, since only repulsive interaction is present. Moreover, in the present bilayer system of charged magnetic dipoles, this nonmonotonic behavior of T_M depends on λ, i.e, depends on the magnetic dipole moment and

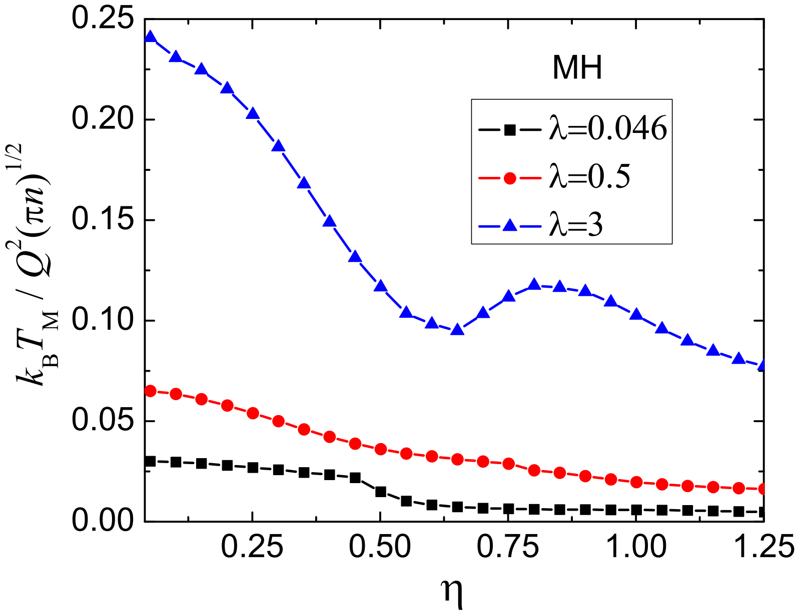

Figure 3.3: Melting temperature of the MH phase as a function of η.

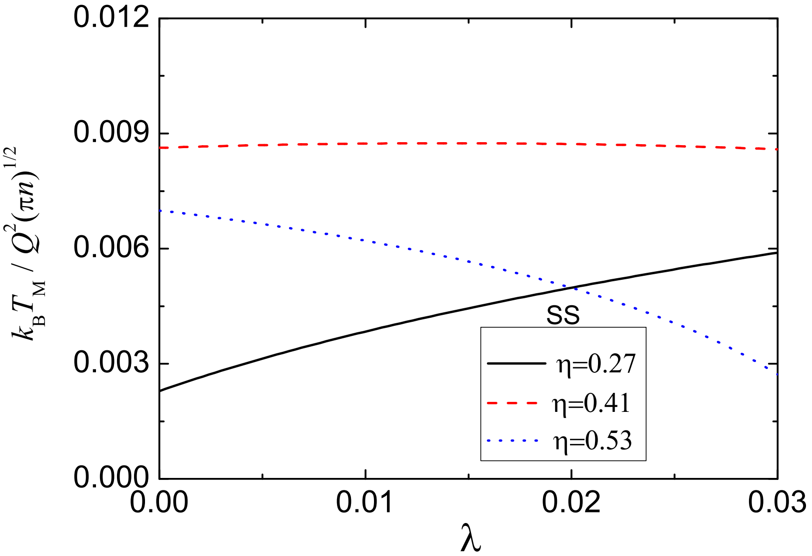

Figure 3.4: Melting temperature of the SS phase for three values of η as a function of λ.

the charge of the particles (for a fixed density). As commented in Ref. [56], the charges and the magnetic dipole moment of the colloidal particles can be altered by changing the pH of the medium in which the colloidal particles are inserted, and through an external magnetic field, respectively. As a consequence, this re-entrant behavior can, in principle, be controlled by the pH of the solution and/or by an external magnetic field.

Fig. 3.4 presents the melting behavior for the SS phase for three values of η and its dependence with λ. First of all, we find quite different situations for each value of η. For $\eta = 0.41$, T_M is almost constant when λ is changed in the interval $0 \leq \lambda \leq 0.03$. Recalling that the melting temperature can be understood in terms of the phonon spectrum of the system, the constancy of T_M for $\eta = 0.41$ should be associated with the invariance of the phonon spectrum when λ is changed. Actually, it was shown in Ref. [56] that the phonon spectra of the SS phase for $\eta = 0.41$ with $\lambda = 0.002$ and $\lambda = 0.029$ are pratically the same. Besides, although the phonon spectrum for $\eta = 0.27$ and $\eta = 0.53$ for the same values of λ presents the same qualitative behavior, we still notice a little increase of the frequencies of vibration when $\eta = 0.27$ and $\lambda = 0.029$ and a little decrease when $\eta = 0.53$ and $\lambda = 0.029$ by comparison with the frequencies for $\lambda = 0.002$. Therefore, our results for the melting temperature of the SS phase are in complete agreement with the phonon spectrum discussed in Ref. [56], since the curves of T_M for $\eta = 0.27$ and $\eta = 0.53$ show a increase and a decrease of T_M with λ, respectively.

3.4 Conclusions

We investigated the melting behavior of a 2D classical bilayer system of charged magnetic dipoles. Because the Lindemann criterion for melting (Eq. (1)) is unseemly for 2D systems we resort to the modified Lindemann criterion (Eq. (3)) in order to estimate the melting temperature of the system. Besides, the correlation function (Eq. (2)) was obtained within the harmonic approximation. We studied the melting as a function of the distance between the layers η (for a fixed density) and the dimensionless parameter λ which stands for relative intensity of the dipole-dipole interaction with respect to the charge-charge interaction. Due to the large number of possible combinations of η and λ, we analyze only some situations which provide us the general understanding of the system at nonzero temperature. We observed that the maximum melting temperature of the structural phases gets smaller when the distance between the layers increases, for a fixed λ. Moreover, due to strong coupling between the dipoles, the MH phase has the highest melting temperature. Another observation is the decrease (increase) of the melting temperature of the SH phase (MH phase), when the magnetic character of the particles becomes large, i. e., when λ increases. Therefore, it is possible to alternate between staggered and matched arrangements by changing the parameter λ as, for example, through an external magnetic field or the pH of the medium. Nevertheless, our most important result is the re-entrant melting behavior of the MH phase when $\lambda \gtrsim 1.1$. It means that, at a fixed temperature, a sequence of solid-liquid transitions takes place when the distance between the planes η is increased, for $\lambda \gtrsim 1.1$.

Up to now, we studied the structures, dynamical properties and melting of a bilayer system of charged magnetic dipoles. In the next chapter, we will investigate the stability, dynamical properties and melting of a binary system of interacting dipoles in a monolayer structure, within the harmonic approximation and using the modified Lindemann criterion.

Chapter 4

Dynamical properties and melting of binary two-dimensional colloidal alloys

4.1 Introduction

Colloids are useful model systems for studying not only important physical phenomena such as crystallization and melting [14, 63], but also for solids specially because of the orders of magnitude slower temporal and larger spatial scales allowing the use of video-microscopy techniques[4, 64] and, therefore, properties such as structure, phonons and melting can be studied in real time [55]. There are several possibilities (at interfaces, in between glass plates, patterned substrates) to stabilize the colloidal particles into a reduced dimensional system such as channels and planar substrates. Additionally, the interaction between the colloidal particles and thus the physical properties of the system can be externally controlled, e. g. by means of external magnetic [65] and/or electric fields [66].

Colloidal systems composed of two different types of dipolar particles confined in a monolayer structure have attracted the attention of many theoretical and experimental researchers. Stirner *et al.*, [67] performed molecular dynamics simulations at finite temperatures of a binary colloidal monolayer of two different particle sizes at an oil-water interface whose inter-particle interaction is governed by an effective dipole potential. The simulations showed that for certain ratios of small (B) to large (A) particles, e. g., $2:1$ (AB_2) and $6:1$ (AB_6), the system forms a 2D crystal. In both cases the crystal is composed of a hexagonal lattice of large particles with a unit cell composed of one A particle and two B particles for AB_2, and one A particle and six B particles for AB_6. Studies of the zero temperature ($T = 0$) phase diagram of a 2D binary system of dipoles using lattice sum calculations, [68] and genetic algorithms [69, 70] predicted the formation of several possible lattice structures as a function of the composition and the susceptibility ratio.

The structural behavior of binary mixtures of super-paramagnetic colloidal particles at an air-water interface was investigated using integral equation theory together with computer simulations

[71, 72] and experiments [72, 73]. Those studies, however, found only a partial clustering of small particles [71, 72] and a local crystalline order [73].

More recently, an interesting experimental and theoretical study [5] of a 2D binary colloidal system of large (A) and small (B) silica particles at an octane-water interface was presented as a function of the relative concentration of small particles $\xi = \rho_B/(\rho_A + \rho_B)$, where ρ_A, ρ_B are the 2D densities of A and B particles, respectively. Due to the experimental setup, the particles were supposed to interact through a repulsive dipole-dipole potential and it was found that the system self-assemblies in a *hexagonal alloy phase* (HAP). Also, it was shown that while the HAP for $\xi = 2/3$ (AB_2) and $\xi = 6/7$ (AB_6) are thermodynamically stable, the HAP for $\xi = 3/4$ (AB_3) and $\xi = 5/6$ (AB_5) was unstable. A comparison between the radial distribution function of the small B particles around the A particles $g_{AB}(r)$ obtained from the analytical *minimum energy configuration* (MEC) with the one obtained from $T \neq 0$ Monte Carlo simulations, that were based on a finite size computational unit cell, was further used in order to determine if the configuration was stable or not. The structure and melting behavior of the system was also studied theoretically as a function of the composition and the dipole moment ratio, using a lattice sum method and Monte Carlo simulations [24]. By investigating the radial distribution function for small particles $g_{BB}(r)$ as a function of temperature, it was found that the melting temperature of the AB_2 and AB_6 configurations was three orders of magnitude larger than that of the AB_5 structure [24].

In this work, we address the dynamical properties and melting of a 2D binary colloidal system of dipoles which consists of particles with small and large dipole moments μ_B and μ_A, respectively. Within the *harmonic approximation* we calculate the phonon spectrum of the system for different values of the dipole moment ratio $s_B = \mu_B/\mu_A$, the relative concentration of small particles ξ, and mass ratio $m^* = m_B/m_A$. The motivation to do so is twofold: 1) it is possible to tune the number and width of the phonon gaps, and the shape of the phonon bands [16]; 2) the study of the phonon spectra tells us additionally if the colloidal alloys are stable, i.e., have real phonon frequencies. Specifically, through a systematic analysis of the dispersion relation we determine the interval of values of s_B for which the considered colloidal alloys are stable. Furthermore, the study of the dispersion relation allows us to obtain the sound velocity, and the optical frequencies in the long-wavelength limit. We also present an estimation of the melting temperature of the sub-lattice generated by the big particles (type A) as a function of s_B, ξ and m^* using the modified Lindemann criterion. As a consequence, we found that it is possible to specify the optimum value of s_B for which the melting temperature of the system for a given composition is maximum.

In most part of this work, we will concentrate on the perfectly ordered 2D *hexagonal* colloidal alloys in order to model some of the configurations observed experimentally in Ref. [5], namely, the configurations for $\xi = 2/3$ (AB_2), $\xi = 3/4$ (AB_3), $\xi = 5/6$ (AB_5), and $\xi = 6/7$ (AB_6). Additionally, we also studied a 2D *square* alloy for $\xi = 1/2$ ($S(AB)$). The lattice structures for these colloidal alloys are illustrated in Fig. 4.1. It is worth to emphasize that in our calculations we considered crystal structures, i. e. perfect periodic arrangements where defects and boundary effects are absent, in contrast with real experiments where, in general, defects and finite size effects might be present. Thus, although a small number of defects can be considered negligible from an experimental point of view (they may act as a stabilizing factor), they are determinant for the stability of the considered lattice from a theoretical point of view. E.g., we find that our perfect hexagonal alloy phase for $\xi = 2/3$ (AB_2) is not always stable even for the same set of parameters considered in the experiments [5], which indicates that some distortion with respect to the perfect HAP might be present in order to stabilize the experimentally observed configuration. Indeed, deviations from the perfect HAP were previously pointed out by one of us [24] and by Julia Fornleitner *et al.* [70].

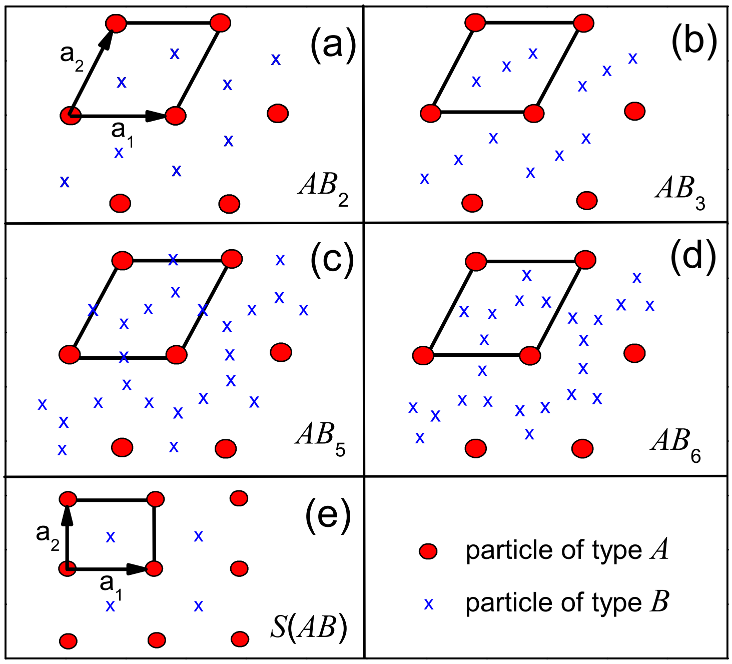

Figure 4.1: Structures of the colloidal alloys (a) AB_2 (b) AB_3 (c) AB_5 (d) AB_6 and (e) $S(AB)$. The unit cell of each phase is shown by the solid box and the primitive vectors are explicitly shown.

This chapter is organized as follows. In Sec. 4.2, we introduce the model, define the parameters used to characterize the system, and present the colloidal alloys considered in this work. In Sec. 4.3, we present the calculation of the dispersion relation and discuss the numerical results. In Sec. 4.4, we study the melting behavior of the system. Our conclusions are given in Sec. 4.5.

4.2 Model

We study a 2D binary colloidal system of dipole particles. The particles denoted by A and B have dipole moments μ_A and μ_B, respectively, directed perpendicularly to the plane. The interaction potential is of the dipole-dipole form and can be written in two different ways:

$$U_{kj}(r) = \frac{\mu_k \mu_j}{r^3} \tag{4.1}$$

or

$$\beta U_{kj}(r) = \Gamma \frac{s_k s_j a^3}{r^3} \tag{4.2}$$

where $k, j = A, B$, and

$$\Gamma = \frac{\mu_A^2}{k_B T a^3} \quad , \tag{4.3}$$

is the dimensionless interaction strenght, which relates the potential and the thermal energy, r is the distance between two particles, k_B the Boltzmann constant, T the temperature of the system, a the lattice parameter of the A particles, $\beta = 1/k_B T$, and $s_B = \mu_B/\mu_A$ is the dipole moment ratio.

For the experimental system studied in Ref. [5], A and B stand for the large and small synthetic amorphous silica particles with diameters 3.00±0.05 μm and 1.00±0.05 μm, respectively, located at an octane-water interface. In this case, the dipoles are mainly due to the residual charges at the particle-oil interface (see Fig. 4.2), and the considered dipole moment ratio was $s_B = 0.037$. In this experiment, the large particles were spread first, forming a hexagonally ordered monolayer structure. Then, the small particles were spread over the existing monolayer. The relative concentration of small particles ξ in the mixed monolayer was varied, but keeping the number density of the large particles constant [5].

On the other hand, for the experimental setup considered in Refs. [72] and [73], A and B represent the large and small super-paramagnetic colloidal particles, respectively, at a water-air interface. For instance, from Ref. [72], the big particles have diameter 4.7 μm, mass density $d_A = 1.3 g/cm^3$ and magnetic susceptibility $\chi_A = 6.2 \times 10^{-11}\mathrm{A}m^2/\mathrm{T}$, while the small ones having diameter 2.8 μm, mass density $d_B = 1.5 g/cm^3$ and magnetic susceptibility $\chi_B = 6.6 \times 10^{-12}\mathrm{A}m^2/\mathrm{T}$. An external magnetic field $\vec{B}$ applied perpendicularly to the water-air interface, induces in each particle a magnetic moment $\vec{\mu}_i = \chi_i \vec{B}$, where $i = A, B$. Thus, the dipole moment ratio is $s_B \approx 0.1$.

In order to understand the experimental setup composed of super-paramagnetic coloidal particles, we will use the idea of ferromagnetic solids. The main characteristic of ferromagnetic solids is that they are non-linear, i. e., they have magnetization even in the absence of an external magnetic field. Furthermore, inside these solids there are regions where magnetic dipoles of the individual atoms are oriented in a fixed direction. These regions are called *magnetic domains* (see Fig. 4.3) [25, 26]. Examples of ferromagnetic materials are iron, nickel, cobalt and some of its alloys and compounds [25, 26]. The magnetic dipole is responsable for the magnetic characteristics of the material and has its origin associated to the orbital angular momentum and spin of the electrons.

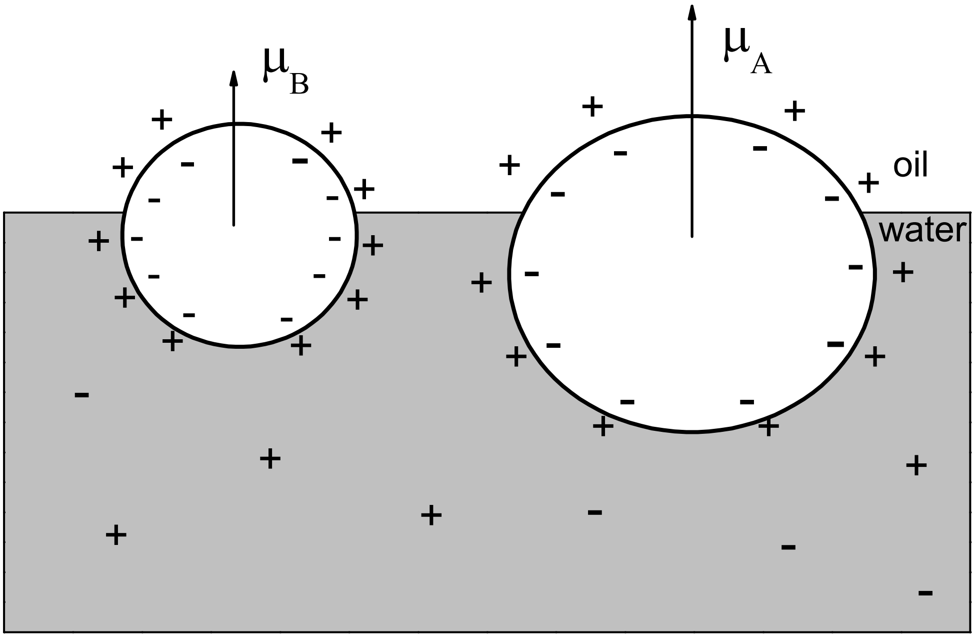

Figure 4.2: Two silica particles of different size floating at an oil-water interface. The charges at the particle-oil interface generate a resultant dipole moment in each particle.

When the size of a ferromagnetic material is reduced, a mono-domain particle can be generated depending on the size of the material. This size for which a mono-domain particle is generated is called critical size (critical diameter for a spherical particle) and depends on the material. As shown in Fig. 4.4, when the diameter is smaller than the critical diameter, we have a mono-domain particle. Otherwise, we have a multi-domain particle [27, 28].

In 1946, Kittel [27] presented the first estimative of the value of the critical diameter (D_c) from which a mono-domain is produced. The value of D_c is about $15nm$ [27, 29]. The magnetic particles with diameter (D) smaller than D_c show a super-paramagnetic behavior due to the fact that the value of the total magnetic moment is in the interval between the paramagnetic and ferromagnetic values [29]. Therefore, the saturation magnetization of the super-paramagnetic materials is larger than that of the paramagnetic materials. Other characteristics of the super-paramagnetic materials are the absence of hysteresis in the magnetization curve and zero coercive field [29]. In the magnetization curve of a material, the coercive field is the magnetic field necessary to remove the residual magnetization.

We are now able to understand how the binary system of super-paramagnetic colloidal particles can be studied. When an external magnetic field is applied in a fixed direction, for instance, perpendicularly to the water-air interface as shown in Fig. 4.5, the particle with larger diameter will also have a larger resultant magnetic dipole in the same direction of the field.

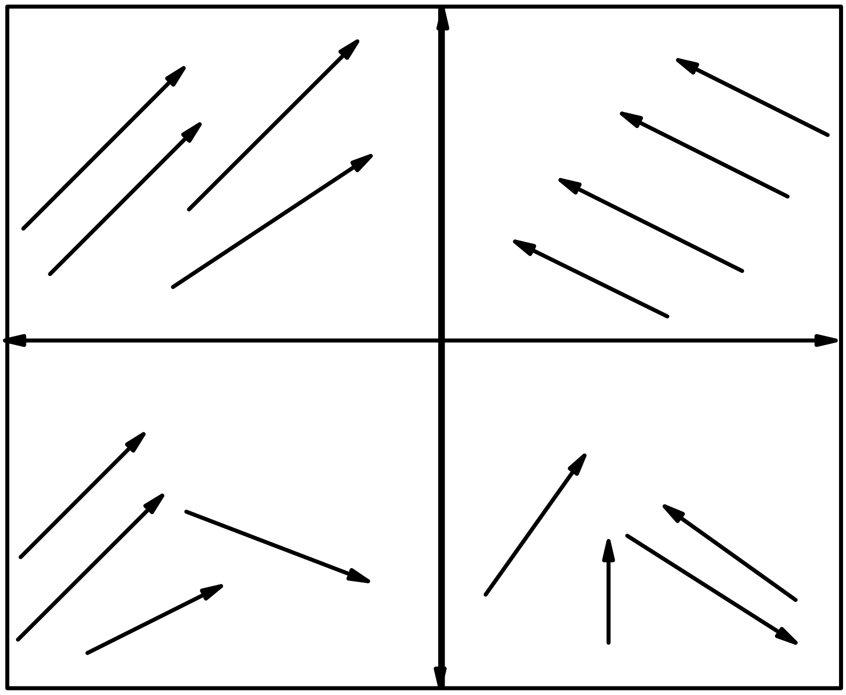

Figure 4.3: A material with four magnetic domains where the vectors indicate the magnetic dipoles.

The colloidal alloy phases depend on the dipole moment ratio as well as the relative concentration of small particles

$$\xi = \frac{\rho_B}{\rho_A + \rho_B} \quad , \tag{4.4}$$

where ρ_A and ρ_B are the 2D densities of A and B particles, respectively.

In the present work we will study the phonons and melting of: 1) the 2D *hexagonal* colloidal alloys considered in Ref. [5] for $\xi = 2/3$ (AB_2), $\xi = 3/4$ (AB_3), $\xi = 5/6$ (AB_5), and $\xi = 6/7$ (AB_6); and 2) a 2D *square* alloy for $\xi = 1/2$ ($S(AB)$) (see Figure 4.1).

The system at hand is 2D with unit cell having one A particle and n small B particles. Therefore, the equilibrium positions of the A particles and of n B particles are given by $\vec{R}_A = \vec{R}$, and $\vec{R}_{B_i} = \vec{R} + \vec{c}_i$, where $\vec{R} = l_1\vec{a}_1 + l_2\vec{a}_2$ with l_1, l_2 integers, $\vec{a}_1$, $\vec{a}_2$ are the primitive vectors, $\vec{c}_i = \alpha_i\vec{a}_1 + \beta_i\vec{a}_2$, where $\alpha_i, \beta_i \in (0,1)$ are determined by minimizing the energy for a given dipole moment ratio, and $i = 1, ..., n$. The primitive vectors of the hexagonal lattice are $\vec{a}_1 = a(1,0)$ and

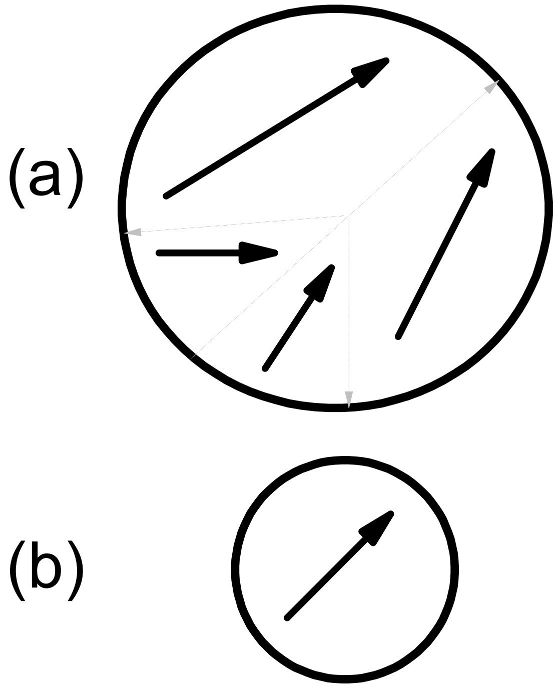

Figure 4.4: Example of a spherical multi-domain particle for (a) $D > D_c$ and of a mono-domain particle for (b) $D < D_c$, where D is the diameter of the particle and D_c is the critical diameter.

$\vec{a}_2 = a(1/2, \sqrt{3}/2)$, while for the square lattice, $\vec{a}_1 = a(1, 0)$ and $\vec{a}_2 = a(0, 1)$. Since the colloidal alloys considered here have only one A particle per unit cell, the density of A particles ρ_A is given by $\rho_A a^2 = 2/\sqrt{3}$ and $\rho_A a^2 = 1$ for hexagonal and square unit cells, respectively.

4.3 Dynamical properties

The dynamical properties, i. e., the phonon spectrum, will be calculated within the harmonic approximation. In this approach, one considers that each particle executes small oscillations (compared to the average distance between the particles) around its equilibrium position and, therefore, one expands the potential energy up to the second order in the deviations from its equilibrium position. Due to the periodicity of the system, one introduces Bloch plane wave-like solutions and thus, one obtains (for a given wave-vector $\vec{q}$ along the high-symmetry directions of the first Brillouin zone) the dynamical matrix whose eigenvalues and eigenvectors are the square frequencies of vibration, $\omega^2(\vec{q}, j)$, and the direction of vibration, $\vec{e}(\vec{q}, j)$, respectively, with $j = 1, ..., 2n_p$, where n_p is the total number of particles per unit cell.

The study of the dispersion relation gives us additionally the stability of the mentioned colloidal

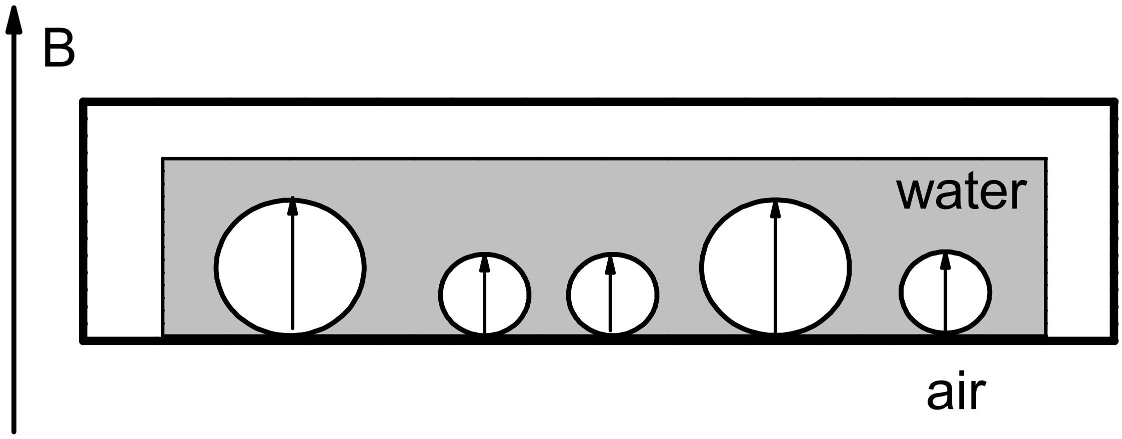

Figure 4.5: Super-paramagnetic colloidal particles at a water-air interface. An external magnetic field applied perpendicularly to the interface induces a magnetic dipole in each particle leading to a repulsive dipole-dipole interaction.

alloys, for a given dipole moment ratio s_B. The considered crystal structure of the colloidal alloy is stable only if $\omega^2(\vec{q}, j) \geq 0$ for all $\vec{q}$ and j [34, 36, 37, 44]. For $\omega^2(\vec{q}, j) < 0$ the frequencies are imaginary, i. e., the amplitude of particle oscillation becomes an exponentially increasing function of time [44]. It implies that the corresponding crystal structure of the colloidal alloy is unstable and will not exist.

All the colloidal alloys considered in this work have more than one particle per unit cell. As a consequence, there are several acoustical and optical modes which can be associated to in-phase and out-of-phase vibrations of particles in the unit cell, respectively. The acoustical branch is characterized by $\omega(\vec{q}) \to 0$ for $\vec{q} \to 0$, while for the optical branch $\omega(\vec{q}) \to$ *constant* in the limit $\vec{q} \to 0$. Besides, the acoustical and optical branches have a longitudinal, $\vec{e} \parallel \vec{q}$, and a transverse mode [44], $\vec{e} \perp \vec{q}$.

The dynamical matrix is given by [36, 44, 62]

$$C_{\alpha\beta}(kk' \mid \vec{q}) = \frac{1}{\sqrt{m_k m_{k'}}} \sum_{l'} \phi_{\alpha\beta}(lk, l'k')\ e^{-i\vec{q}.(\vec{R}_{lk} - \vec{R}_{l'k'})} \tag{4.5}$$

where $\phi(r)$ is the interaction potential and

$$\phi_{\alpha\beta}(lk,l'k') = \partial_\alpha \partial_\beta \phi(\vec{R}_{lk} - \vec{R}_{l'k'}) \tag{4.6}$$

are the force constants with α,β=x,y. Furthermore, $\vec{R}_{lk} = \vec{R}(l) + \vec{R}(k)$ is the equilibrium position vector of the kth particle in the lth unit cell of the crystal, m_k is its mass and $\vec{R}(l) = \vec{R}$. Besides, the force constants have the property

$$\sum_{lk,l'k'} \phi_{\alpha\beta}(lk,l'k') = 0 \tag{4.7}$$

which will be useful in our further calculations. Thus, the equilibrium positions of A particles and of n B particles are given by $\vec{R}_{lA} = \vec{R}_A$ and $\vec{R}_{lB_i} = \vec{R}_{B_i}$. Furthermore, the order of the dynamical matrix is $t = 2n_p \times 2n_p$, i. e., it depends on the considered 2D lattice. The dynamical matrix can be written as

$$D = \begin{pmatrix} D^{AA} & D^{AB_1} & ... & D^{AB_n} \\ D^{B_1A} & D^{B_1B_1} & ... & D^{B_1B_n} \\ . & . & ... & . \\ . & . & ... & . \\ . & . & ... & . \\ D^{B_nA} & D^{B_nB_1} & ... & D^{B_nB_n} \end{pmatrix} , \tag{4.8}$$

where D^{AA}, D^{AB_1}, ..., $D^{B_nB_n}$ are 2×2 block matrices. From Eqs. (5) and (7), the elements of the block D^{AA} are written by

$$D^{AA}_{\alpha\beta}(\vec{q}) = \frac{1}{m_A}\left[S^{AA}_{\alpha\beta}(0) + \sum_i SI1^{AB_i}_{\alpha\beta}(0) - S^{AA}_{\alpha\beta}(\vec{q}) \right] \tag{4.9}$$

where

$$S^{AA}_{\alpha\beta}(\vec{q}) = -\mu_A^2 \lim_{r\to 0} \partial_\alpha \partial_\beta \psi_0(\vec{r},\vec{q}) \quad , \tag{4.10a}$$

$$SI1^{AB_i}_{\alpha\beta}(\vec{q}) = -s_B \mu_A^2 \lim_{r\to 0} \partial_\alpha \partial_\beta \psi^i_{I1}(\vec{r},\vec{q}) \quad , \tag{4.10b}$$

with

$$\psi_0(\vec{r},\vec{q}) \;\; = \;\; \sum_{\vec{R}\neq\vec{0}} \frac{e^{-i\vec{q}.\vec{R}}}{|\vec{r}+\vec{R}|^3} \quad , \tag{4.11a}$$

$$\psi^{i}_{I1}(\vec{r},\vec{q}) \;=\; \sum_{\vec{R}} \frac{e^{-i\vec{q}.(\vec{R}+\vec{c}_i)}}{|\vec{r}+\vec{R}+\vec{c}_i|^3} \quad . \tag{4.11b}$$

On the other hand, from Eq. (5) we found

$$D^{AB_i}_{\alpha\beta}(\vec{q}) = \frac{1}{\sqrt{m_A m_B}}\left[-SI1^{AB_i}_{\alpha\beta}(\vec{q})\right] \quad . \tag{4.12}$$

In the same spirit of Refs. [34, 36, 37] we used the Ewald summation technique and transformed Eqs. (11a) and (11b) into expressions which converge rapidly. Thus, we obtain [37]

$$\begin{aligned}\psi_0(\vec{r},\vec{q}) \;=\;& \pi\rho_A \sum_{\vec{G}} e^{i(\vec{q}+\vec{G}).\vec{r}}\Upsilon\left(\frac{|\vec{q}+\vec{G}|}{2\varepsilon},0\right) + \frac{2\varepsilon e^{-\varepsilon^2 r^2}}{\sqrt{\pi}r^2} \\ & -\frac{erf(\varepsilon r)}{r^3} + \sum_{\vec{R}\neq\vec{0}} e^{-i\vec{q}.\vec{R}}\Omega_1(|\vec{r}+\vec{R}|) \quad ,\end{aligned} \tag{4.13}$$

with

$$\begin{aligned}\Upsilon\left(\frac{|\vec{q}+\vec{G}|}{2\varepsilon},0\right) \;=\;& \frac{4\varepsilon}{\sqrt{\pi}}e^{-|\vec{q}+\vec{G}|^2/4\varepsilon^2} \\ & -2|\vec{q}+\vec{G}|erfc\left(\frac{|\vec{q}+\vec{G}|}{2\varepsilon}\right)\end{aligned} \tag{4.14a}$$

and

$$\Omega_1(x) \;=\; \frac{erfc(\varepsilon x)}{x^3} + \frac{2\varepsilon}{\sqrt{\pi}}\frac{e^{-\varepsilon^2 x^2}}{x^2} \tag{4.14b}$$

where the parameter $\varepsilon > 0$ is related to the density of large particles, i. e., $\varepsilon = \sqrt{\pi\rho_A}$. Besides, we have

$$\begin{aligned}\psi^{i}_{I1}(\vec{r},\vec{q}) \;=\;& \pi\rho_A \sum_{\vec{G}} e^{i(\vec{q}+\vec{G}).\vec{r}} e^{i\vec{G}.\vec{c}_i}\Upsilon\left(\frac{|\vec{q}+\vec{G}|}{2\varepsilon},0\right) + \\ & + \sum_{\vec{R}} e^{-i\vec{q}.(\vec{R}+\vec{c}_i)}\Omega_1(|\vec{r}+\vec{R}+\vec{c}_i|)\end{aligned} \tag{4.15}$$

and, therefore, the block matrices D^{AA} and D^{AB_i} involve only rapidly convergent sums. On the other hand, the block $D^{B_iB_j}$, $i \neq j$, and $D^{B_iB_i}$, are written as

$$D^{B_iB_j}_{\alpha\beta}(\vec{q}) = \frac{1}{m_B}\left[-SII1^{B_iB_j}_{\alpha\beta}(\vec{q})\right] \tag{4.16a}$$

$$
\begin{aligned}
D_{\alpha\beta}^{B_iB_i}(\vec{q}) &= \frac{1}{m_B}\Bigg[s_B^2 S_{\alpha\beta}^{AA}(0) + \sum_{j\neq i} SII1_{\alpha\beta}^{B_iB_j}(0) \\
&\quad + SI1_{\alpha\beta}^{AB_i}(0) - s_B^2 S_{\alpha\beta}^{AA}(\vec{q})\Bigg] \qquad (4.16b)
\end{aligned}
$$

with

$$SII1_{\alpha\beta}^{B_iB_j}(\vec{q}) = -s_B^2\mu_A^2 \lim_{r\to 0}\partial_\alpha\partial_\beta\psi_{II1}^{ij}(\vec{r},\vec{q}) \qquad (4.17a)$$

$$\psi_{II1}^{ij}(\vec{r},\vec{q}) = \sum_{\vec{R}} \frac{e^{-i\vec{q}.(\vec{R}+\vec{c}_{ij})}}{|\vec{r}+\vec{R}+\vec{c}_{ij}|^3} \qquad (4.17b)$$

$$\vec{c}_{ij} = \vec{c}_i - \vec{c}_j \quad . \qquad (4.17c)$$

Again, the expression for $\psi_{II1}^{ij}(\vec{r},\vec{q})$ using the Ewald method is given by

$$
\begin{aligned}
\psi_{II1}^{ij}(\vec{r},\vec{q}) &= \pi\rho_A \sum_{\vec{G}} e^{i(\vec{q}+\vec{G}).\vec{r}} e^{i\vec{G}.\vec{c}_{ij}} \Upsilon\left(\frac{|\vec{q}+\vec{G}|}{2\varepsilon}, 0\right) + \\
&\quad + \sum_{\vec{R}} e^{-i\vec{q}.(\vec{R}+\vec{c}_{ij})}\Omega_1(|\vec{r}+\vec{R}+\vec{c}_{ij}|) \quad . \qquad (4.18)
\end{aligned}
$$

Since the dynamical matrix is hermitian, we have $D^{B_iA} = [D^{AB_i}]^\dagger$ and $D^{B_jB_i} = [D^{B_iB_j}]^\dagger$. Because the dynamical matrix involves the mass of the particles, we introduced the parameter $m^* = m_B/m_A$. For Brownian systems one can consider $m^* = 1$, i. e. the particles have the same mass, since the inertial asymmetry between the colloids becomes irrelevant in the overdampped regime [16, 74, 2]. On the other hand, assuming that the dipole moment of each particle is $\mu_i = \lambda D_i^3$, where λ is a constant of proportionality and D_i is the radius of the particle [69], and that the particles have the same mass density, we obtain $m^* = s_B = \mu_B/\mu_A$. The case with different masses is available experimentally in systems of colloids between glass plates with no solvent [75]. In what follows, we will restrict ourselves to the two cases $m^* = s_B$ and $m^* = 1$.

Figs. 4.6 and 4.7 show the square of the phonon frequencies in units of $\omega_0^2 = \mu_A^2\rho_A^{5/2}/m_A$ of the structure AB_2 (Fig. 4.1a) for $s_B = 0.015$ and $s_B = 0.037$, considering $m^* = s_B$ and $m^* = 1$, respectively. The square frequencies are shown along the high-symmetry directions in reciprocal space, where the high-symmetry points are shown as insets. For $s_B = 0.015$, we found $\omega^2(\vec{q}, j) \geq 0$ for all the eigenvalues, indicating a stable long-range AB_2 ordered structure. On the other hand, for the dipole moment ratio $s_B = 0.037$ considered in the experiments performed by Law *et al.* [5], we found $\omega^2(\vec{q}, j) < 0$ for some eigenvalues indicating that the AB_2 structure is not stable for $s_B = 0.037$. Actually, we found that on the basis of the requirement of real phonon frequencies, the range of stability for the phase AB_2 is $0 \leq s_B \leq 0.0269$. We stress that in our calculations the considered perfect periodic structures are free of defects and boundary effects, in contrast with real experiments where, in general, defects might be present. Thus, although a small number of

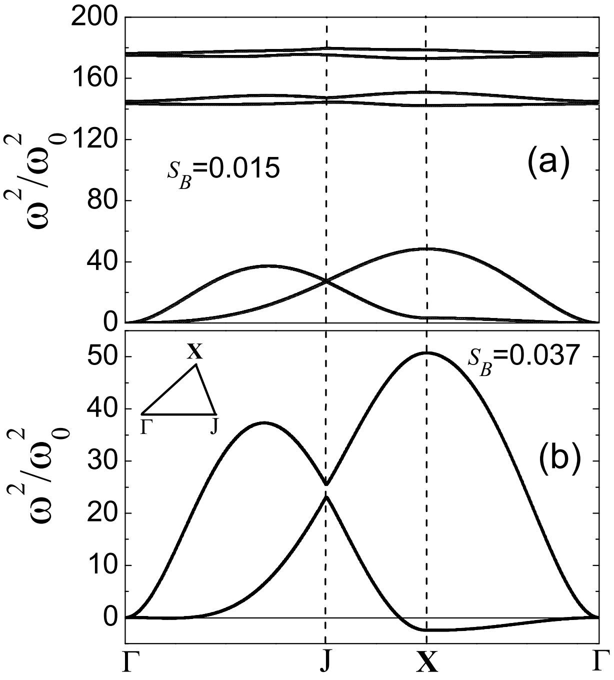

Figure 4.6: Square of the phonon frequencies of the crystal phase AB_2 for $m^* = s_B$ in units of $\omega_0^2 = \mu_A^2 \rho_A^{5/2}/m_A$ (a) for $s_B = 0.015$ and (b) $s_B = 0.037$, along the high-symmetry directions in reciprocal space. The high-symmetry points Γ, J and X are shown in the inset of (b). Only the lowest energy modes are shown in (b) in order to enlarge the region around zero frequency.

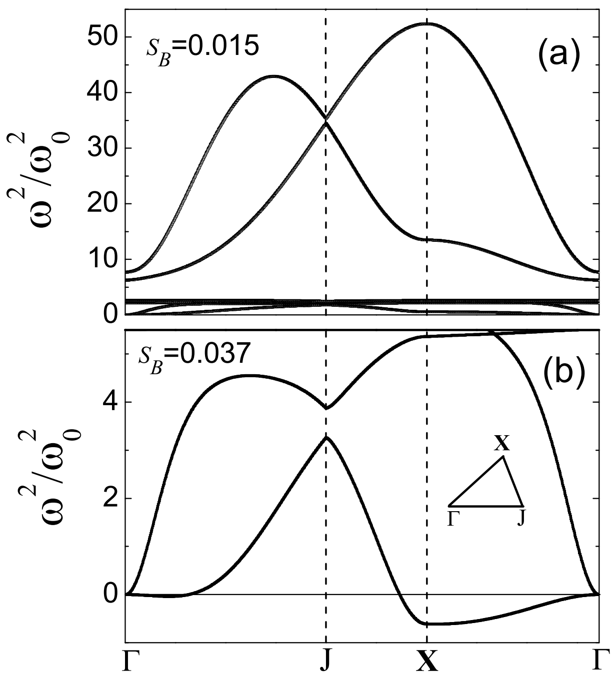

Figure 4.7: Square of the phonon frequencies of the phase AB_2 for $m^* = 1$ (a) for $s_B = 0.015$ and (b) $s_B = 0.037$. Only the lowest energy modes are shown in (b).

defects in the configuration AB_2 for $s_B = 0.037$ can be considered negligible from an experimental point of view, they are determinant for the stability from a theoretical point of view. Our results

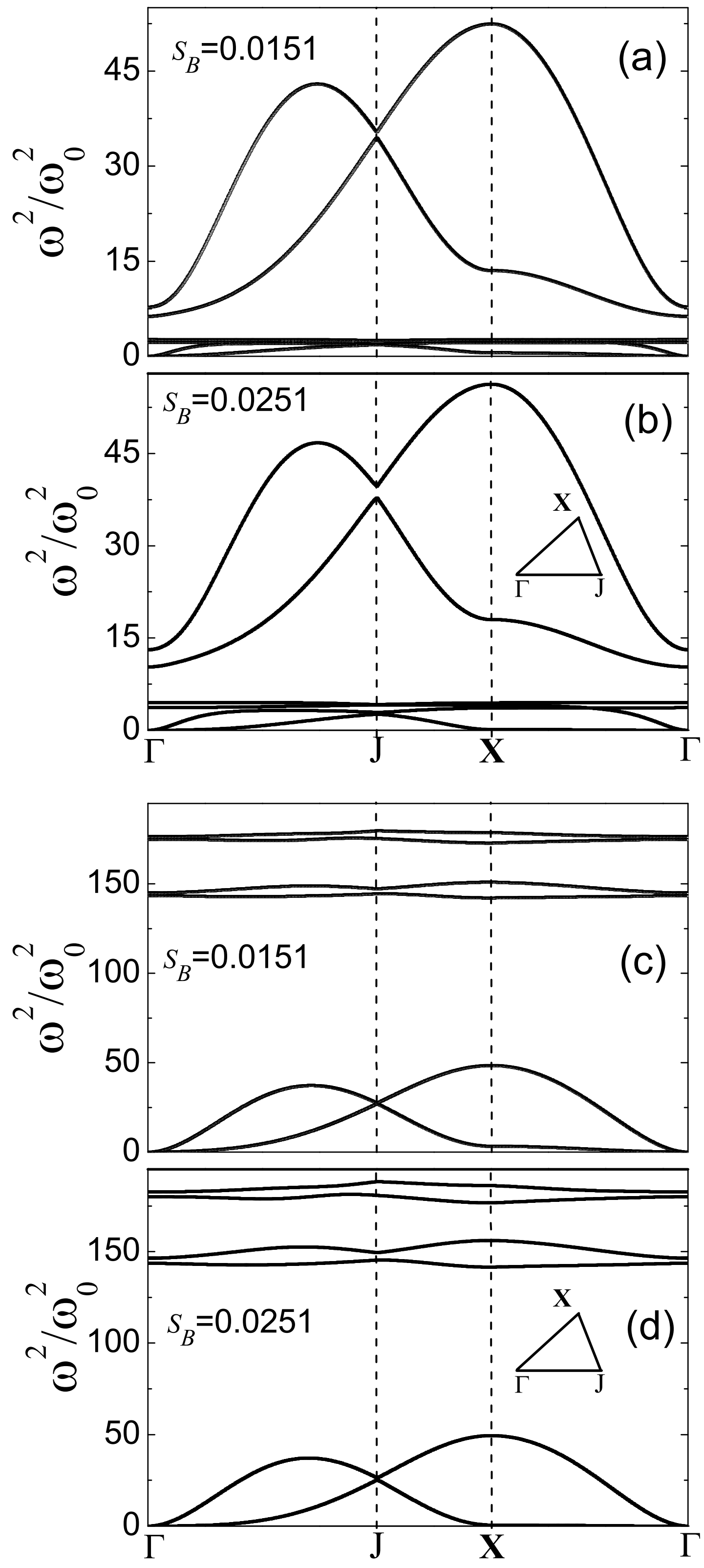

Figure 4.8: Square of the phonon frequencies of the phase AB_2 considering $m^* = 1$ ((a) and (b)) and $m^* = s_B$ ((c) e (d)).

indicate that the stable phase observed experimentally in Ref. [5] must present some distortion from the perfect hexagonal alloy phase. As a consequence, we did not find long-range order for the perfect HAP AB_2 for $s_B = 0.037$, but we found it for $s_B = 0.0269$ which is a slightly lower value.

The presence of gaps in the phonon frequency spectrum is another important characteristic of the structure AB_2. No vibrations are possible for frequencies within the gap. The phonon gaps of the phase AB_2 for $m^* = s_B$, i. e., when the particles have different masses, are larger than the ones for $m^* = 1$. Furthermore, for $m^* = s_B$, the phonon gaps occur between acoustical and optical modes as well as between the optical modes, while for $m^* = 1$ the phonon gaps appear only between the optical modes. The thick line in Fig. 4.7 is due to two optical branches very close to each other that are not distinguishable on the scale used in the figure.

To conclude the analysis of the phase AB_2, we show in Figure 4.8 the behavior of the phonon frequencies of this phase for values of s_B within the range of stability. In each case, we can notice a small increase of the frequencies when we increase the dipole moment ratio. This is an expected result since the interaction energy between the particles becomes stronger when the value of s_B is increased (see Equation (3.2)). However, the transverse acoustical branch softens along the ΓX direction (see Figs. 4.8c e 4.8d) when $s_B = 0.0251$ since this value is close to the limit of stability.

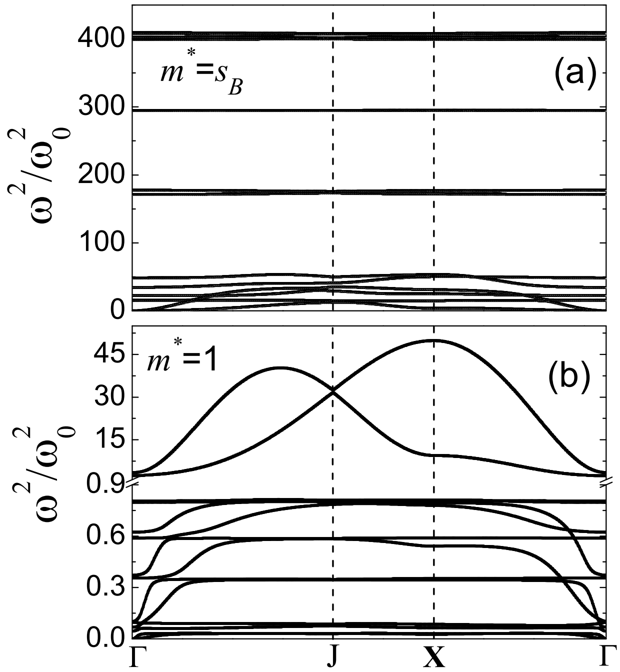

Figure 4.9: Square of the phonon frequencies of the phase AB_6 for $s_B = 0.002$ in units of $\omega_0^2 = \mu_A^2 \rho_A^{5/2}/m_A$ for (a) $m^* = s_B$ and (b) $m^* = 1$.

For the structures AB_3 and AB_5 shown in Figs. 4.1(b) and 4.1(c), respectively, we found that they are unstable for any dipole moment ratio, since imaginary phonon frequencies are found. In other words, long-range order is not possible for the configurations AB_3 and AB_5 independently of the value of the dipole moment ratio. Since in the harmonic approximation, the particles execute only small vibrations around their equilibrium positions, one can not state that the structures AB_3 and AB_5 are stable at $T = 0$, as it was mentioned for the phase AB_5 in Ref. [5]. Our result clearly shows that calculations of the energy of a given lattice structure, even after minimization with respect to some parameters, at $T = 0$, do not guarantee that the obtained MECs are stable.

In Fig. 4.9 we present the square of the phonon frequencies of the phase AB_6 for $s_B = 0.002$. For the AB_6 configuration, we found that the interval of stability is $0 \leq s_B \leq 0.0043$. Therefore, if we considered not only the large A particles, there is no long-range AB_6 order for $s_B = 0.037$ which is consistent with the experiments reported in Ref. [5]. However, the most important result for the AB_6 configuration is the considerable increase of the phonon gaps between the optical modes when the particles have different masses. As a consequence, there is a large number of frequencies for which the AB_6 structure can not sustain vibrations. On the other hand, when the particles have the same mass only a small phonon gap is found, between the optical modes, similarly to the phase AB_2.

Figure 4.10 shows the dispersion relation of the configuration $S(AB)$ for $s_B = 0.25$. Again, on the basis of the requirement of real phonon frequencies, we found that the interval of stability of the alloy $S(AB)$ is $0.038 \leq s_B \leq 0.29$. Interestingly, in this case, we do not have stability for $s_B = 0$, i. e., when only one particle is present in the unit cell. It is well known that a 2D system of particles interacting through a Coulomb potential when arranged in a square Bravais lattice is unstable [34]. Here, the same conclusion is reached when the particles interact through a repulsive dipole-dipole potential. Unlike the phases AB_2 and AB_6 that have phonon gaps for $m^* = s_B$ and $m^* = 1$, the configuration $S(AB)$ exhibits gaps in the phonon spectrum only for $m^* = s_B$. This is an example of how the properties of the system depend on the composition ξ. The interval of stability of some of the colloidal alloys are reported in Table 4.1.

Table 4.1: Interval of stability of some colloidal alloys. The phases AB_3 and AB_5 are unstable and therefore are not listed.

Phases	AB_2	AB_6	$S(AB)$
Stable	$0 \leq s_B \leq 0.0269$	$0 \leq s_B \leq 0.0043$	$0.038 \leq s_B \leq 0.29$

The sound velocity of the transverse acoustical (TA) mode, $\nu_{TA} = d\omega_{TA}/dq|_{q\to 0}$, is shown for the stable configurations AB_2, AB_6 and $S(AB)$, in Figs. 4.11, 4.12, and 4.13, respectively, along the directions (1,0) and (1,1) (in what follows, the symbol 0^+ means that we are not considering $s_B = 0$, but only s_B values very close to zero). For these phases, the sound velocity is large in the case the particles have different masses. For the structure AB_2, in both directions, we found the sound velocity decreases with increasing s_B. However, the sound velocity along the direction ΓJ decreases faster than in the direction $X\Gamma$. On the other hand, for the configuration AB_6 we have a different behavior for the sound velocity. In the direction ΓJ, the sound velocity decreases

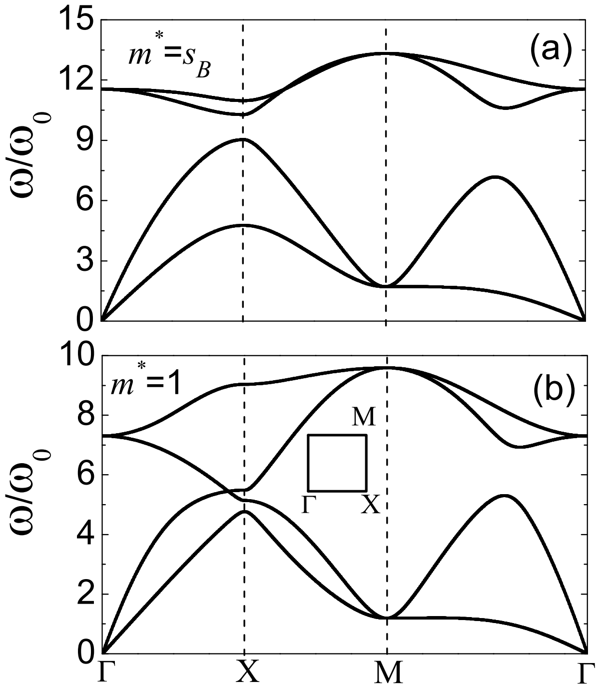

Figure 4.10: Dispersion relation of the phase $S(AB)$ for $s_B = 0.25$ along the high-symmetry directions in reciprocal space (a) for $m^* = s_B$ and (b) for $m^* = 1$. The high-symmetry points Γ, X and M are shown in the inset of (b).

monotonically with increasing s_B, while along the direction $X\Gamma$ the sound velocity decreases up to $s_B = 0.00251$, where the minimum sound velocities $\nu_{TA}/\nu_0 = 1.07608$ and $\nu_{TA}/\nu_0 = 0.40973$ are observed for $m^* = s_B$ and $m^* = 1$, respectively.

For the configuration $S(AB)$, the s_B-dependence of the sound velocity is completely different from the one found for the phases AB_2 and AB_6 as is shown in Fig. 4.13. In the direction ΓX, the velocity increases monotonically with increasing s_B, while the opposite behavior is found along the direction $M\Gamma$. We were able to fit the sound velocity of the phases AB_2, AB_6 and $S(AB)$ to the expression

$$\nu_{TA}/\nu_0 = v_0 + v_1 s_B + v_2 s_B^2 \tag{4.19}$$

where the coefficients v_i are reported in Tables 4.2, 4.3 and 4.4, respectively.

Table 4.2: Fitting parameters for the sound velocity of the phase AB_2.

AB_2	$m^* = s_B$	$m^* = s_B$	$m^* = 1$	$m^* = 1$
Direction	ΓJ	$X\Gamma$	ΓJ	$X\Gamma$
v_0	1.289	1.289	0.744	0.743
v_1	−17.38	−18.32	−9.166	−9.745
v_2	−473.1	−314.4	−294.8	−200.0

In Figs. 4.14(a), 4.15, and 4.16 the s_B-dependence of the optical frequencies ω_{op} at the Γ point is presented for both cases $m^* = s_B$ and $m^* = 1$. The optical frequencies are associated

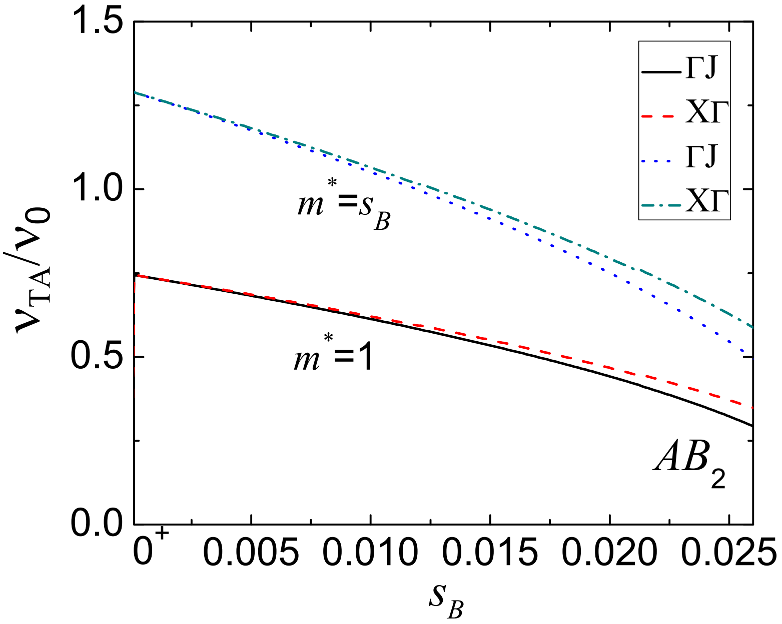

Figure 4.11: The sound velocity in units of $\nu_0 = \omega_0/\sqrt{\rho_A}$ of the transverse acoustical mode of the phase AB_2 as a function of s_B for $m^* = 1$ and $m^* = s_B$.

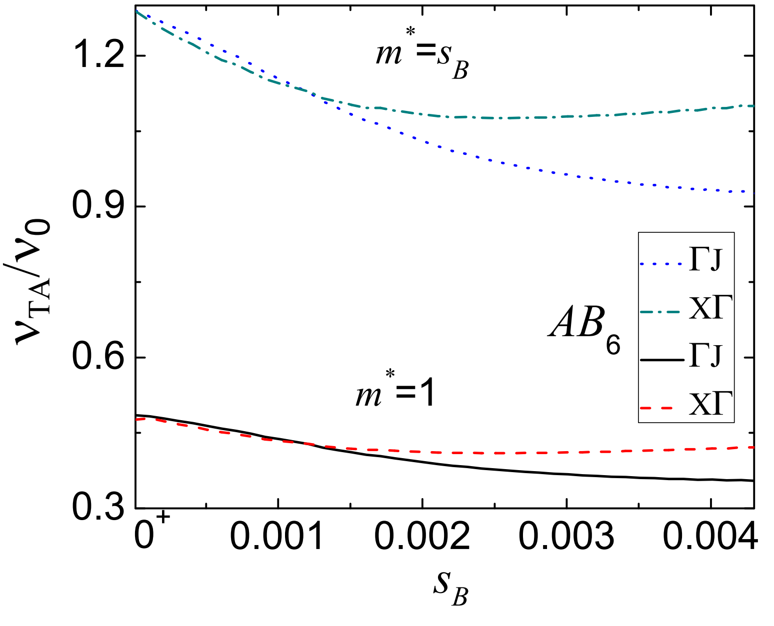

Figure 4.12: The sound velocity in units of $\nu_0 = \omega_0/\sqrt{\rho_A}$ of the transverse acoustical mode of the phase AB_6 as a function of s_B for $m^* = 1$ and $m^* = s_B$.

with the out-of-phase vibrations of the particles in the unit cell. In general, the number of optical frequencies n_{op} depends on the number of particles per unit cell n_p and the dimensionality of the system, being $n_{op} = 2n_p - 2$ for the 2D colloidal system at hand. As a general behavior, the

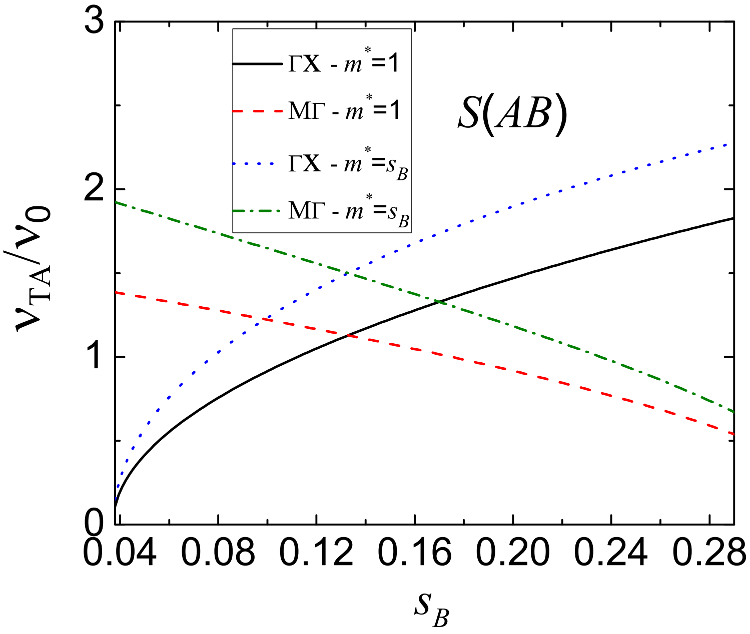

Figure 4.13: The sound velocity in units of $\nu_0 = \omega_0/\sqrt{\rho_A}$ of the transverse acoustical mode of the $S(AB)$ as a function of s_B for $m^* = 1$ and $m^* = s_B$.

Table 4.3: Fitting parameters for the sound velocity of the phase AB_6.

AB_6	$m^* = s_B$	$m^* = s_B$	$m^* = 1$	$m^* = 1$
Direction	ΓJ	$X\Gamma$	ΓJ	$X\Gamma$
v_0	1.289	1.288	0.485	0.476
v_1	−176.7	−142.9	−65.16	−50.90
v_2	20861.2	24930.7	7759.54	9060.95

optical frequencies for $m^* = s_B$ are larger than those for $m^* = 1$.

The phase AB_2 has four optical frequencies and the phase AB_6 has twelve, since these alloys have three and seven particles per unit cell, respectively. For the colloidal alloys AB_2 and AB_6, the different optical frequencies are non-degenerate. The jumps of the optical frequencies for the phase AB_2 in Fig. 4.14(a) are associated with the change of the positions of the small particles in the unit cell as a function of s_B, as can be seen in Fig. 4.14(b). On the other hand, a different behavior is found for the structure $S(AB)$. In this case, the two allowed optical phonon frequencies are degenerate, which is a consequence of the symmetry of the square lattice structure presented by that phase. The vibrations of the particles in the unit cell are equivalent in both directions.

To conclude, notice that the optical frequencies tend to zero when s_B approaches zero only in the case $m^* = 1$. In this limit ($s_B \to 0$) the interaction involving the small particles B becomes negligible, allowing the optical modes to be excited with a very low frequency.

Table 4.4: Fitting parameters for the sound velocity of the phase $S(AB)$.

$S(AB)$	$m^* = s_B$	$m^* = s_B$	$m^* = 1$	$m^* = 1$
Direction	ΓX	$M\Gamma$	ΓX	$M\Gamma$
v_0	0.001	2.015	-0.021	1.417
v_1	13.64	-2.985	10.22	-1.236
v_2	-20.02	-5.899	-13.25	-6.354

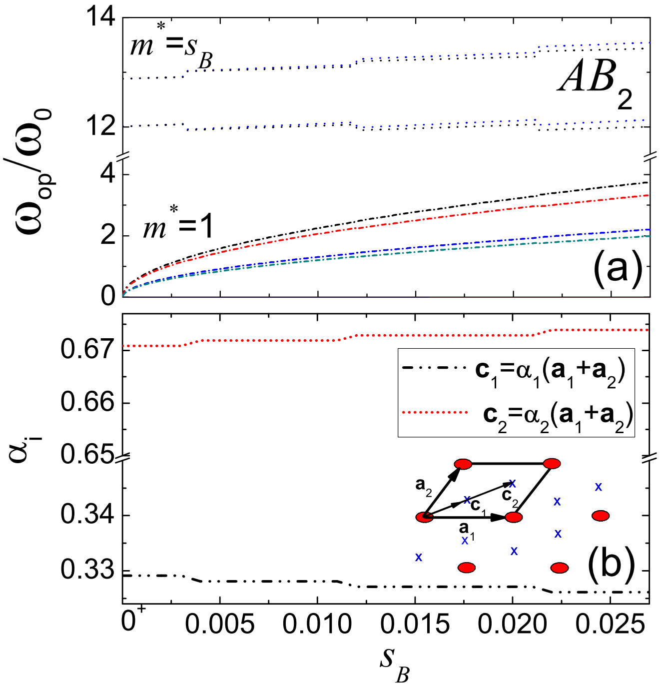

Figure 4.14: (a) The optical frequencies in units of ω_0 at the Γ point for AB_2 as a function of s_B for $m^* = s_B$ (dotted line) and $m^* = 1$ (short dash dotted line) and (b) positions of the small particles inside the unit cell of the structure AB_2 as a function of s_B.

4.4 Melting

Now we turn our discussion to the melting behavior of the system as a function of the dipole moment ratio s_B. The melting temperature will be calculated within the harmonic approximation using a Lindemann-like criterion. The original Lindemann criterion [59] states that the melting of a given structural phase occurs when the mean square displacement exceeds a threshold value of the mean inter-particle distance r_0 [59, 60, 61]:

$$\frac{< u^2 >}{r_0^2} = \delta^2 \quad , \tag{4.20}$$

where the parameter δ^2 is obtained numerically from, e. g., molecular dynamics simulation. The symbol $<>$ stands for a thermal average. The original Lindemann criterion is not applicable for 2D crystals because $< u^2 >$ diverges logarithmically with the size of the system [36, 61]. Bedanov *et al.* [61] showed through molecular dynamics simulations that the relative mean square

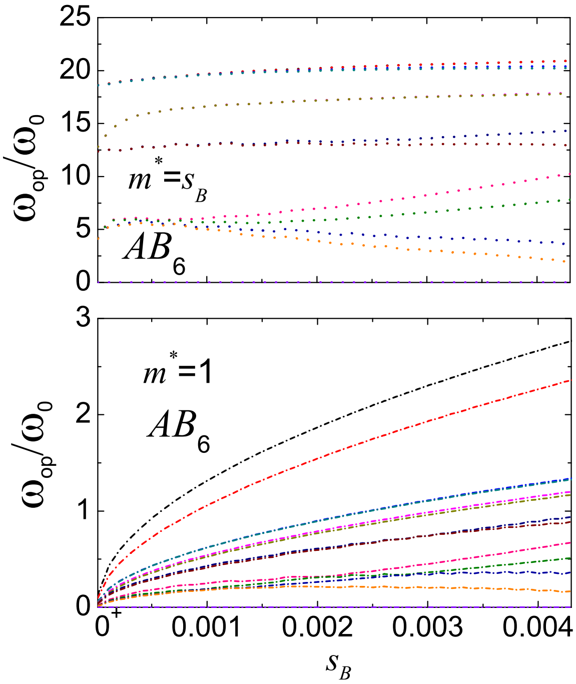

Figure 4.15: The optical frequencies in units of ω_0 at the Γ point for AB_6 as a function of s_B for $m^* = s_B$ and $m^* = 1$.

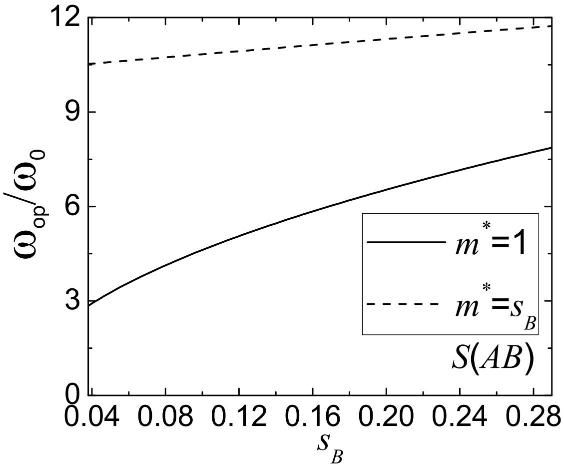

Figure 4.16: The optical frequencies in units of ω_0 at the Γ point for $S(AB)$ as a function of s_B for $m^* = s_B$ and $m^* = 1$.

displacement, given by

$$< |\vec{u}(\vec{R}) - \vec{u}(\vec{R}+\vec{a})|^2 > \quad , \tag{4.21}$$

is a well defined quantity for a 2D infinite system, where $\vec{u}(\vec{R})$ and $\vec{u}(\vec{R}+\vec{a})$ are the displacement vectors at site $\vec{R}$ and at its nearest-neighbor site $\vec{R}+\vec{a}$, respectively, and $\vec{a}$ is the lattice parameter.

In Ref. [61], the modified Lindemann-like criterion for 2D crystals was defined as

$$\frac{< |\vec{u}(\vec{R}) - \vec{u}(\vec{R}+\vec{a})|^2 >}{r_0^2} = \delta_m^2 \quad , \tag{4.22}$$

with the modified Lindemann parameter (δ_m^2) typically $\delta_m^2 \approx 0.1$. The melting of the B sub-lattice was studied in Ref. [24] using Monte Carlo simulations and the radial distribution function $g_{BB}(r)$ between the small particles was obtained. For instance, the calculated melting temperature of the B sub-lattice for the AB_2 configuration was $4.0 \pm 0.5 \times 10^{-3}$ for $s_B = 0.025$.

Here we will study the melting behavior of the large A particles. In this case, r_0 in Eq. (4.22) is the mean inter-particle distance between large particles which is related to the density as $r_0 = 1/\sqrt{\pi\rho_A}$. The parameter δ_m^2 for 2D dipole interaction [61] is $\delta_m^2 = 0.12$, and therefore, we will take this value in order to determine the melting temperature (T_M) of the A particles. In fact, the value of T_M calculated in the present work is an estimate. As shown recently, the B sub-lattice (small particles) is already melted at T_M, since the melting temperature of the A sub-lattice (large particles) was estimated to be two orders of magnitude larger than the one for the small particles [24]. In addition, the melting temperature calculated through the harmonic approximation depends on the frequencies of the phonon spectrum which are obtained at $T = 0$ by considering both sub-lattices ordered (e. g., see Eq. (4.30)). In the present colloidal alloys the distribution of the small B particles around the big A particles is symmetric. We argue here that since in the melted state the small particles are spread uniformly around the large particles, the effective interaction between small and large particles is very similar to the one found in the crystal structure at $T = 0$. In this case, the frequencies of the phonon spectrum obtained at $T = 0$ for the ordered arrangement of the colloidal alloy would also in some sense reflect the effective interaction between both types of particles at $T \neq 0$. Therefore, in spite of the B sub-lattice be already melted at the melting temperature of the A sub-lattice, we consider the phonon frequencies obtained for the complete ordered structure at $T = 0$. We stress again that the melting temperature of the large A particles obtained here is only an estimate but we expect that the qualitative trends and the order of magnitude to be correct.

The correlation function $< |\vec{u}(\vec{R})-\vec{u}(\vec{R}+\vec{a})|^2 >$ is obtained within the harmonic approximation and by considering only the nearest neighbors interactions. In general, each lattice site in the 2D colloidal alloys has several types of nearest neighbors, and the number and the distance of the nearest neighbors depend on the considered colloidal alloy. The melting behavior of the A sub-lattice will be studied as a function of the dipole moment ratio s_B for the case $m^* = 1$, i. e. when both types of particles have the same mass [16, 77] and for $m^* = s_B$.

The correlation function between A particles is given by [36, 37]:

$$\Delta u_{AA} = \frac{1}{N_A} \sum_{\alpha=x,y} \sum_{l=1}^{N_A} < |u_\alpha^A(0) - u_\alpha^A(l)|^2 >, \tag{4.23}$$

where $u_\alpha^A(l)$ is the αth component of the displacement vector of the lth nearest neighbor of type A and N_A is the number of nearest neighbors of type A. For the stable configurations AB_2 and AB_6 the A particles are ordered in a hexagonal lattice and therefore each of them has six nearest neighbors. On the other hand, for the phase $S(AB)$ the A particles form a square lattice with each particle having four nearest neighbors.

Using the normal coordinates transformation [37, 62],

$$u_\alpha^A(0) = \frac{1}{\sqrt{N m_A}} \sum_{\vec{q},j} e_\alpha^A(\vec{q},j) Q(\vec{q},j) \quad , \tag{4.24a}$$

$$u_\alpha^A(l) = \frac{1}{\sqrt{N m_A}} \sum_{\vec{q},j} e_\alpha^A(\vec{q},j) Q(\vec{q},j) e^{i\vec{q}.\vec{R}_A(l)} \quad , \tag{4.24b}$$

where m_A is the mass of the large particle, N the number of unit cells of the crystal, $e_\alpha^A(\vec{q},j)$ the αth component of the eigenvector of the jth normal mode of the large particle for the wave vector $\vec{q}$, $Q(\vec{q},j)$ the normal coordinate of the vibrational mode, and $\vec{R}_A(l)$ is the relative vector connecting one A particle at the origin to its lth nearest neighbor of type A. From the fact that the thermal average of $Q(\vec{q},j)Q^*(\vec{q}',j')$ is given by [37, 62]

$$< Q(\vec{q},j)Q^*(\vec{q}',j') >= \frac{k_B T}{\omega^2(\vec{q},j)} \delta_{\vec{q}\vec{q}'} \delta_{jj'} \tag{4.25}$$

where k_B is the Boltzmann constant and T is the temperature of the system, we obtain

$$< |u_\alpha^A(0) - u_\alpha^A(l)|^2 >= \frac{4 k_B T}{N m_A} \sum_{\vec{q},j} \frac{[e_\alpha^A(\vec{q},j)]^2}{\omega^2(\vec{q},j)} \sin^2 \frac{\vec{q}.\vec{R}_A(l)}{2} \quad . \tag{4.26}$$

Therefore, the expression for Δu_{AA} results in

$$\Delta u_{AA} = \frac{4 k_B T}{N m_A N_A} \Gamma_{AA} \quad , \tag{4.27}$$

with

$$\Gamma_{AA} = \sum_{\vec{q},j} \frac{[e_x^A(\vec{q},j)]^2 + [e_y^A(\vec{q},j)]^2}{\omega^2(\vec{q},j)} \sum_{l=1}^{N_A} \sin^2 \frac{\vec{q}.\vec{R}_A(l)}{2} \quad . \tag{4.28}$$

Now, the correlation function becomes

$$< |\vec{u}(\vec{R}) - \vec{u}(\vec{R} + \vec{a})|^2 >= \Delta u_{AA}, \tag{4.29}$$

and substituting this into the modified Lindemann criterion, we found

$$\begin{aligned}\Gamma_M &= \frac{4\pi}{NN_A\delta_m^2\rho_A^{3/2}a^3}\sum_{\vec{q},j}\frac{[e_x^A(\vec{q},j)]^2+[e_y^A(\vec{q},j)]^2}{\omega^2(\vec{q},j)/\omega_0^2}\times \\ &\sum_{l=1}^{N_A}\sin^2\frac{\vec{q}.\vec{R}_A(l)}{2}, \end{aligned} \tag{4.30}$$

where $\omega_0^2=\mu_A^2\rho_A^{5/2}/m_A$.

The melting temperature of dipolar systems is usually studied in terms of the dimensionless coupling parameter $\Gamma_M=\mu_A^2/k_BT_Ma^3$, which involves the potential and thermal energy. Here we will plot $1/\Gamma_M$ as a function of the dipole moment ratio s_B.

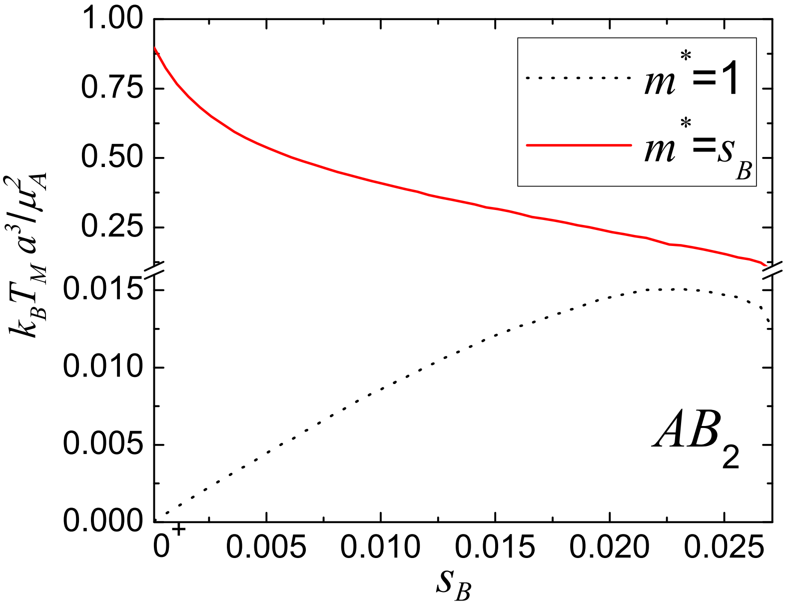

Figure 4.17: Melting temperature of the A sub-lattice of the phase AB_2 as a function of the dipole moment ratio. $m^*=1$ ($m^*=s_B$) means particles A and B with equal (different) masses. For $m^*=1$, the melting temperature assumes the maximum value $1/\Gamma_M=0.01507$ for $s_B=0.0231$.

In Fig. 4.17 we present the melting behavior of the structure AB_2 ($\xi=2/3$) as a function of the dipole moment ratio s_B for the cases with equal ($m^*=1$) and different ($m^*=s_B$) masses. Initially, we will focus on the case with $m^*=1$. For $s_B=0$, i. e., a one component dipolar system, we found $1/\Gamma_M\approx 0.15$, which is very close to the value $1/\Gamma_M\approx 0.11$ found in Refs. [24] and [78]. Besides, as an important finding, there is an optimum value of the dipole moment ratio s_B for which the melting temperature of the A sub-lattice reaches a maximum, i. e., for $s_B=0.0231$ the melting temperature has the maximum value $1/\Gamma_M=0.01507$. This is interesting since it can be used in future experimental studies of 2D binary colloidal systems of dipoles when one

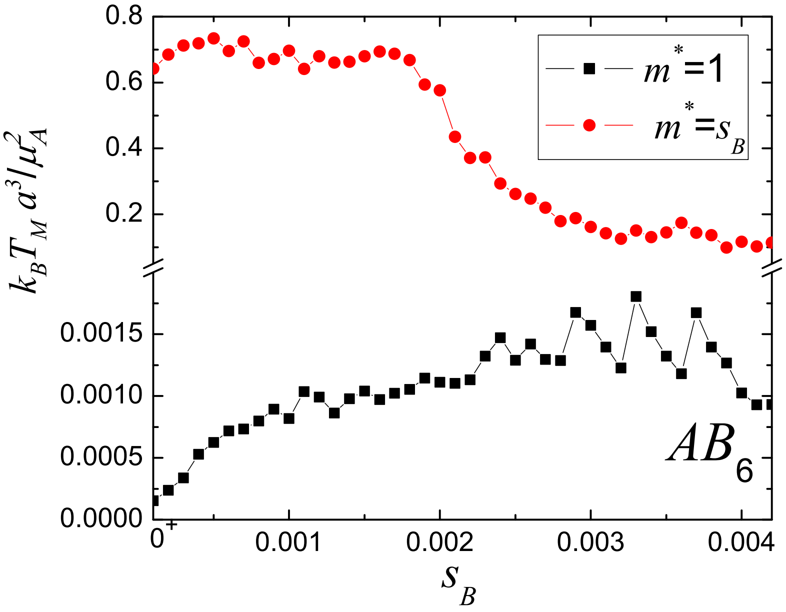

Figure 4.18: Melting temperature of the A sub-lattice for the structure AB_6 as a function of the dipole moment ratio. $m^* = 1$ ($m^* = s_B$) means particles A and B with equal (different) masses. The melting temperature for $m^* = 1$ reaches its maximum value when $s_B = 0.0033$.

wants to maximize the melting temperature. For $s_B = 0.025$ which is relevant to the experiments performed by Law *et al.* [5, 24], we find that $1/\Gamma_M = 1.45 \times 10^{-2}$. It means that, for $s_B = 0.025$, the melting point of the A sub-lattice is one order of magnitude larger than that of the B sub-lattice ($1/\Gamma_M = 4.0 \pm 0.5 \times 10^{-3}$) calculated using Monte Carlo simulations [24].

In the case of particles having different masses ($m^* = s_B$), we observe a very different qualitative behavior of the melting temperature as a function of s_B. The melting temperature decreases monotonically as s_B is increased. Quantitatively, the melting temperature is one order of magnitude larger than that of the case with equal masses $m^* = 1$. The presence of the lighter small dipoles makes the crystalline structure more stable against thermal fluctuations, as compared to the case with $m^* = 1$.

The melting temperature for the phase AB_6 ($\xi = 6/7$) as a function of s_B is presented in Fig. 4.18 for the cases $m^* = 1$ and $m^* = s_B$. The same general qualitative behavior found for the phase AB_2 is also observed for the phase AB_6, namely, the melting temperature for $m^* = 1$ presents a maximum for $s_B = 0.0033$, while for the case $m^* = s_B$ we observe that the melting temperature decreases with increasing s_B. Also, the melting temperature for $m^* = s_B$ is about two orders of magnitude larger than that for $m^* = 1$. The fluctuations of the melting temperature observed in Fig. 4.18 come from the non-symmetric distribution of small B particles around the big A particles.

The melting of the A sub-lattice for the structure $S(AB)$ as a function of s_B, for $m^* = 1$ and

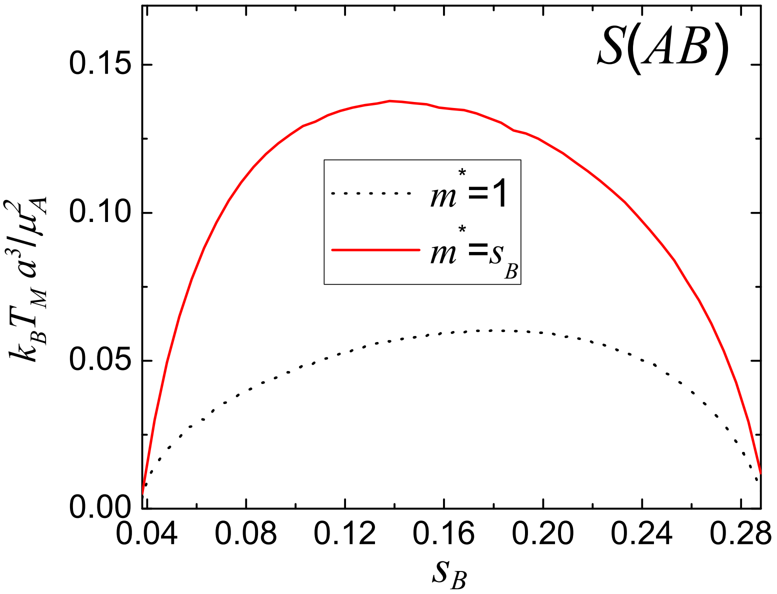

Figure 4.19: Melting temperature of the A sub-lattice for the configuration $S(AB)$ as a function of the dipole moment ratio. Here, for $m^* = 1$, the maximum temperature $1/\Gamma_M \approx 0.060$ takes place for $s_B = 0.18$, while for $m^* = s_B$, the maximum temperature $1/\Gamma_M \approx 0.138$ occurs for $s_B = 0.138$.

$m^* = s_B$, is presented in Fig. 4.19. Unlike the configurations AB_2 and AB_6, the phase $S(AB)$ has the same qualitative behavior for $m^* = 1$ and $m^* = s_B$. On the other hand, quantitatively, the maximum melting temperature for $m^* = 1$ ($1/\Gamma_M \approx 0.060$) is one order of magnitude smaller than that for $m^* = s_B$ ($1/\Gamma_M \approx 0.138$). This is another example of how the composition changes drastically the properties of the system.

4.5 Conclusions

We investigated the dynamical properties and melting transition of a 2D binary colloidal system of dipoles interacting through a dipole-dipole repulsive potential. Within the *harmonic approximation* we calculated the phonon spectra of the system as a function of the relative concentration of small particles, dipole moment ratio and mass ratio. We determined the interval of values of the dipole moment ratio s_B for which the colloidal alloys are stable and have long-range order. For instance, we found that the hexagonal AB_2 configuration has long-range order for $s_B \lesssim 0.0269$. Furthermore, unlike the $T = 0$ calculation of the energy for the phase AB_5 which was based on a minimization of the energy of a limited set of crystal structures, we found that the $T = 0$ phonon spectrum consists of imaginary frequencies, indicating that the AB_5 structure at $T = 0$ is unstable. We did not find a long-range AB_6 ordered configuration for $s_B = 0.037$ which is consistent with the experiments reported in Ref. [5].

The gaps in the phonon spectra were analyzed by changing the composition, mass ratio and the dipole moment ratio. E. g., the phonon gaps of the configurations AB_2 and AB_6 are considerably larger when the particles have different masses. Furthermore, unlike the colloidal alloys AB_2 and AB_6 that have phonon gaps when the particles have different masses as well as equal masses, the configuration $S(AB)$ exhibits phonon gaps only when the particles have different masses. This is an example of how the composition changes the properties of the system. The optical frequencies in the long-wavelength limit were discussed. The number of optical frequencies is associated with the number of particles per unit cell, i. e., the composition. The optical frequencies of the phase $S(AB)$ are degenerate while the ones of the configurations AB_2 and AB_6 are not. The common behavior that the optical frequencies go to zero when the dipole moment ratio tends to zero, does not hold when particles have different masses ($m^* = s_B$). We also analyzed the sound velocity of the transverse acoustical mode. As a general behavior, the sound velocity becomes large when the particles have different masses. Furthermore, the speed of sound depends strongly on the composition and the dipole moment ratio. For instance, for the composition $\xi = 6/7$ (AB_6) the sound velocity along the ΓX direction diminishes only until $s_B = 0.00251$, where the minimum speed of sound is obtained.

We estimated the melting temperature of the A sub-lattice as a function of the dipole moment ratio and composition, within the harmonic approximation, and using the modified Lindemann criterion. For each stable configuration, we determined the value of the dipole moment ratio for which the melting temperature is a maximum. This is also an important result that will be useful in future experiments of 2D binary colloidal systems of dipoles.

Chapter 5

Conclusions

In this chapter, we summarize the main results obtained in this thesis.

First, we studied a 2D classical bilayer system of charged magnetic dipoles. Six ordered structural phases (OCH, SS, SRect, SRhomb, SH and MH) and one disordered phase were found to be the ground-state configurations as a function of the separation between the layers (η) and a parameter which is related to the ratio between the dipole moment (μ) and the charge (Q) of the particles ($\lambda = \mu^2 n/Q^2$, with n the density of particles).

The phonon spectrum of the different phases given in the (λ, η) phase diagram were obtained. A non-monotonic behavior of the phonon spectrum as a function of λ was found for the MH phase, which is related to the competition between the dipole and the Coulomb interaction [37]. We found that the non-monotonic behavior of the phonon spectrum is associated to a change from attractive to repulsive character in the total energy. Besides, since the melting temperature can be calculated from the normal mode frequencies (at least within the harmonic approximation), the non-monotonic behavior of the phonon spectrum might play an important role when determining the melting temperature for different λ.

The stability of the phases obtained from the phonon spectrum were compared with the phase boundaries for different values of (λ, η). As an important finding, the presence of both electric and magnetic interaction stabilizes up to three phases in some η-interval of a given ground state configuration, and this fact should have profound implications on the melting temperature, since structural transitions may take place for temperatures $T \neq 0$.

We found a region in the (λ, η) phase diagram where the SH phase has the lowest energy among the considered 9 crystal structures while from the phonon spectrum it appears to be unstable. Monte Carlo simulations were used to determine the ordered structure in this region, and we found that the lowest energy configuration corresponds to a distorted hexagonal lattice structure, where the lattice positions are slightly disordered.

Second, we investigated the melting behavior of the previous system using the modified Lindemann criterion in order to estimate the melting temperature of the system. We observed that the maximum melting temperature of the structural phases gets smaller when the distance between the layers increases, for a fixed λ. Moreover, due to strong coupling between the dipoles, the MH phase has the highest melting temperature. Another observation is the decrease (increase) of the melting temperature of the SH phase (MH phase), when the magnetic character of the particles becomes large, i. e., when λ increases. Therefore, it is possible to alternate between staggered and matched arrangements by changing the parameter λ as, for example, through an external magnetic field or the pH of the medium. Nevertheless, our most important result is the re-entrant melting behavior of the MH phase when $\lambda \gtrsim 1.1$. It means that, at a fixed temperature, a sequence of solid-liquid transitions takes place when the distance between the planes η is increased, for $\lambda \gtrsim 1.1$.

Last, we investigated the dynamical properties and melting transition of a 2D binary colloidal system of dipoles interacting through a dipole-dipole repulsive potential. We determined the interval of values of the dipole moment ratio s_B for which the colloidal alloys are stable and have long-range order. For instance, we found that the hexagonal AB_2 configuration has long-range order for $s_B \lesssim 0.0269$.

The gaps in the phonon spectra were analyzed by changing the composition, mass ratio and the dipole moment ratio. E. g., the phonon gaps of the configurations AB_2 and AB_6 are considerably large when the particles have different masses. Furthermore, unlike the colloidal alloys AB_2 and AB_6 that have phonon gaps when the particles have different masses as well as equal masses, the configuration $S(AB)$ exhibits phonon gaps only when the particles have different masses.

We estimated the melting temperature of the A sub-lattice as a function of the dipole moment ratio and composition, within the harmonic approximation, and using the modified Lindemann criterion. For each stable configuration, we determined the value of the dipole moment ratio for which the melting temperature is a maximum.

Appendix A

Energy per particle using Ewald summation

In this appendix, we present the details of the calculation of the energy per particle for the bilayer system of charged magnetic dipoles.

A.1 Electric case

A.1.1 Coulomb interaction energy per particle in each layer

From equation (2.6a), we have that

$$E_{0E} = \sum_{\vec{R}\neq\vec{0}} \frac{Q^2}{|\vec{R}|} \tag{A.1}$$

$$E_{0E} = Q^2 \lim_{\vec{r}\to 0} \left[\sum_{\vec{R}} \frac{1}{|\vec{r}-\vec{R}|} - \frac{1}{r} \right] \tag{A.2}$$

Following the Refs. [35, 36], we define the function:

$$T_0(\vec{r},\vec{q}) = e^{-i\vec{q}.\vec{r}} \sum_{\vec{R}} \frac{e^{i\vec{q}.(\vec{r}-\vec{R})}}{|\vec{r}-\vec{R}|} - \frac{1}{r} \quad . \tag{A.3}$$

Then, we can rewrite equation $(A.2)$ in the following way:

$$E_{0E} = Q^2 \lim_{\vec{r}\to 0} T_0(\vec{r},\vec{0}) \quad . \tag{A.4}$$

Using the equations,

$$\mathrm{erf} + \mathrm{erfc} = 1 \tag{A.5}$$

$$\text{erf} = \frac{2}{\sqrt{\pi}} \int_0^x e^{-t^2} dt \tag{A.6}$$

$$\text{erfc} = \frac{2}{\sqrt{\pi}} \int_x^\infty e^{-t^2} dt. \tag{A.7}$$

we can write $1/|\vec{r} - \vec{R}|$ as

$$\frac{1}{|\vec{r} - \vec{R}|} = \frac{1}{|\vec{r} - \vec{R}|} [\text{erf}(\varepsilon |\vec{r} - \vec{R}|) + \text{erfc}(\varepsilon |\vec{r} - \vec{R}|)] \quad . \tag{A.8}$$

Substituting $(A.8)$ into $T_0(\vec{r}, \vec{q})$ we have:

$$T_0(\vec{r}, \vec{q}) = e^{-i\vec{q}.\vec{r}} \sum_{\vec{R}} e^{i\vec{q}.(\vec{r}-\vec{R})} \frac{[\text{erf}(\varepsilon |\vec{r} - \vec{R}|) + \text{erfc}(\varepsilon |\vec{r} - \vec{R}|)]}{|\vec{r} - \vec{R}|} - \frac{1}{r} \tag{A.9}$$

$$T_0(\vec{r}, \vec{q}) \;\; = \;\; e^{-i\vec{q}.\vec{r}} \sum_{\vec{R}} e^{i\vec{q}.(\vec{r}-\vec{R})} \frac{\text{erf}(\varepsilon |\vec{r} - \vec{R}|)}{|\vec{r} - \vec{R}|} + e^{-i\vec{q}.\vec{r}} \sum_{\vec{R}} e^{i\vec{q}.(\vec{r}-\vec{R})} \frac{\text{erfc}(\varepsilon |\vec{r} - \vec{R}|)}{|\vec{r} - \vec{R}|} - \frac{1}{r} \tag{A.10}$$

$$\begin{aligned} T_0(\vec{r}, \vec{q}) \;\; = \;\; & e^{-i\vec{q}.\vec{r}} \sum_{\vec{R}} e^{i\vec{q}.(\vec{r}-\vec{R})} \frac{\text{erf}(\varepsilon |\vec{r} - \vec{R}|)}{|\vec{r} - \vec{R}|} + e^{-i\vec{q}.\vec{r}} \sum_{\vec{R} \neq \vec{0}} e^{i\vec{q}.(\vec{r}-\vec{R})} \frac{\text{erfc}(\varepsilon |\vec{r} - \vec{R}|)}{|\vec{r} - \vec{R}|} \\ & + \frac{\text{erfc}(\varepsilon |\vec{r}|)}{|\vec{r}|} - \frac{1}{r} \end{aligned} \tag{A.11}$$

Let us define

$$t = \gamma \xi \tag{A.12}$$

$$dt = \gamma d\xi \tag{A.13}$$

Thus,

$$\text{erf}(x) = \frac{2}{\sqrt{\pi}} \int_0^x e^{-t^2} dt = \frac{2}{\sqrt{\pi}} \int_0^{x/\gamma} \gamma e^{-\gamma^2 \xi^2} d\xi \tag{A.14}$$

gives us

$$\frac{\text{erf}(\varepsilon \gamma)}{\gamma} = \frac{2}{\sqrt{\pi}} \int_0^\varepsilon e^{-\gamma^2 \xi^2} d\xi \tag{A.15}$$

Substituting $(A.15)$ into $(A.11)$, we have that

$$\begin{aligned} T_0(\vec{r},\vec{q}) &= \sum_{\vec{R}} e^{-i\vec{q}.\vec{R}} \frac{2}{\sqrt{\pi}} \int_0^{\varepsilon} e^{-|\vec{r}-\vec{R}|^2\xi^2} d\xi + e^{-i\vec{q}.\vec{r}} \sum_{\vec{R}\neq\vec{0}} e^{i\vec{q}.(\vec{r}-\vec{R})} \frac{\mathrm{erfc}(\varepsilon|\vec{r}-\vec{R}|)}{|\vec{r}-\vec{R}|} \\ & \quad + \frac{\mathrm{erfc}(\varepsilon|\vec{r}|)}{|\vec{r}|} - \frac{1}{r} \end{aligned} \tag{A.16}$$

Now, we work with the first term of this equation:

$$\sum_{\vec{R}} e^{-i\vec{q}.\vec{R}} \frac{2}{\sqrt{\pi}} \int_0^{\varepsilon} e^{-|\vec{r}-\vec{R}|^2\xi^2} d\xi = \frac{2}{\sqrt{\pi}} \int_0^{\varepsilon} \left[\sum_{\vec{R}} e^{-|\vec{r}-\vec{R}|^2\xi^2} e^{-i\vec{q}.\vec{R}} \right] d\xi \tag{A.17}$$

Substituting the following transformation (the 2D θ-function transformation)

$$\sum_{\vec{R}} e^{-|\vec{r}-\vec{R}|^2\xi^2} e^{-i\vec{q}.\vec{R}} = \frac{n_s\pi}{\xi^2} \sum_{\vec{G}} e^{-|\vec{q}+\vec{G}|^2/4\xi^2} e^{-i(\vec{q}+\vec{G}).\vec{r}} \tag{A.18}$$

into $(A.17)$, we have that

$$2\sqrt{\pi} n_s \sum_{\vec{G}} e^{-i(\vec{q}+\vec{G}).\vec{r}} \left[\int_0^{\varepsilon} \frac{1}{\xi^2} e^{-|\vec{q}+\vec{G}|^2/4\xi^2} d\xi \right] \quad . \tag{A.19}$$

If

$$t = |\vec{q}+\vec{G}|/2\xi \tag{A.20}$$

then

$$\int_0^{\varepsilon} \frac{1}{\xi^2} e^{-|\vec{q}+\vec{G}|^2/4\xi^2} d\xi = \frac{2}{|\vec{q}+\vec{G}|} \left[\int_{|\vec{q}+\vec{G}|/2\varepsilon}^{\infty} e^{-t^2} dt \right] = \frac{\sqrt{\pi}}{|\vec{q}+\vec{G}|} \mathrm{erfc}\left(\frac{|\vec{q}+\vec{G}|}{2\varepsilon} \right) \tag{A.21}$$

and $(A.19)$ becomes

$$2\pi n_s \sum_{\vec{G}} \frac{e^{-i(\vec{q}+\vec{G}).\vec{r}}}{|\vec{q}+\vec{G}|} \mathrm{erfc}\left(\frac{|\vec{q}+\vec{G}|}{2\varepsilon} \right) \quad . \tag{A.22}$$

Let us define

$$\Phi(x) = \sqrt{\frac{\pi}{x}} \mathrm{erfc}(\sqrt{x}) \quad . \tag{A.23}$$

Thus,

$$\frac{\mathrm{erfc}(\varepsilon r)}{r} = \frac{\varepsilon}{\sqrt{\pi}} \Phi(\varepsilon^2 r^2) \quad . \tag{A.24}$$

Since $\varepsilon = \sqrt{\pi n_s}$, we have that

$$\frac{\mathrm{erfc}(\sqrt{\pi n_s} r)}{r} = \sqrt{n_s} \Phi(\pi n_s r^2) \quad . \tag{A.25}$$

Analogously,

$$\frac{\mathrm{erfc}(\varepsilon|\vec{r}-\vec{R}|)}{|\vec{r}-\vec{R}|} = \sqrt{n_s}\Phi(\varepsilon^2|\vec{r}-\vec{R}|^2) \tag{A.26}$$

gives us

$$\frac{\mathrm{erfc}(\sqrt{\pi n_s}|\vec{r}-\vec{R}|)}{|\vec{r}-\vec{R}|} = \sqrt{n_s}\Phi(\pi n_s|\vec{r}-\vec{R}|^2) \tag{A.27}$$

and

$$\frac{\mathrm{erfc}(|\vec{q}+\vec{G}|/2\varepsilon)}{|\vec{q}+\vec{G}|} = \frac{\mathrm{erfc}(|\vec{q}+\vec{G}|/2\sqrt{\pi n_s})}{|\vec{q}+\vec{G}|} = \frac{1}{2\pi\sqrt{n_s}}\Phi\left(\frac{|\vec{q}+\vec{G}|^2}{4\pi n_s}\right) \quad . \tag{A.28}$$

Then,

$$\begin{aligned} T_0(\vec{r},\vec{q}) \quad = \quad & \sqrt{n_s}\sum_{\vec{G}} e^{-i(\vec{q}+\vec{G}).\vec{r}}\Phi\left(\frac{|\vec{q}+\vec{G}|^2}{4\pi n_s}\right) + \sqrt{n_s}\sum_{\vec{R}\neq\vec{0}} e^{-i\vec{q}.\vec{R}}\Phi(\pi n_s|\vec{r}-\vec{R}|^2) + \\ & \sqrt{n_s}\Phi(\pi n_s|\vec{r}|^2) - \frac{1}{r} \quad , \end{aligned} \tag{A.29}$$

$$E_{0E} = Q^2 \lim_{\vec{r}\to 0} T_0(\vec{r},\vec{0}) \quad , \tag{A.30}$$

and

$$\begin{aligned} T_0(\vec{r},0) \quad = \quad & \sqrt{n_s}\sum_{\vec{G}} e^{-i\vec{G}.\vec{r}}\Phi\left(\frac{|\vec{G}|^2}{4\pi n_s}\right) + \sqrt{n_s}\sum_{\vec{R}\neq\vec{0}} \Phi(\pi n_s|\vec{r}-\vec{R}|^2) + \\ & \sqrt{n_s}\Phi(\pi n_s|\vec{r}|^2) - \frac{1}{r} \quad . \end{aligned} \tag{A.31}$$

Now, we are going to work with the last two terms of the equation ($A.31$). Thus,

$$\lim_{r\to 0}\left[\sqrt{n_s}\Phi(\pi n_s|\vec{r}|^2) - \frac{1}{r}\right] = \lim_{r\to 0}\left[-\frac{\mathrm{erf}(\sqrt{\pi n_s}r)}{r}\right] = -\sqrt{\pi n_s}\lim_{t\to 0}\frac{\mathrm{erf}(t)}{t} \tag{A.32}$$

Using the Taylor series of the error function, we have that

$$\lim_{x\to 0}\frac{\mathrm{erf}(x)}{x} = \frac{2}{\sqrt{\pi}} \tag{A.33}$$

and then,

$$\lim_{r\to 0}\left[\sqrt{n_s}\Phi(\pi n_s|\vec{r}|^2) - \frac{1}{r}\right] = -2\sqrt{n_s} \quad . \tag{A.34}$$

For the first term of the equation $(A.31)$, we have that

$$\lim_{r\to 0}\sqrt{n_s}\sum_{\vec{G}} e^{-i\vec{G}.\vec{r}}\Phi\left(\frac{|\vec{G}|^2}{4\pi n_s}\right) = \sqrt{n_s}\sum_{\vec{G}}\Phi\left(\frac{|\vec{G}|^2}{4\pi n_s}\right) = \sqrt{n_s}\,\Phi\left(\frac{|\vec{G}|^2}{4\pi n_s}\right)\Bigg|_{G=0} + \sqrt{n_s}\sum_{\vec{G}\neq 0}\Phi\left(\frac{|\vec{G}|^2}{4\pi n_s}\right) \quad . \tag{A.35}$$

From equations $(A.5)$ e $(A.23)$, we obtain

$$\lim_{r\to 0}\sqrt{n_s}\sum_{\vec{G}} e^{-i\vec{G}.\vec{r}}\Phi\left(\frac{|\vec{G}|^2}{4\pi n_s}\right) = \frac{2\pi n_s}{G}\bigg|_{G=0} - \left[\frac{2\pi n_s}{G}\mathrm{erf}\left(\frac{G}{2\sqrt{\pi n_s}}\right)\right]\bigg|_{G=0} + \sqrt{n_s}\sum_{\vec{G}\neq 0}\Phi\left(\frac{|\vec{G}|^2}{4\pi n_s}\right) \tag{A.36}$$

and using the equation $(A.33)$, we can write

$$\lim_{r\to 0}\sqrt{n_s}\sum_{\vec{G}} e^{-i\vec{G}.\vec{r}}\Phi\left(\frac{|\vec{G}|^2}{4\pi n_s}\right) = \frac{2\pi n_s}{G}\bigg|_{G=0} - 2\sqrt{n_s} + \sqrt{n_s}\sum_{\vec{G}\neq 0}\Phi\left(\frac{|\vec{G}|^2}{4\pi n_s}\right) \tag{A.37}$$

But,

$$\vec{G} = 2\pi n_s(\hat{z}\times\vec{R}) \tag{A.38}$$

and since $\hat{z}$ is a unit vector perpendicular to the layers, we have that

$$G = 2\pi n_s R \tag{A.39}$$

$$\frac{G^2}{4\pi n_s} = \pi n_s R^2 \quad . \tag{A.40}$$

Thus,

$$\lim_{r\to 0}\sqrt{n_s}\sum_{\vec{G}} e^{-i\vec{G}.\vec{r}}\Phi\left(\frac{|\vec{G}|^2}{4\pi n_s}\right) = \frac{2\pi n_s}{G}\bigg|_{G=0} - 2\sqrt{n_s} + \sqrt{n_s}\sum_{\vec{R}\neq 0}\Phi\left(\pi n_s R^2\right) \tag{A.41}$$

and

$$\lim_{r\to 0} T_0(\vec{r},0) = \frac{2\pi n_s}{G}\bigg|_{G=0} - 2\sqrt{n_s} + \sqrt{n_s}\sum_{\vec{R}\neq 0}\Phi\left(\pi n_s R^2\right) + \sqrt{n_s}\sum_{\vec{R}\neq\vec{0}}\Phi(\pi n_s|\vec{R}|^2) - 2\sqrt{n_s} \tag{A.42}$$

gives us,

$$E_{0E} \;=\; \left.\frac{2\pi Q^2 n_s}{G}\right|_{G=0} + 2Q^2\sqrt{n_s}\sum_{\vec{R}\neq 0}\Phi\left(\pi n_s R^2\right) - 4Q^2\sqrt{n_s} \quad . \tag{A.43}$$

The divergent term in the last equation is exactly balanced by the interaction energy with a background $\rho_+ = Qn_s$, located in the same layer [34, 36]. This interaction energy is given by

$$E_{0E}^{B} = -Q\rho_+\int\frac{d^2r}{|\vec{r}|} = -\left.\frac{2\pi Q^2 n_s}{q}\right|_{q=0} \tag{A.44}$$

and then, we obtain (with $n_s = n/2$)

$$E_{0E} = Q^2\sqrt{n/2}A \quad , \tag{A.45}$$

where

$$A = 2\sum_{\vec{R}\neq\vec{0}}\Phi(\pi n|\vec{R}|^2/2) - 4 \quad . \tag{A.46}$$

A.1.2 Coulomb interaction energy per particle between particles in distinct layers

The equation (2.7a) is given by

$$E_{IE} = \sum_{\vec{R}}\frac{Q^2}{[|\vec{R}+\vec{c}|^2+d^2]^{1/2}} \tag{A.47}$$

and following the Ref. [36], we define

$$T_I(\vec{r},\vec{q}) = e^{-i\vec{q}.\vec{r}}\sum_{\vec{R}}\frac{e^{i\vec{q}.(\vec{r}-\vec{R}+\vec{c})}}{[|\vec{r}-\vec{R}+\vec{c}|^2+d^2]^{1/2}} \tag{A.48}$$

and, thus

$$E_{IE} = Q^2\lim_{\vec{r}\to 0}T_I(\vec{r},\vec{0}) \quad . \tag{A.49}$$

With

$$\gamma^2 = |\vec{r}-\vec{R}+\vec{c}|^2+d^2 \tag{A.50}$$

and from equation $(A.5)$, we have:

$$T_I(\vec{r},\vec{q}) = e^{-i\vec{q}.\vec{r}}\sum_{\vec{R}}\frac{e^{i\vec{q}.(\vec{r}-\vec{R}+\vec{c})}}{\gamma} \tag{A.51}$$

$$T_I(\vec{r},\vec{q}) = e^{-i\vec{q}.\vec{r}} \sum_{\vec{R}} \frac{e^{i\vec{q}.(\vec{r}-\vec{R}+\vec{c})}}{\gamma}[\mathrm{erf}(\varepsilon\gamma) + \mathrm{erfc}(\varepsilon\gamma)] \tag{A.52}$$

$$\begin{aligned} T_I(\vec{r},\vec{q}) \;&=\; e^{-i\vec{q}.\vec{r}} \sum_{\vec{R}} \frac{e^{i\vec{q}.(\vec{r}-\vec{R}+\vec{c})}}{\gamma}\mathrm{erf}(\varepsilon\gamma) + \\ &\quad\; e^{-i\vec{q}.\vec{r}} \sum_{\vec{R}} \frac{e^{i\vec{q}.(\vec{r}-\vec{R}+\vec{c})}}{\gamma}\mathrm{erfc}(\varepsilon\gamma) \quad . \end{aligned} \tag{A.53}$$

Since

$$\frac{\mathrm{erf}(\varepsilon\gamma)}{\gamma} = \frac{2}{\sqrt{\pi}}\int_0^{\varepsilon} e^{-\gamma^2\xi^2} d\xi \tag{A.54}$$

we can write

$$\begin{aligned} T_I(\vec{r},\vec{q}) \;&=\; e^{-i\vec{q}.\vec{r}} \sum_{\vec{R}} e^{i\vec{q}.(\vec{r}-\vec{R}+\vec{c})} \frac{2}{\sqrt{\pi}}\int_0^{\varepsilon} e^{-\gamma^2\xi^2} d\xi + \\ &\quad\; e^{-i\vec{q}.\vec{r}} \sum_{\vec{R}} \frac{e^{i\vec{q}.(\vec{r}-\vec{R}+\vec{c})}}{\gamma}\mathrm{erfc}(\varepsilon\gamma) \end{aligned} \tag{A.55}$$

Let us define the function

$$T_A(\vec{r},\vec{q}) \;=\; e^{-i\vec{q}.\vec{r}} \sum_{\vec{R}} e^{i\vec{q}.(\vec{r}-\vec{R}+\vec{c})} \frac{2}{\sqrt{\pi}}\int_0^{\varepsilon} e^{-\gamma^2\xi^2} d\xi \tag{A.56}$$

and then,

$$T_I(\vec{r},\vec{q}) \;=\; T_A(\vec{r},\vec{q}) + e^{-i\vec{q}.\vec{r}} \sum_{\vec{R}} \frac{e^{i\vec{q}.(\vec{r}-\vec{R}+\vec{c})}}{\gamma}\mathrm{erfc}(\varepsilon\gamma) \quad . \tag{A.57}$$

Now, we are going to work with the equation $(A.55)$:

$$T_A(\vec{r},\vec{q}) \;=\; \frac{2}{\sqrt{\pi}}\int_0^{\varepsilon} \left[\sum_{\vec{R}} e^{-i\vec{q}.(\vec{R}-\vec{c})} e^{-\gamma^2\xi^2}\right] d\xi \tag{A.58}$$

$$T_A(\vec{r},\vec{q}) \;=\; \frac{2}{\sqrt{\pi}}\int_0^{\varepsilon} e^{i\vec{q}.\vec{c}} \left[\sum_{\vec{R}} e^{-i\vec{q}.\vec{R}} e^{-\gamma^2\xi^2}\right] d\xi \quad . \tag{A.59}$$

Using the equation $(A.49)$, we have that:

$$T_A(\vec{r},\vec{q}) \;=\; \frac{2}{\sqrt{\pi}}\int_0^{\varepsilon} e^{i\vec{q}.\vec{c}}\left[\sum_{\vec{R}} e^{-i\vec{q}.\vec{R}} e^{-[|\vec{r}-\vec{R}+\vec{c}|^2+d^2]\xi^2}\right] d\xi \tag{A.60}$$

$$T_A(\vec{r},\vec{q}) \;=\; \frac{2}{\sqrt{\pi}}\int_0^{\varepsilon} e^{i\vec{q}.\vec{c}}\left[\sum_{\vec{R}} e^{-i\vec{q}.\vec{R}} e^{-|\vec{r}-\vec{R}+\vec{c}|^2\xi^2}\right] e^{-d^2\xi^2} d\xi \tag{A.61}$$

$$T_A(\vec{r},\vec{q}) \;=\; \frac{2}{\sqrt{\pi}}\int_0^{\varepsilon} e^{i\vec{q}.\vec{c}}\left[\sum_{\vec{R}} e^{-i\vec{q}.\vec{R}} e^{-|(\vec{r}+\vec{c})-\vec{R}|^2\xi^2}\right] e^{-d^2\xi^2} d\xi \tag{A.62}$$

But,

$$\sum_{\vec{R}} e^{-|\vec{r}-\vec{R}|^2\xi^2} e^{-i\vec{q}.\vec{R}} = \frac{n_s\pi}{\xi^2}\sum_{\vec{G}} e^{-|\vec{q}+\vec{G}|^2/4\xi^2} e^{-i(\vec{q}+\vec{G}).\vec{r}} \tag{A.63}$$

gives us

$$\sum_{\vec{R}} e^{-|(\vec{r}+\vec{c})-\vec{R}|^2\xi^2} e^{-i\vec{q}.\vec{R}} = \frac{n_s\pi}{\xi^2}\sum_{\vec{G}} e^{-|\vec{q}+\vec{G}|^2/4\xi^2} e^{-i(\vec{q}+\vec{G}).(\vec{r}+\vec{c})} \tag{A.64}$$

and thus,

$$T_A(\vec{r},\vec{q}) \;=\; \frac{2}{\sqrt{\pi}} n_s\pi \sum_{\vec{G}} e^{-i(\vec{q}+\vec{G}).\vec{r}} e^{-i\vec{G}.\vec{c}}\left[\int_0^{\varepsilon}\frac{1}{\xi^2} e^{-|\vec{q}+\vec{G}|^2/4\xi^2} e^{-d^2\xi^2} d\xi\right] \quad . \tag{A.65}$$

Let us define the integral I as

$$I = \int_0^{\varepsilon}\frac{1}{\xi^2} e^{-|\vec{q}+\vec{G}|^2/4\xi^2} e^{-d^2\xi^2} d\xi \quad . \tag{A.66}$$

Using the variable

$$t = \frac{|\vec{q}+\vec{G}|}{2\xi} \tag{A.67}$$

$$dt = -\frac{|\vec{q}+\vec{G}|}{2\xi^2} d\xi \tag{A.68}$$

$$-2\frac{dt}{|\vec{q}+\vec{G}|} = \frac{d\xi}{\xi^2} \tag{A.69}$$

we have that, if $\xi = 0$, then $t = \infty$. On the other hand, if $\xi = \varepsilon$, then $t = \frac{|\vec{q}+\vec{G}|}{2\varepsilon}$. Therefore, the integral I becomes

$$I = \frac{2}{|\vec{q}+\vec{G}|} \int_{\frac{|\vec{q}+\vec{G}|}{2\varepsilon}}^{\infty} e^{-d^2|\vec{q}+\vec{G}|^2/4t^2} e^{-t^2} dt \tag{A.70}$$

$$I = \frac{2}{|\vec{q}+\vec{G}|} \int_{\frac{|\vec{q}+\vec{G}|}{2\varepsilon}}^{\infty} e^{-\left[t^2 + \left(\frac{d|\vec{q}+\vec{G}|}{2}\right)^2 \frac{1}{t^2}\right]} dt \tag{A.71}$$

and using the result

$$\int_x^{\infty} e^{-\left[t^2+\frac{\alpha^2}{t^2}\right]} dt = \frac{\sqrt{\pi}}{4}\left[e^{2\alpha}\text{erfc}\left(x+\frac{\alpha}{x}\right) + e^{-2\alpha}\text{erfc}\left(x-\frac{\alpha}{x}\right)\right] \tag{A.72}$$

with

$$x = \frac{|\vec{q}+\vec{G}|}{2\varepsilon} \tag{A.73}$$

$$\alpha = \frac{d|\vec{q}+\vec{G}|}{2} \tag{A.74}$$

$$\frac{\alpha}{x} = \varepsilon d \tag{A.75}$$

we have that

$$\begin{aligned} \int_{\frac{|\vec{q}+\vec{G}|}{2\varepsilon}}^{\infty} e^{-\left[t^2 + \left(\frac{d|\vec{q}+\vec{G}|}{2}\right)^2 \frac{1}{t^2}\right]} dt \quad &= \quad \frac{\sqrt{\pi}}{4}\left[e^{d|\vec{q}+\vec{G}|}\text{erfc}\left(\frac{|\vec{q}+\vec{G}|}{2\varepsilon} + \varepsilon d\right) + \right. \\ & \left. e^{-d|\vec{q}+\vec{G}|}\text{erfc}\left(\frac{|\vec{q}+\vec{G}|}{2\varepsilon} - \varepsilon d\right)\right] \quad . \end{aligned} \tag{A.76}$$

Let us define $\varepsilon = \sqrt{\pi n_s}$. Defining the function $\Psi(x,y)$ given by

$$\Psi(x,y) = \frac{1}{2}\sqrt{\frac{\pi}{x}}\left[e^{\sqrt{4xy}}\text{erfc}\left(\sqrt{x}+\sqrt{y}\right) + e^{-\sqrt{4xy}}\text{erfc}\left(\sqrt{x}-\sqrt{y}\right)\right] \tag{A.77}$$

with

$$\sqrt{x} = \frac{|\vec{q}+\vec{G}|}{2\varepsilon} \tag{A.78}$$

$$x = \frac{|\vec{q}+\vec{G}|^2}{4\varepsilon^2} = \frac{|\vec{q}+\vec{G}|^2}{4\pi n_s} \tag{A.79}$$

$$\frac{1}{2}\sqrt{\frac{\pi}{x}} = \frac{\pi\sqrt{n_s}}{|\vec{q}+\vec{G}|} \tag{A.80}$$

$$\sqrt{y} = \varepsilon d = d\sqrt{\pi n_s} \tag{A.81}$$

$$y = d^2 \pi n_s \tag{A.82}$$

and, with $\eta = d\sqrt{n_s}$, we have that

$$y = \pi\eta^2 \quad . \tag{A.83}$$

With these definitions, we obtain

$$\begin{aligned}\Psi\left(\frac{|\vec{q}+\vec{G}|^2}{4\pi n_s}, \pi\eta^2\right) &= \frac{\pi\sqrt{n_s}}{|\vec{q}+\vec{G}|}\left[e^{d|\vec{q}+\vec{G}|}\mathrm{erfc}\left(\frac{|\vec{q}+\vec{G}|}{2\varepsilon}+\varepsilon d\right)+\right.\\ &\left. e^{-d|\vec{q}+\vec{G}|}\mathrm{erfc}\left(\frac{|\vec{q}+\vec{G}|}{2\varepsilon}-\varepsilon d\right)\right]\end{aligned} \tag{A.84}$$

$$\begin{aligned}\frac{|\vec{q}+\vec{G}|}{\pi\sqrt{n_s}}\Psi\left(\frac{|\vec{q}+\vec{G}|^2}{4\pi n_s}, \pi\eta^2\right) &= \left[e^{d|\vec{q}+\vec{G}|}\mathrm{erfc}\left(\frac{|\vec{q}+\vec{G}|}{2\varepsilon}+\varepsilon d\right)+\right.\\ &\left. e^{-d|\vec{q}+\vec{G}|}\mathrm{erfc}\left(\frac{|\vec{q}+\vec{G}|}{2\varepsilon}-\varepsilon d\right)\right]\end{aligned} \tag{A.85}$$

Substituting $(A.84)$ into $(A.75)$, we have that

$$\int_{\frac{|\vec{q}+\vec{G}|}{2\varepsilon}}^{\infty} e^{-\left[t^2+\left(\frac{d|\vec{q}+\vec{G}|}{2}\right)^2\frac{1}{t^2}\right]}dt = \frac{\sqrt{\pi}}{4}\frac{|\vec{q}+\vec{G}|}{\pi\sqrt{n_s}}\Psi\left(\frac{|\vec{q}+\vec{G}|^2}{4\pi n_s}, \pi\eta^2\right) \tag{A.86}$$

therefore,

$$I = \frac{2}{|\vec{q}+\vec{G}|}\int_{\frac{|\vec{q}+\vec{G}|}{2\varepsilon}}^{\infty} e^{-\left[t^2+\left(\frac{d|\vec{q}+\vec{G}|}{2}\right)^2\frac{1}{t^2}\right]}dt = \frac{2}{|\vec{q}+\vec{G}|}\frac{\sqrt{\pi}}{4}\frac{|\vec{q}+\vec{G}|}{\pi\sqrt{n_s}}\Psi\left(\frac{|\vec{q}+\vec{G}|^2}{4\pi n_s}, \pi\eta^2\right) \tag{A.87}$$

$$I = \frac{2}{|\vec{q}+\vec{G}|}\int_{\frac{|\vec{q}+\vec{G}|}{2\varepsilon}}^{\infty} e^{-\left[t^2+\left(\frac{d|\vec{q}+\vec{G}|}{2}\right)^2\frac{1}{t^2}\right]}dt = \frac{1}{2}\frac{1}{\sqrt{\pi}\sqrt{n_s}}\Psi\left(\frac{|\vec{q}+\vec{G}|^2}{4\pi n_s},\pi\eta^2\right) \quad . \tag{A.88}$$

Thus,

$$T_A(\vec{r},\vec{q}) \;=\; \frac{2}{\sqrt{\pi}}n_s\pi\sum_{\vec{G}} e^{-i(\vec{q}+\vec{G}).\vec{r}}e^{-i\vec{G}.\vec{c}}\left[\frac{1}{2}\frac{1}{\sqrt{\pi}\sqrt{n_s}}\Psi\left(\frac{|\vec{q}+\vec{G}|^2}{4\pi n_s},\pi\eta^2\right)\right] \tag{A.89}$$

$$T_A(\vec{r},\vec{q}) \;=\; \sqrt{n_s}\sum_{\vec{G}} e^{-i(\vec{q}+\vec{G}).\vec{r}}e^{-i\vec{G}.\vec{c}}\Psi\left(\frac{|\vec{q}+\vec{G}|^2}{4\pi n_s},\pi\eta^2\right) \tag{A.90}$$

and then,

$$T_I(\vec{r},\vec{q}) \;=\; \sqrt{n_s}\sum_{\vec{G}} e^{-i(\vec{q}+\vec{G}).\vec{r}}e^{-i\vec{G}.\vec{c}}\Psi\left(\frac{|\vec{q}+\vec{G}|^2}{4\pi n_s},\pi\eta^2\right) + \sum_{\vec{R}}\frac{e^{-i\vec{q}.(\vec{R}-\vec{c})}}{\gamma}\mathrm{erfc}(\varepsilon\gamma) \quad . \tag{A.91}$$

On the other hand, with $\varepsilon = \sqrt{\pi n_s}$ and $\gamma = [|\vec{r}-\vec{R}+\vec{c}|^2+d^2]^{1/2}$, we have that

$$\frac{\mathrm{erf}(\varepsilon\gamma)}{\gamma} = \frac{\mathrm{erf}(\sqrt{\pi n_s}[|\vec{r}-\vec{R}+\vec{c}|^2+d^2]^{1/2})}{[|\vec{r}-\vec{R}+\vec{c}|^2+d^2]^{1/2}} \tag{A.92}$$

and again, we write this equation in terms of the function $\Phi(x)$ given by

$$\Phi(x) = \sqrt{\frac{\pi}{x}}\mathrm{erfc}(\sqrt{x}) \quad . \tag{A.93}$$

If

$$\sqrt{x} = \sqrt{\pi n_s}[|\vec{r}-\vec{R}+\vec{c}|^2+d^2]^{1/2} \tag{A.94}$$

then

$$x = \pi[n_s|\vec{r}-\vec{R}+\vec{c}|^2+n_s d^2] \quad . \tag{A.95}$$

But, since $\eta = d\sqrt{n_s}$ and, therefore, $\eta^2 = d^2 n_s$, we obtain

$$x = \pi[n_s|\vec{r}-\vec{R}+\vec{c}|^2+\eta^2] \tag{A.96}$$

$$\frac{\mathrm{erf}(\varepsilon\gamma)}{\gamma} = \frac{\mathrm{erf}(\sqrt{\pi n_s}[|\vec{r}-\vec{R}+\vec{c}|^2+d^2]^{1/2})}{[|\vec{r}-\vec{R}+\vec{c}|^2+d^2]^{1/2}} = \sqrt{n_s}\Phi(\pi[n_s|\vec{r}-\vec{R}+\vec{c}|^2+\eta^2]) \tag{A.97}$$

and we can write

$$\begin{aligned} T_I(\vec{r},\vec{q}) &= \sqrt{n_s}\sum_{\vec{G}} e^{-i(\vec{q}+\vec{G}).\vec{r}} e^{-i\vec{G}.\vec{c}}\Psi\left(\frac{|\vec{q}+\vec{G}|^2}{4\pi n_s},\pi\eta^2\right)+ \\ & \sqrt{n_s}\sum_{\vec{R}} e^{-i\vec{q}.(\vec{R}-\vec{c})}\Phi(\pi[n_s|\vec{r}-\vec{R}+\vec{c}|^2+\eta^2]) \quad . \end{aligned} \tag{A.98}$$

Since

$$E_{IE} = Q^2 \lim_{\vec{r}\to 0} T_I(\vec{r},\vec{0}) \tag{A.99}$$

we are going to calculate $T_I(0,0)$:

$$\begin{aligned} \lim_{\vec{r}\to 0} T_I(\vec{r},\vec{0}) &= \sqrt{n_s}\sum_{\vec{G}} e^{-i\vec{G}.\vec{c}}\Psi\left(\frac{|\vec{G}|^2}{4\pi n_s},\pi\eta^2\right)+ \\ & \sqrt{n_s}\sum_{\vec{R}} e^{-i\vec{q}.(\vec{R}-\vec{c})}\Phi(\pi[n_s|\vec{R}+\vec{c}|^2+\eta^2]) \end{aligned} \tag{A.100}$$

$$\begin{aligned} \lim_{\vec{r}\to 0} T_I(\vec{r},\vec{0}) &= \sqrt{n_s}\lim_{G\to 0}\Psi\left(\frac{|\vec{G}|^2}{4\pi n_s},\pi\eta^2\right)+\sqrt{n_s}\sum_{\vec{G}\neq 0} e^{-i\vec{G}.\vec{c}}\Psi\left(\frac{|\vec{G}|^2}{4\pi n_s},\pi\eta^2\right)+ \\ & \sqrt{n_s}\sum_{\vec{R}} e^{-i\vec{q}.(\vec{R}-\vec{c})}\Phi(\pi[n_s|\vec{R}+\vec{c}|^2+\eta^2]) \end{aligned} \tag{A.101}$$

with

$$\begin{aligned} \Psi\left(\frac{|\vec{G}|^2}{4\pi n_s},\pi\eta^2\right) &= \frac{\pi\sqrt{n_s}}{|\vec{G}|}\left[e^{|\vec{G}|\eta/\sqrt{n_s}}\mathrm{erfc}\left(\frac{|\vec{G}|}{2\sqrt{\pi n_s}}+\sqrt{\pi}\eta\right)+\right. \\ & \left. e^{-|\vec{G}|\eta/\sqrt{n_s}}\mathrm{erfc}\left(\frac{|\vec{G}|}{2\sqrt{\pi n_s}}-\sqrt{\pi}\eta\right)\right] \quad . \end{aligned} \tag{A.102}$$

From equation

$$\mathrm{erf}(x)+\mathrm{erfc}(x)=1 \tag{A.103}$$

we have that,

$$\mathrm{erfc}\left(\frac{|\vec{G}|}{2\sqrt{\pi n_s}}\pm\sqrt{\pi}\eta\right) = 1-\mathrm{erf}\left(\frac{|\vec{G}|}{2\sqrt{\pi n_s}}\pm\sqrt{\pi}\eta\right) \tag{A.104}$$

$$\begin{aligned} \Psi\left(\frac{|\vec{G}|^2}{4\pi n_s},\pi\eta^2\right) &= \frac{\pi\sqrt{n_s}}{|\vec{G}|}\left[e^{|\vec{G}|\eta/\sqrt{n_s}}+e^{-|\vec{G}|\eta/\sqrt{n_s}}-e^{|\vec{G}|\eta/\sqrt{n_s}}\mathrm{erf}\left(\frac{|\vec{G}|}{2\sqrt{\pi n_s}}+\sqrt{\pi}\eta\right)\right. \\ & \left. -e^{-|\vec{G}|\eta/\sqrt{n_s}}\mathrm{erf}\left(\frac{|\vec{G}|}{2\sqrt{\pi n_s}}-\sqrt{\pi}\eta\right)\right] \end{aligned} \tag{A.105}$$

$$\Psi\left(\frac{|\vec{G}|^2}{4\pi n_s},\pi\eta^2\right) = \frac{\pi\sqrt{n_s}}{|\vec{G}|}\left[e^{|\vec{G}|\eta/\sqrt{n_s}}+e^{-|\vec{G}|\eta/\sqrt{n_s}}\right]-\frac{\pi\sqrt{n_s}}{|\vec{G}|}\left[e^{|\vec{G}|\eta/\sqrt{n_s}}\mathrm{erf}\left(\frac{|\vec{G}|}{2\sqrt{\pi n_s}}+\sqrt{\pi}\eta\right)\right.$$
$$\left.+e^{-|\vec{G}|\eta/\sqrt{n_s}}\mathrm{erf}\left(\frac{|\vec{G}|}{2\sqrt{\pi n_s}}-\sqrt{\pi}\eta\right)\right] \quad . \tag{A.106}$$

Now, let us define the functions

$$\Psi_A = \frac{\pi\sqrt{n_s}}{|\vec{G}|}\left[e^{|\vec{G}|\eta/\sqrt{n_s}}+e^{-|\vec{G}|\eta/\sqrt{n_s}}\right] \tag{A.107}$$

$$\Psi_B = -\frac{\pi\sqrt{n_s}}{|\vec{G}|}\left[e^{|\vec{G}|\eta/\sqrt{n_s}}\mathrm{erf}\left(\frac{|\vec{G}|}{2\sqrt{\pi n_s}}+\sqrt{\pi}\eta\right)+e^{-|\vec{G}|\eta/\sqrt{n_s}}\mathrm{erf}\left(\frac{|\vec{G}|}{2\sqrt{\pi n_s}}-\sqrt{\pi}\eta\right)\right] \tag{A.108}$$

and, therefore,

$$\Psi\left(\frac{|\vec{G}|^2}{4\pi n_s},\pi\eta^2\right) = \Psi_A+\Psi_B \tag{A.109}$$

$$\Psi\left(0,\pi\eta^2\right) = \lim_{G\to 0}\Psi_A+\lim_{G\to 0}\Psi_B \tag{A.110}$$

where

$$\lim_{G\to 0}\Psi_B = -\frac{\pi\sqrt{n_s}}{|\vec{G}|}\left[\mathrm{erf}\left(\sqrt{\pi}\eta\right)+\mathrm{erf}\left(-\sqrt{\pi}\eta\right)\right] \tag{A.111}$$

$$\lim_{G\to 0}\Psi_B = -\frac{\pi\sqrt{n_s}}{|\vec{G}|}\left[\mathrm{erf}\left(\sqrt{\pi}\eta\right)-\mathrm{erf}\left(\sqrt{\pi}\eta\right)\right] = \frac{0}{0} \tag{A.112}$$

since $\mathrm{erf}(-x) = -\mathrm{erf}(x)$. Thus, we can use the L'Hospital theorem, after the following definitions:

$$M = -\pi\sqrt{n_s}\left[e^{|\vec{G}|\eta/\sqrt{n_s}}\mathrm{erf}\left(\frac{|\vec{G}|}{2\sqrt{\pi n_s}}+\sqrt{\pi}\eta\right)+e^{-|\vec{G}|\eta/\sqrt{n_s}}\mathrm{erf}\left(\frac{|\vec{G}|}{2\sqrt{\pi n_s}}-\sqrt{\pi}\eta\right)\right] \tag{A.113}$$

and

$$N = G \tag{A.114}$$

and thus

$$\Psi_B = \frac{M}{N} \tag{A.115}$$

with

$$\lim_{G\to 0} \Psi_B = \lim_{G\to 0} \frac{M}{N} = \frac{0}{0} \quad . \tag{A.116}$$

Using the L'Hospital theorem,

$$\lim_{G\to 0} \Psi_B = \lim_{G\to 0} \frac{M}{N} = \lim_{G\to 0} \frac{\frac{dM}{dG}}{\frac{dN}{dG}} \tag{A.117}$$

where

$$\frac{dN}{dG} = 1 \quad . \tag{A.118}$$

On the other hand, in order to calculate $\frac{dM}{dG}$, we need to obtain the derivative of the integrals. Thus, if

$$I(t) = \int_{a(t)}^{b(t)} f(x)dx \tag{A.119}$$

then,

$$\frac{dI(t)}{dt} = f(b(t))\frac{db(t)}{dt} - f(a(t))\frac{da(t)}{dt} \tag{A.120}$$

and

$$\mathrm{erf}\left(\frac{|\vec{G}|}{2\sqrt{\pi n_s}} \pm \sqrt{\pi}\eta\right) = \frac{2}{\sqrt{\pi}} \int_0^{\frac{|\vec{G}|}{2\sqrt{\pi n_s}} \pm \sqrt{\pi}\eta} e^{-t^2} dt \tag{A.121}$$

$$\frac{d}{dG}\mathrm{erf}\left(\frac{|\vec{G}|}{2\sqrt{\pi n_s}} \pm \sqrt{\pi}\eta\right) = e^{-\left(\frac{|\vec{G}|}{2\sqrt{\pi n_s}} \pm \sqrt{\pi}\eta\right)^2} \frac{1}{\pi\sqrt{n_s}} \tag{A.122}$$

gives us

$$\lim_{G\to 0} \Psi_B = \lim_{G\to 0} \frac{\frac{dM}{dG}}{\frac{dN}{dG}} = -2\pi\sqrt{n_s}\left[\frac{e^{-\pi\eta^2}}{\pi\sqrt{n_s}} + \frac{\eta\,\mathrm{erf}(\sqrt{\pi}\eta)}{\sqrt{n_s}}\right] \quad . \tag{A.123}$$

On the other hand,

$$\lim_{G\to 0}\Psi_A = \lim_{G\to 0}\frac{\pi\sqrt{n_s}}{|\vec{G}|}\left[e^{|\vec{G}|\eta/\sqrt{n_s}} + e^{-|\vec{G}|\eta/\sqrt{n_s}}\right] \tag{A.124}$$

$$\lim_{G\to 0}\Psi_A = \lim_{G\to 0}\pi\sqrt{n_s}\left[\frac{e^{|\vec{G}|\eta/\sqrt{n_s}} - e^{-|\vec{G}|\eta/\sqrt{n_s}}}{G} + \frac{2e^{-|\vec{G}|\eta/\sqrt{n_s}}}{G}\right] \tag{A.125}$$

$$\lim_{G\to 0}\Psi_A = 2\pi\sqrt{n_s}\lim_{G\to 0}\frac{e^{-|\vec{G}|\eta/\sqrt{n_s}}}{G} + \pi\sqrt{n_s}\lim_{G\to 0}\left[\frac{e^{|\vec{G}|\eta/\sqrt{n_s}} - e^{-|\vec{G}|\eta/\sqrt{n_s}}}{G}\right] \tag{A.126}$$

$$\lim_{G\to 0}\Psi_A = 2\pi\sqrt{n_s}\left.\frac{e^{-|\vec{G}|\eta/\sqrt{n_s}}}{G}\right|_{G=0} + \frac{0}{0} \quad . \tag{A.127}$$

Again, applying the L'Hospital theorem, we have that

$$\lim_{G\to 0}\Psi_A = 2\pi\sqrt{n_s}\left.\frac{e^{-|\vec{G}|\eta/\sqrt{n_s}}}{G}\right|_{G=0} + \pi\sqrt{n_s}\lim_{G\to 0}\left[\frac{\eta}{\sqrt{n_s}}e^{|\vec{G}|\eta/\sqrt{n_s}} + \frac{\eta}{\sqrt{n_s}}e^{-|\vec{G}|\eta/\sqrt{n_s}}\right] \tag{A.128}$$

$$\lim_{G\to 0}\Psi_A = 2\pi\sqrt{n_s}\left.\frac{e^{-|\vec{G}|\eta/\sqrt{n_s}}}{G}\right|_{G=0} + 2\pi\eta \tag{A.129}$$

Then, the equation $(A.109)$ becomes

$$\Psi\left(0,\pi\eta^2\right) = 2\pi\sqrt{n_s}\left.\frac{e^{-|\vec{G}|\eta/\sqrt{n_s}}}{G}\right|_{G=0} + 2\pi\eta - 2\left[e^{-\pi\eta^2} + \pi\eta\,\mathrm{erf}(\sqrt{\pi}\eta)\right] \tag{A.130}$$

and, finally,

$$\begin{aligned}\lim_{\vec{r}\to 0}T_I(\vec{r},\vec{0}) = {} & 2\pi n_s\left.\frac{e^{-|\vec{G}|\eta/\sqrt{n_s}}}{G}\right|_{G=0} + 2\pi\eta\sqrt{n_s} - 2\sqrt{n_s}\left[e^{-\pi\eta^2} + \pi\eta\,\mathrm{erf}(\sqrt{\pi}\eta)\right] + \\ & \sqrt{n_s}\sum_{\vec{G}\neq 0}e^{-i\vec{G}.\vec{c}}\Psi\left(\frac{|\vec{G}|^2}{4\pi n_s},\pi\eta^2\right) + \sqrt{n_s}\sum_{\vec{R}}e^{-i\vec{q}.(\vec{R}-\vec{c})}\Phi(\pi[n_s|\vec{R}+\vec{c}|^2+\eta^2])\end{aligned} \tag{A.131}$$

with

$$E_{IE} = Q^2\lim_{\vec{r}\to 0}T_I(\vec{r},\vec{0}) \quad . \tag{A.132}$$

Thus,

$$\begin{aligned} E_{IE} \;=\; & 2\pi Q^2 n_s \frac{e^{-|\vec{G}|\eta/\sqrt{n_s}}}{G}\bigg|_{G=0} + 2\pi Q^2 \eta\sqrt{n_s} - 2Q^2\sqrt{n_s}\left[e^{-\pi\eta^2} + \pi\eta\,\mathrm{erf}(\sqrt{\pi}\eta)\right] + \\ & Q^2\sqrt{n_s}\sum_{\vec{G}\neq 0} e^{-i\vec{G}.\vec{c}}\Psi\left(\frac{|\vec{G}|^2}{4\pi n_s}, \pi\eta^2\right) + Q^2\sqrt{n_s}\sum_{\vec{R}} e^{-i\vec{q}.(\vec{R}-\vec{c})}\Phi(\pi[n_s|\vec{R}+\vec{c}|^2 + \eta^2]) \end{aligned} \tag{A.133}$$

and, again, the divergent term in the last equation is balanced by the interaction energy with a background $\rho_+ = Qn_s$, located in the opposite layer [36]. This interaction energy is given by

$$E_{IE}^B = -Q\rho_+ \int \frac{d^2r}{(r^2+d^2)^{1/2}} = -\,2\pi Q^2 n_s \frac{e^{-|\vec{q}|\eta/\sqrt{n_s}}}{q}\bigg|_{q=0} \quad . \tag{A.134}$$

Therefore, we obtain

$$E_{IE} = Q^2\sqrt{n/2}B(\eta) \tag{A.135}$$

where

$$\begin{aligned} B(\eta) = & \sum_{\vec{R}} \Phi(\pi[n|\vec{R}+\vec{c}|^2/2 + \eta^2]) \\ & + \sum_{\vec{G}\neq\vec{0}} e^{-i\vec{G}\cdot\vec{c}}\Psi\left(\frac{|\vec{q}+\vec{G}|^2}{2\pi n}, \pi\eta^2\right) \\ & + 2\{\pi\eta\cdot\mathrm{erfc}(\sqrt{\pi}\eta) - e^{-\pi\eta^2}\}. \end{aligned} \tag{A.136}$$

A.2 Magnetic case

A.2.1 Magnetic interaction energy per particle in each layer

From equation (2.6b), we have that

$$E_{0M} = \sum_{R\neq 0} \frac{\mu^2}{|\vec{R}|^3} \quad . \tag{A.137}$$

Following the Ref. [37], we define the function:

$$\psi_0(\vec{r},\vec{q}) = e^{i\vec{q}\cdot\vec{r}}\sum_{R\neq 0}\frac{e^{-i\vec{q}\cdot(\vec{r}+\vec{R})}}{|\vec{r}+\vec{R}|^3} \tag{A.138}$$

such that

$$E_{0M} = \mu^2 \lim_{\vec{r}\to 0}\psi_0(\vec{r},\vec{0}) \quad . \tag{A.139}$$

Using the identity based on the integral representation of the gamma function

$$\frac{1}{X^{2s}} = \frac{1}{\Gamma(s)}\int_0^\infty t^{s-1}e^{-X^2 t}dt \tag{A.140}$$

with $s = 3/2$, $\Gamma(3/2) = \sqrt{\pi}/2$, we have that

$$\frac{1}{|\vec{r}+\vec{R}|^3} = \frac{2}{\sqrt{\pi}}\int_0^\infty t^{1/2}e^{-|\vec{r}+\vec{R}|^2 t}dt \quad . \tag{A.141}$$

Substituting (A.139) into (A.136), we obtain:

$$\psi_0(\vec{r},\vec{q}) = e^{i\vec{q}\cdot\vec{r}}\sum_{R\neq 0} e^{-i\vec{q}\cdot(\vec{r}+\vec{R})}\frac{2}{\sqrt{\pi}}\int_0^\infty t^{1/2}e^{-|\vec{r}+\vec{R}|^2 t}dt \quad , \tag{A.142}$$

$$\psi_0(\vec{r},\vec{q}) = e^{i\vec{q}\cdot\vec{r}}\sum_{R} e^{-i\vec{q}\cdot(\vec{r}+\vec{R})}\frac{2}{\sqrt{\pi}}\int_0^\infty t^{1/2}e^{-|\vec{r}+\vec{R}|^2 t}dt - \frac{2}{\sqrt{\pi}}\int_0^\infty t^{1/2}e^{-|\vec{r}|^2 t}dt \quad . \tag{A.143}$$

If we separate the integrals above in the regions $(0,\alpha^2)$ and (α^2,∞), we obtain:

$$\begin{aligned}\psi_0(\vec{r},\vec{q}) \;=\;& e^{i\vec{q}\cdot\vec{r}}\sum_{R} e^{-i\vec{q}\cdot(\vec{r}+\vec{R})}\frac{2}{\sqrt{\pi}}\int_0^{\alpha^2} t^{1/2}e^{-|\vec{r}+\vec{R}|^2 t}dt \\ &+e^{i\vec{q}\cdot\vec{r}}\sum_{R} e^{-i\vec{q}\cdot(\vec{r}+\vec{R})}\frac{2}{\sqrt{\pi}}\int_{\alpha^2}^\infty t^{1/2}e^{-|\vec{r}+\vec{R}|^2 t}dt \\ &-\frac{2}{\sqrt{\pi}}\int_0^{\alpha^2} t^{1/2}e^{-|\vec{r}|^2 t}dt - \frac{2}{\sqrt{\pi}}\int_{\alpha^2}^\infty t^{1/2}e^{-|\vec{r}|^2 t}dt\end{aligned} \tag{A.144}$$

$$\begin{aligned}\psi_0(\vec{r},\vec{q}) \;=\;& e^{i\vec{q}\cdot\vec{r}}\frac{2}{\sqrt{\pi}}\int_0^{\alpha^2} t^{1/2}\left[\sum_R e^{-|\vec{r}+\vec{R}|^2 t}e^{-i\vec{q}\cdot(\vec{r}+\vec{R})}\right]dt + \frac{2}{\sqrt{\pi}}\int_{\alpha^2}^\infty t^{1/2}e^{-|\vec{r}|^2 t}dt \\ &+e^{i\vec{q}\cdot\vec{r}}\sum_{R\neq 0} e^{-i\vec{q}\cdot(\vec{r}+\vec{R})}\frac{2}{\sqrt{\pi}}\int_{\alpha^2}^\infty t^{1/2}e^{-|\vec{r}+\vec{R}|^2 t}dt - \frac{2}{\sqrt{\pi}}\int_0^{\alpha^2} t^{1/2}e^{-|\vec{r}|^2 t}dt \\ &-\frac{2}{\sqrt{\pi}}\int_{\alpha^2}^\infty t^{1/2}e^{-|\vec{r}|^2 t}dt\end{aligned} \tag{A.145}$$

$$\begin{aligned}\psi_0(\vec{r},\vec{q}) \;=\;& e^{i\vec{q}\cdot\vec{r}}\frac{2}{\sqrt{\pi}}\int_0^{\alpha^2} t^{1/2}\left[\sum_R e^{-|\vec{r}+\vec{R}|^2 t}e^{-i\vec{q}\cdot(\vec{r}+\vec{R})}\right]dt - \frac{2}{\sqrt{\pi}}\int_0^{\alpha^2} t^{1/2}e^{-|\vec{r}|^2 t}dt \\ &+e^{i\vec{q}\cdot\vec{r}}\sum_{R\neq 0} e^{-i\vec{q}\cdot(\vec{r}+\vec{R})}\frac{2}{\sqrt{\pi}}\int_{\alpha^2}^\infty t^{1/2}e^{-|\vec{r}+\vec{R}|^2 t}dt\end{aligned} \tag{A.146}$$

Using the 2D Poisson summation formula

$$\sum_R e^{-|\vec{r}+\vec{R}|^2 t} e^{-i\vec{q}.\vec{R}} = \frac{\pi n_s}{t} \sum_G e^{-|\vec{q}+\vec{G}|^2/4t} e^{i(\vec{q}+\vec{G}).\vec{r}} \tag{A.147}$$

the equation A.144 becomes

$$\begin{aligned} \psi_0(\vec{r},\vec{q}) &= \pi n_s \sum_G e^{i(\vec{q}+\vec{G}).\vec{r}} \frac{2}{\sqrt{\pi}} \int_0^{\alpha^2} t^{-1/2} e^{-|\vec{q}+\vec{G}|^2/4t} dt - \frac{2}{\sqrt{\pi}} \int_0^{\alpha^2} t^{1/2} e^{-|\vec{r}|^2 t} dt \\ &+ \sum_{R\neq 0} e^{-i\vec{q}\cdot\vec{R}} \frac{2}{\sqrt{\pi}} \int_{\alpha^2}^{\infty} t^{1/2} e^{-|\vec{r}+\vec{R}|^2 t} dt \quad . \end{aligned} \tag{A.148}$$

Now, we need the following equations:

$$\int_{\alpha^2}^{\infty} t^{1/2} e^{-x^2 t} dt = \frac{\sqrt{\pi}}{2x^3} \mathrm{erfc}(\alpha x) + \frac{\alpha e^{-\alpha^2 x^2}}{x^2} \tag{A.149}$$

$$\int_0^{\alpha^2} t^{-1/2} e^{-x^2/4t} dt = e^{-x^2/4\alpha^2} \left[2\alpha - \sqrt{\pi} x e^{x^2/4\alpha^2} \mathrm{erfc}(x/2\alpha) \right] \quad . \tag{A.150}$$

Therefore,

$$\int_{\alpha^2}^{\infty} t^{1/2} e^{-|\vec{r}+\vec{R}|^2 t} dt = \frac{\sqrt{\pi}}{2|\vec{r}+\vec{R}|^3} \mathrm{erfc}(\alpha|\vec{r}+\vec{R}|) + \frac{\alpha e^{-\alpha^2|\vec{r}+\vec{R}|^2}}{|\vec{r}+\vec{R}|^2} \tag{A.151}$$

e

$$\int_0^{\alpha^2} t^{-1/2} e^{-|\vec{q}+\vec{G}|^2/4t} dt = e^{-|\vec{q}+\vec{G}|^2/4\alpha^2} \left[2\alpha - \sqrt{\pi} |\vec{q}+\vec{G}| e^{|\vec{q}+\vec{G}|^2/4\alpha^2} \mathrm{erfc}(|\vec{q}+\vec{G}|/2\alpha) \right] \tag{A.152}$$

$$\int_0^{\alpha^2} t^{-1/2} e^{-|\vec{q}+\vec{G}|^2/4t} dt = 2\alpha e^{-|\vec{q}+\vec{G}|^2/4\alpha^2} - \sqrt{\pi} |\vec{q}+\vec{G}| \mathrm{erfc}(|\vec{q}+\vec{G}|/2\alpha) \quad . \tag{A.153}$$

Besides,

$$\int_0^{\alpha^2} t^{1/2} e^{-|\vec{r}|^2 t} dt = \frac{\sqrt{\pi}}{2r^3} \mathrm{erf}(\alpha r) - \frac{\alpha e^{-\alpha^2 r^2}}{r^2} \quad . \tag{A.154}$$

Substituting (A.149), (A.151) and (A.152) into (A.146), with $n_s = n/2$ and $\alpha = \varepsilon$, we obtain:

$$\begin{aligned}\psi_0(\vec{r},\vec{q}) = \frac{\pi n}{2}\sum_{\vec{G}} e^{i(\vec{q}+\vec{G})\cdot\vec{r}} & \left[\frac{4\varepsilon}{\sqrt{\pi}} e^{-|\vec{q}+\vec{G}|^2/4\varepsilon^2}\right. \\ & \left. - 2|\vec{q}+\vec{G}|\mathrm{erfc}\left(\frac{|\vec{q}+\vec{G}|}{2\varepsilon}\right)\right] \\ & + \left[\frac{2\varepsilon e^{-\varepsilon^2 r^2}}{\sqrt{\pi} r^2} - \frac{\mathrm{erf}(\varepsilon r)}{r^3}\right] \\ & + \sum_{\vec{R}\neq\vec{0}} e^{-i\vec{q}\cdot\vec{R}} \left[\frac{\mathrm{erfc}(\varepsilon|\vec{R}+\vec{r}|)}{|\vec{R}+\vec{r}|^3}\right. \\ & \left. + \left(\frac{2\varepsilon}{\sqrt{\pi}}\right)\frac{e^{-\varepsilon^2|\vec{R}+\vec{r}|^2}}{|\vec{R}+\vec{r}|^2}\right] .\end{aligned} \tag{A.155}$$

Since

$$E_{0M} = \mu^2 \lim_{r\to 0}\psi_0(\vec{r},\vec{0}) \quad , \tag{A.156}$$

we have to calculate $\lim_{\vec{r}\to 0}\psi_0(\vec{r},\vec{0})$:

$$\begin{aligned}\lim_{r\to 0}\psi_0(\vec{r},\vec{0}) = \frac{\pi n}{2}\sum_{\vec{G}} & \left[\frac{4\varepsilon}{\sqrt{\pi}} e^{-|\vec{G}|^2/4\varepsilon^2} - 2|\vec{G}|\mathrm{erfc}\left(\frac{|\vec{G}|}{2\varepsilon}\right)\right] \\ & + \lim_{r\to 0}\left[\frac{2\varepsilon e^{-\varepsilon^2 r^2}}{\sqrt{\pi} r^2} - \frac{\mathrm{erf}(\varepsilon r)}{r^3}\right] \\ & + \sum_{\vec{R}\neq\vec{0}}\left[\frac{\mathrm{erfc}(\varepsilon|\vec{R}|)}{|\vec{R}|^3} + \frac{2\varepsilon}{\sqrt{\pi}}\frac{e^{-\varepsilon^2|\vec{R}|^2}}{|\vec{R}|^2}\right] .\end{aligned} \tag{A.157}$$

But,

$$\lim_{r\to 0}\left[\frac{2\varepsilon e^{-\varepsilon^2 r^2}}{\sqrt{\pi} r^2} - \frac{\mathrm{erf}(\varepsilon r)}{r^3}\right] = \lim_{r\to 0}\left[\frac{2\alpha r e^{-\varepsilon^2 r^2} - \sqrt{\pi}\mathrm{erf}(\varepsilon r)}{\sqrt{\pi} r^3}\right] = \frac{0}{0} \quad . \tag{A.158}$$

Therefore, we can use the L'Hospital theorem, after the following definitions:

$$f(r) = 2\varepsilon r e^{-\varepsilon^2 r^2} - \sqrt{\pi}\mathrm{erf}(\varepsilon r) \tag{A.159}$$

and

$$g(r) = \sqrt{\pi} r^3 \tag{A.160}$$

such that

$$\lim_{r\to 0}\frac{f(r)}{g(r)} = \lim_{r\to 0}\frac{\frac{df}{dr}}{\frac{dg}{dr}} = \lim_{r\to 0}\frac{-4\varepsilon^3 r^2 e^{-\varepsilon^2 r^2}}{3\sqrt{\pi}r^2} = \frac{-4\varepsilon^3}{3\sqrt{\pi}} \quad . \tag{A.161}$$

Thus, we obtain (with $\varepsilon = \sqrt{\pi n_s} = \sqrt{\pi n/2}$):

$$E_{0M} = \mu^2 (n/2)^{3/2} C, \tag{A.162}$$

where

$$\begin{aligned} C = &\sum_{\vec{G}}\left[4\pi e^{-|\vec{G}|^2/2\pi n} - \frac{2|\vec{G}|\pi}{\sqrt{n/2}}\mathrm{erfc}\left(\frac{|\vec{G}|}{2\sqrt{\pi n/2}}\right)\right] \\ &+ \sum_{\vec{R}\neq\vec{0}}\left[\frac{\mathrm{erfc}(\sqrt{\pi n/2}|\vec{R}|)}{(n/2)^{3/2}|\vec{R}|^3} + \left(\frac{4}{n}\right)\frac{e^{-\pi n|\vec{R}|^2/2}}{|\vec{R}|^2}\right] - \frac{4\pi}{3} \quad . \end{aligned} \tag{A.163}$$

A.2.2 Magnetic interaction energy per particle between particles in distinct layers

From equation (2.7)b, we have that

$$E_{IM} = \sum_{\vec{R}} \frac{\mu^2(|\vec{R}+\vec{c}|^2 - 2d^2)}{(|\vec{R}+\vec{c}|^2 + d^2)^{5/2}} \quad . \tag{A.164}$$

Following the procedure developed in Ref. [37], we define the function

$$\psi_I(\vec{r},\vec{q}) = e^{i\vec{q}\cdot\vec{r}}\sum_{\vec{R}}\left(\frac{e^{-i\vec{q}\cdot(\vec{r}+\vec{R}+\vec{c})}}{|\vec{r}+\vec{R}+\vec{c}|^3} + \frac{-3d^2 e^{-i\vec{q}\cdot(\vec{r}+\vec{R}+\vec{c})}}{|\vec{r}+\vec{R}+\vec{c}|^5}\right) \tag{A.165}$$

which can also be written as

$$\psi_I(\vec{r},\vec{q}) = \psi_{I1}(\vec{r},\vec{q}) - 3d^2\psi_{I2}(\vec{r},\vec{q}) \tag{A.166}$$

with

$$\psi_{I1}(\vec{r},\vec{q}) = \sum_{\vec{R}}\frac{e^{-i\vec{q}\cdot(\vec{R}+\vec{c})}}{|\vec{r}+\vec{R}+\vec{c}|^3}, \tag{A.167}$$

$$\psi_{I2}(\vec{r},\vec{q}) = \sum_{\vec{R}}\frac{e^{-i\vec{q}\cdot(\vec{R}+\vec{c})}}{|\vec{r}+\vec{R}+\vec{c}|^5}, \tag{A.168}$$

where $|\vec{r}+\vec{R}+\vec{c}| \equiv (|\vec{r}+\vec{R}+\vec{c}|^2 + d^2)^{1/2}$. Therefore,

$$E_{IM} = \mu^2 \lim_{\vec{r}\to 0} \psi_I(\vec{r},\vec{0}). \tag{A.169}$$

Using the equations (A.138) and (A.145), we can write

$$\begin{aligned} \psi_{I1}(\vec{r},\vec{q}) &= \pi n_s \sum_G e^{i(\vec{q}+\vec{G}).\vec{r}} e^{i\vec{G}.\vec{c}} \frac{2}{\sqrt{\pi}} \int_0^{\alpha^2} t^{-1/2} e^{-\frac{|\vec{q}+\vec{G}|^2}{4t} - d^2 t} dt \\ &+ \sum_R e^{-i\vec{q}\cdot(\vec{R}+\vec{c})} \frac{2}{\sqrt{\pi}} \int_{\alpha^2}^{\infty} t^{1/2} e^{-|\vec{r}+\vec{R}+\vec{c}|^2 t} dt \quad . \end{aligned} \tag{A.170}$$

The integral

$$I_1 = \int_0^{\alpha^2} t^{-1/2} e^{-\frac{|\vec{q}+\vec{G}|^2}{4t} - d^2 t} dt \tag{A.171}$$

with the change of variable $t = 1/w^2$ can be written as

$$I_1 = 2 \int_{1/\alpha}^{\infty} w^{-2} e^{-\frac{|\vec{q}+\vec{G}|^2 w^2}{4} - \frac{d^2}{w^2}} dw \tag{A.172}$$

$$I_1 = \frac{\sqrt{\pi}}{2d} \left[e^{-|\vec{q}+\vec{G}|d} \mathrm{erfc}\left(\frac{|\vec{q}+\vec{G}|}{2\alpha} - \alpha d \right) - e^{|\vec{q}+\vec{G}|d} \mathrm{erfc}\left(\frac{|\vec{q}+\vec{G}|}{2\alpha} + \alpha d \right) \right] \quad . \tag{A.173}$$

Using the equation (A.147), the second integral in the equation (A.168) can be solved. Therefore,

$$\begin{aligned} \psi_{I1}(\vec{r},\vec{q}) &= \frac{\pi n_s}{d} \sum_G e^{i(\vec{q}+\vec{G}).\vec{r}} e^{i\vec{G}.\vec{c}} \left[e^{-|\vec{q}+\vec{G}|d} \mathrm{erfc}\left(\frac{|\vec{q}+\vec{G}|}{2\alpha} - \alpha d \right) - e^{|\vec{q}+\vec{G}|d} \mathrm{erfc}\left(\frac{|\vec{q}+\vec{G}|}{2\alpha} + \alpha d \right) \right] \\ &+ \sum_R e^{-i\vec{q}\cdot(\vec{R}+\vec{c})} \left[\frac{\mathrm{erfc}(\alpha|\vec{r}+\vec{R}+\vec{c}|)}{|\vec{r}+\vec{R}+\vec{c}|^3} + \left(\frac{2\alpha}{\sqrt{\pi}} \right) \frac{e^{-\alpha^2|\vec{r}+\vec{R}+\vec{c}|^2}}{|\vec{r}+\vec{R}+\vec{c}|^2} \right] \quad . \end{aligned} \tag{A.174}$$

Now, we have to work with the expression

$$\psi_{I2}(\vec{r},\vec{q}) = \sum_{\vec{R}} \frac{e^{-i\vec{q}\cdot(\vec{R}+\vec{c})}}{|\vec{r}+\vec{R}+\vec{c}|^5} \quad . \tag{A.175}$$

Using the equation (A.138) (with $s = 5/2$, $\Gamma(5/2) = 3\sqrt{\pi}/4$) and the equation (A.145), we obtain

$$\begin{aligned}\psi_{I2}(\vec{r},\vec{q}) &= \frac{4\sqrt{\pi}n_s}{3}\sum_G e^{i(\vec{q}+\vec{G}).\vec{r}}e^{i\vec{G}.\vec{c}}\int_0^{\alpha^2} t^{1/2}e^{-\frac{|\vec{q}+\vec{G}|^2}{4t}-d^2t}dt \\ &\quad +\frac{4}{3\sqrt{\pi}}\sum_R e^{-i\vec{q}\cdot(\vec{R}+\vec{c})}\int_{\alpha^2}^{\infty} t^{3/2}e^{-|\vec{r}+\vec{R}+\vec{c}|^2t}dt \quad . \end{aligned} \tag{A.176}$$

The first integral in (A.174) can be solved using the change of variable $t = 1/w^2$ with the equation

$$\begin{aligned}\int_{1/\alpha}^{\infty} w^{-4}e^{-\frac{x^2w^2}{4}-\frac{y^2}{w^2}}dw &= \frac{1}{8y^3}\left[-4\alpha y e^{-\frac{x^2}{4\alpha^2}-\alpha^2y^2}+\sqrt{\pi}e^{-xy}(xy+1)\mathrm{erfc}\left(\frac{x}{2y}-\alpha y\right)+\right. \\ &\quad \left.\sqrt{\pi}e^{xy}(xy-1)\mathrm{erfc}\left(\frac{x}{2y}+\alpha y\right)\right] \quad . \end{aligned} \tag{A.177}$$

The second integral in (A.174) can be solved using the result

$$\int_{\alpha^2}^{\infty} t^{3/2}e^{-x^2t}dt = \frac{3\sqrt{\pi}}{4x^5}\mathrm{erfc}(\alpha x)+\frac{\alpha(3+2\alpha^2x^2)e^{-\alpha^2x^2}}{2x^4} \quad . \tag{A.178}$$

Using the equation (with $\alpha = \varepsilon$, $\varepsilon = \sqrt{\pi n_s} = \sqrt{\pi n/2}$, $\eta = d\sqrt{n/2}$)

$$E_{IM} = \mu^2 \lim_{\vec{r}\to 0}\psi_I(\vec{r},\vec{0}) \tag{A.179}$$

with

$$\psi_I(\vec{r},\vec{q}) = \psi_{I1}(\vec{r},\vec{q}) - 3d^2\psi_{I2}(\vec{r},\vec{q}) \tag{A.180}$$

we obtain

$$E_{IM} = \mu^2(n/2)^{3/2}D(\eta) \tag{A.181}$$

where

$$\begin{aligned}
D(\eta) = \sum_{\vec{G}} e^{i\vec{G}\cdot\vec{c}} \Bigg[& 4\pi e^{-\frac{|\vec{G}|^2}{2\pi n} - \pi\eta^2} \\
& - \frac{\pi|\vec{G}|}{\sqrt{n/2}} e^{-|\vec{G}|\eta/\sqrt{n/2}} \mathrm{erfc}\left(\frac{|\vec{G}|}{2\sqrt{\pi n/2}} - \sqrt{\pi}\eta\right) \\
& - \frac{\pi|\vec{G}|}{\sqrt{n/2}} e^{|\vec{G}|\eta/\sqrt{n/2}} \mathrm{erfc}\left(\frac{|\vec{G}|}{2\sqrt{\pi n/2}} + \sqrt{\pi}\eta\right)\Bigg] \\
& + \sum_{\vec{R}} \left[\frac{\mathrm{erfc}(\sqrt{\pi n/2}|\vec{R}+\vec{c}|)}{(n/2)^{3/2}|\vec{R}+\vec{c}|^3} \left(1 - \frac{6\eta^2}{n|\vec{R}+\vec{c}|^2}\right) \right. \\
& \left. + \frac{4e^{-\pi n|\vec{R}+\vec{c}|^2/2}}{n|\vec{R}+\vec{c}|^2} \left(1 - \frac{6\eta^2}{n|\vec{R}+\vec{c}|^2} - 2\pi\eta^2\right)\right] \quad .
\end{aligned} \tag{A.182}$$

Bibliography

[1] C. N. Likos, Physics Reports **348**, 267 (2001).

[2] P. Keim, G. Maret, U. Herz, and H. H. von Grünberg, Phys. Rev. Lett. **92**, 215504 (2004).

[3] F. M. Peeters and Xiaoguang Wu, Phys. Rev. A **35**, 3109 (1987).

[4] F. Ebert, P. Dillmann, G. Maret and P. Keim, Rev. Sci. Instrum. **80**, 083902 (2009).

[5] Adam D. Law, D. Martin A. Buzza, and Tommy S. Horozov, Phys. Rev. Lett. **106**, 128302 (2011).

[6] R. Messina and H. Löwen, Phys. Rev. Lett. **91**, 146101 (2003).

[7] Y. Levin, Rep. Prog. Phys. **65**, 1577 (2002).

[8] L. Assoud, R. Messina and H. Löwen, J. Chem. Phys. **129**, 164511 (2008).

[9] A. Delattre, S. Pouget, J. F. Jacuot, Y. Samson, and P Reiss, Small **6**, 932 (2010).

[10] A. F. C. Campos, F. A. Tourinho, G. J. da Silva, M. C. F. L. Lara, and J. Depeyrot, Eur. Phys. J. E **6**, 29 (2001).

[11] Norman Hoffmann, Christos N Likos, and Hartmut Löwen, J. Phys.: Condens. Matter **18**, 10193 (2006).

[12] K. Zahn and G. Maret, Phys. Rev. Lett. **85**, 3656 (2000).

[13] K. Zahn, R. Lenke, and G. Maret, Phys. Rev. Lett. **82**, 2721 (1999).

[14] U. Gasser, C. Eisenmann, G. Maret, and P. Keim, Chem. Phys. Chem. **11**, 963 (2010).

[15] Georg M. Bruun and David R. Nelson, Phys. Rev. B **89**, 094112 (2014).

[16] Julia Fornleitner, Gerhard Kahl, and Christos N. Likos, Phys. Rev. E **81**, 060401(R) (2010).

[17] E. P. Wigner, Phys. Rev. **46**, 1002 (1934).

[18] C. C. Grimes and G. Adams, Phys. Rev. Lett. **42**, 795 (1979).

[19] D. W. Wang, M. D. Lukin, and E. Demler, Phys. Rev. Lett. **97**, 180413 (2006).

[20] D. W. Wang, Phys. Rev. Lett. **98**, 060403 (2007).

[21] H. P. Buchler, E. Demler, M. D. Lukin, A. Micheli, N. V. Prokof'ev, G. Pupillo, and P. Zoller, Phys. Rev. Lett. **98**, 060404 (2007).

[22] M. Golosovsky, Y. Saado, and D. Davidov, Phys. Rev. E **65**, 061405 (2002).

[23] S. Neser, C Bechinger, P. Leiderer, and T. Palberg, Phys. Rev. Lett. **79**, 2348 (1997).

[24] A. D. Law, T. S. Horozov, and D. M. Buzza, Soft Matter **7**, 8923 (2011).

[25] R. E. Rosensweig, *Ferrohydrodynamics*, (Dover Publications, New York, USA, 1985).

[26] D. J. Griffiths, *Introduction to Eletrodynamics*, (Prentice Hall, New Jersey, 1999).

[27] C. Kittel, Phys. Rev. **70**, 965 (1946).

[28] C. Kittel, Phys. Rev. Lett. **73**, 810 (1948).

[29] C. P. Bean, J. D. Livingston, Appl. Phys. **30**, 120S (1959).

[30] J. H. Chu and Lin I, Phys. Rev. Lett. **72**, 4009 (1994).

[31] Gwennow Coupier, Claudine Guthmann, Yves Noat, and M. SaintJean, Phys. Rev. E **71**, 046105 (2005).

[32] Peter Schall, Itai Cohen, David A. Weitz, and Frans Spaepen, Nature (London), **440**, 319 (2006).

[33] W. P. Ferreira, A. Matulis, G. A. Farias, and F. M. Peeters, Phys. Rev. E **67**, 046601 (2003).

[34] L. Bonsall and A. A. Maradudin, Phys. Rev. B **15**, 1959 (1977); F. M. Peeters, Phys. Rev. B **30**, 159 (1984).

[35] D. S. Fisher, Phys. Rev. B **26**, 5009 (1982).

[36] G. Goldoni and F. M. Peeters, Phys. Rev. B **53**, 4591 (1996).

[37] Xin Lu, Chang-Qin Wu, Andrea Micheli, and Guido Pupillo, Phys. Rev. B **78**, 024108 (2008).

[38] J. Dobnikar, J. Fornleitner, and G. Kahl, J. Phys. Condens. Matter, **20**, 494220 (2008).

[39] Julia Fornleitner, Federica Lo Verso, Gerhard Kahl, and Christos N. Likos, Soft Matter, **4**, 480 (2008).

[40] L. Assoud, F. Ebert, P. Keim, R. Messina, G. Maret, and H. Löwen, J. Phys. Condens. Matter, **21**, 464114 (2009).

[41] Angang Dong, Xingchen Ye, Jun Chen, and Christopher B. Murray, Nano Lett. **11**, 1804-1809.

[42] F. M. Peeters and X. G. Wu, Phys. Rev. A **35** , 3109 (1987).

[43] M. P. Allen and D. J. Tildesley, *Computer Simulation of Liquids*, (Claredon Press, Oxford, 1992), p. 155.

[44] G. P. Srivastava, *The Physics of Phonons*, (Adam Hilger, Bristol, 1990).

[45] R. S. Crandall and R. Willians, Phys. Lett. **34A**, 404 (1971).

[46] P. M. Platzman and H. Fukuyawa , Phys. Rev. B **10**, 3150 (1974).

[47] F. M. Peeters, Phys. Rev. B **30**, 159 (1984).

[48] R. W. Hockney and T. R. Brown, J. Phys. C **8**, 1813 (1975).

[49] D. J. Thouless, J. Phys. C **11**, L189 (1978).

[50] C. C. Grimes and G. Adams, Phys. Rev. Lett. **42**, 795 (1979).

[51] J. J. Weis, D. Levesque and S. Jorge, Phys. Rev. B **63**, 045308 (2001).

[52] I. V. Schweigert, V. A. Schweigert, and F. M. Peeters, Phys. Rev. Lett. **82**, 5293 (1999).

[53] I. V. Schweigert, V. A. Schweigert, and F. M. Peeters, Phys. Rev. B **60**, 14665 (1999).

[54] P. Keim, G. Maret, U. Herz and H. H. von Grünberg, Phys. Rev. Lett. **92**, 215504 (2004).

[55] A. M. Alsayed, M. F. Islam, J. Zhang, P. J. Collings, and A. G. Yodh, Science, **309**, 1207 (2005).

[56] I. R. O. Ramos, W. P. Ferreira, F. F. Munarin, F. M. Peeters, and G. A. Farias, Phys. Rev. E **85**, 051404 (2012).

[57] K. Zahn, R. Lenke, and G. Maret, Phys. Rev. Lett. **82**, 2721 (1999); K. Zahn and G. Maret, Phys. Rev. Lett. **85**, 3656 (2000).

[58] A. Delattre, S. Pouget, J. F. Jacuot, Y. Samson, and P. Reiss, Small **6**, 932 (2010).

[59] F. A. Lindemann, Physik. Z. **11**, 609 (1910).

[60] D. Pines, *Elementary Excitations in Solids*, (W. A. Benjamin, New York, 1983).

[61] V. M. Bedanov, G. V. Gadiyak, and Y. E. Lozovik, Phys. Lett. **109A**, 289 (1985).

[62] A. A. Maradudin, E. W. Montroll, G. H. Weiss, and I. P. Ipatova, *Theory of Lattice Dynamics in the Harmonic Approximation* (Academic Press, New York, 1971), Suppl. 3.

[63] K. Zahn, R. Lenke, and G. Maret, Phys. Rev. Lett. **82**, 2721 (1999).

[64] P. Schall, I. Cohen, D. A. Weitz, and F. Spaepen, Nature (London), **440**, 319 (2006).

[65] P. Keim, G. Maret, U. Herz, and H. H. von Grünberg, Phys. Rev. Lett. **92**, 215504 (2004).

[66] Sofi Nöjd, Priti S. Mohanty, Payam Baheri, Anand Yethiraj, and Peter Schurtenberger, Soft Matter, **9**, 9199 (2013).

[67] T. Stirner and J. Sun, Langmuir **21**, 6636 (2005).

[68] L. Assoud, R. Messina, and H. Löwen, Europhys. Lett. **80**, 48001 (2007).

[69] Julia Fornleitner, Federica Lo Verso, Gerhard Kahl, and Christos N. Likos, Soft Matter, **4**, 480 (2008).

[70] J. Fornleitner, F. Lo Verso, G. Kahl, and C. N. Likos, Langmuir **25**, 7836 (2009).

[71] N. Hoffmann, C. Likos, and H. Löwen, J. Phys.: Condens. Matter **18**, 10193 (2006).

[72] N. Hoffmann, F. Ebert, C. N. Likos, H. Löwen, and G. Maret, Phys. Rev. Lett. **97**, 078301 (2006).

[73] F. Ebert, P. Keim, and G. Maret, Eur. Phys. J. E **26**, 161 (2008).

[74] H. H. von Grünberg and J. Baumgartl, Phys. Rev. E **75**, 051406 (2007).

[75] N. Osterman, D. Babic, I. Poberaj, J. Dobnikar, and P. Ziherl, Phys. Rev. Lett. **99**, 248301 (2007).

[76] F. A. Lindemann, Physik. Z. **11**, 609 (1910).

[77] W. P. Ferreira, G. A. Farias, and F. M. Peeters, J. Phys.: Condens. Matter **22**, 285103 (2010).

[78] K. Zahn and G. Maret, Phys. Rev. Lett. **85**, 3656 (2000).